

AD-A280 632



**CALIBRATION AND INITIAL
TESTING OF A NEW
HYDRAULIC SIMULATOR**

THESIS

Cristian A. Puebla, B.S.

AFIT/GA/ENY/94J



174 98 **94-19377**

CALIBRATION AND INITIAL
TESTING OF A NEW
HYDRAULIC SIMULATOR

THESIS

Presented to the Faculty of the School of Engineering
of the Air Force Institute of Technology

Air University

In Partial Fulfillment of the
Requirements for the Degree of
Master of Science in Astronautical Engineering

Cristian A. Puebla, B.S.

June 1994

Accession For	
NTIS	<input checked="" type="checkbox"/>
CRA&I	<input checked="" type="checkbox"/>
DTIC	<input type="checkbox"/>
TAB	<input type="checkbox"/>
Unannounced	<input type="checkbox"/>
Justification _____	
By _____	
Distribution /	
Availability Codes	
Dist	Avail and / or Special
A-1	

Approved for public release; distribution unlimited

Acknowledgments

This study is by no means the result of the individual effort of the author who is fully aware that very little could have been accomplished without the help of the many people who, in one way or another, were involved in this project and whose aid is hereby gratefully acknowledged.

First and foremost the author is grateful to his Heavenly Father for the growth he experienced through the many hardships and difficulties in the completion of this project. He also is deeply grateful to his wife Veronica and family for enduring his stay at AFIT with love, patience and understanding.

The author wants to express his gratitude to his advisor, Dr. Paul King, whose direction and support were key factors in the successful completion of this project. A very special word of gratitude goes to Lt. USAF Raymond Tsui, Lt. USAF Michael Meyer, Mr. Andrew Pitts and Mrs. Kathleen MacGuffin without whose help, enthusiasm and friendship this project would have never been possible.

Cristian Puebla

Table of Contents

Acknowledgments	i
Table of Contents	ii
List of Figures	v
List of Tables	viii
List of Symbols.....	x
Abstract.....	xv
I. INTRODUCTION.....	1.1
1.1 Background and Problem.	1.1
1.2 Objective and Scope	1.2
II. THEORY.....	2.1
2.1 Introduction.	2.1
2.2 Derivation of the Gas Hydraulic Analogy	2.2
2.3 Consideration of Simplifying Assumptions.....	2.8
2.4 Investigation of the Analogy.....	2.11
2.5 Modification of the Analogy for Quantitative Application.	2.17
III. EXPERIMENTAL APPARATUS	3.1
3.1 Hydraulic Simulator	3.1
3.2 Modification to the Simulator	3.2
3.3 Image Acquisition and Data Analysis	3.4

3.4 Models-----	3.5
IV. EXPERIMENTAL METHODS-----	4.1
4.1 Calibration of the Hydraulic Simulator -----	4.1
4.1.1 Objective-----	4.1
4.1.2 Froude Number versus Head Height-----	4.1
4.1.3 Uniform Flow -----	4.8
4.1.4 Analysis of Error in the Data.-----	4.11
4.1.5 Sensitivity Analysis -----	4.16
4.2 Description of Experimental Methods on Models-----	4.19
4.2.1 Capsule-----	4.19
4.2.2 Capsule and Fuselage-----	4.21
V. RESULTS AND DISCUSSION-----	5.1
5.1 Capsule -----	5.1
5.2 Capsule and Fuselage-----	5.6
VI. CONCLUSIONS AND RECOMMENDATIONS-----	6.1
6.1 Conclusions -----	6.1
6.2 Recommendations-----	6.2

VII. REFERENCES	7.1
------------------------	------------

Appendix A: Figures	A.1
----------------------------	------------

Appendix B: Tables of Experimental Values	B.1
--	------------

Appendix C: Calibration Procedure	C.1
--	------------

List of Figures

Figure	Page
2.1(a) Oblique Hydraulic Jump-----	A.1
2.1(b) Oblique Expansion Wave-----	A.2
2.2 Graphical Relationship Between $F_1, \theta, \beta_1, F_2$ and $\frac{h_2}{h_1}$ -----	A.3
2.3 Theoretical Correlation Between Analogous Water and Air Characteristics for $F_1 = M_1$ -----	A.4
3.1(a) Model Used on the Experiments -----	A.5
3.1(b) Model Used on the Experiments -----	A.6
3.2 Hydraulic Simulator-----	A.7
4.1 Best Fit of Water Depth vs. Head Height -----	A.8
4.2 Velocity Measurements Using High Speed Camera as Compared to the Velocity from the Energy Equation -----	A.9
4.3 Froude Number vs. Head Height -----	A.10
4.4 Uniform Velocity vs. Head Height-----	A.11
4.5 Pressure Ratio Sensitivity as a Function of Mach Number -----	A.12
4.6 Pressure Coefficient Sensitivity as a Function of Mach Number ----	A.13
4.7 Water Depth Measurements on Model -----	A.14
5.1 Pressure Ratio for Surface 2 of Case 1 -----	A.15
5.2 Pressure Ratio for Surface 3 of Case 1 -----	A.16
5.3 Pressure Ratio for Surface 4 of Case 1 -----	A.17
5.4 Pressure Ratio for Surface 5 of Case 1 -----	A.18
5.5 Pressure Ratio for Surface 2 of Case 2 -----	A.19
5.6 Pressure Ratio for Surface 3 of Case 2 -----	A.20

Figure	Page
5.7 Pressure Ratio for Surface 4 of Case 2 -----	A.21
5.8 Pressure Ratio for Surface 5 of Case 2 -----	A.22
5.9 Pressure Coefficient for Surface 2 of Case 1 -----	A.23
5.10 Pressure Coefficient for Surface 3 of Case 1 -----	A.24
5.11 Pressure Coefficient for Surface 4 of Case 1 -----	A.25
5.12 Pressure Coefficient for Surface 5 of Case 1 -----	A.26
5.13 Pressure Coefficient for Surface 2 of Case 2 -----	A.27
5.14 Pressure Coefficient for Surface 3 of Case 2 -----	A.28
5.15 Pressure Coefficient for Surface 4 of Case 2 -----	A.29
5.16 Pressure Coefficient for Surface 5 of Case 2 -----	A.30
5.17 A Comparison of Pressure Ratio on Surface 2 for Different Motion Profiles. Position 1 -----	A.31
5.18 A Comparison of Pressure Ratio on Surface 4 for Different Motion Profiles. Position 1 -----	A.32
5.19 A Comparison of Pressure Ratio on Surface 2 for Different Motion Profiles. Position 2 -----	A.33
5.20 A Comparison of Pressure Ratio on Surface 4 for Different Motion Profiles. Position 2 -----	A.34
5.21 A Comparison of Pressure Coefficient on Surface 2 for Different Motion Profiles. Position 1 -----	A.35
5.22 A Comparison of Pressure Coefficient on Surface 4 for Different Motion Profiles. Position 1 -----	A.36
5.23 A Comparison of Pressure Coefficient on Surface 2 for Different Motion Profiles. Position 2 -----	A.37
5.24 A Comparison of Pressure Coefficient on Surface 4 for Different Motion Profiles. Position 2 -----	A.38

Figure	Page
5.25 Analysis of Flow for Capsule/Fuselage System -----	A.39
B.1 Capillary Rise in a Tube -----	B.1
B.2 Velocity Measurements Using Pitot Tube as Compared to the Velocity from the Energy Equation -----	B.2
B.3 Velocity Differential vs. Angle of Inclination of Table. Head Height of 20 mm -----	B.3
B.4 Velocity Differential vs. Angle of Inclination of Table. Head Height of 40 mm -----	B.4
B.5 Velocity Differential vs. Angle of Inclination of Table. Head Height of 50 mm -----	B.5
B.6 Velocity Differential vs. Angle of Inclination of Table. Head Height of 60 mm -----	B.6
B.7 Velocity Differential vs. Angle of Inclination of Table. Head Height of 80 mm -----	B.7
B.8(a) Method of Determination of the Uncertainty in the Velocity Differential for the Reference Head Heights Between 50 and 80 mm	B.8
B.8(b) Method of Determination of the Uncertainty in the Velocity Differential for the Reference Head Heights Between 20 and 40 mm	B.9
B.9 Determination of Velocity Using High Speed Camera -----	B.10
B.10 Positive and Negative Angle of Inclination for the Table -----	B.11

List of Tables

Table	Page
2.1 Summary of Analogous Variables-----	2.8
2.2 Calculation of Pressure Ratio Using Direct and Modified Analogy -----	2.18
2.3 Difference in the Theoretical Correlation of Water Depth and Density Ratios -----	2.19
4.1 Value of C_d for Reference Heights -----	4.4
4.2 Numerical Values of Fr , h_s , V , θ vs. h -----	4.6
4.3 Associated Errors of Fr -----	4.15
4.4 Effect of a 5% Variation in Fr on Height Ratio -----	4.16
4.5 Variation of the Aerodynamic Parameters with a 5% Variation in Mach Number -----	4.18
4.6 Experimental Runs for Capsule-----	4.20
4.7 Cases Studied for Capsule/Fuselage System. -----	4.21
4.8 Conditions After the Shock Wave Produced by the Capsule -----	4.23
5.1 Theoretical Values of Ratio of Different Flow Parameters Across a Compression Shock Wave-----	5.2
5.2 Theoretical Values of the Ratio of Different Flow Parameters Across an Expansion Wave -----	5.2
5.3 Theoretical Results of Hydraulic Parameters for Surfaces 4 and 2 -----	5.7
5.4 Theoretical Results Using the Shock-Expansion Theory for Surfaces 4 and 2 -----	5.8
5.5 Experimental Results of Water Depth Ratio for Surfaces 4 and 2 -----	5.8

Table	Page
5.6 Theoretical Results of Pressure and Density Ratio	
for Static and Dynamic Case 1-----	5.9
5.7 Experimental Results of Pressure and Density Ratios	
for Static and Dynamic Case 1-----	5.10
5.8 Experimental Values of the Ratio of Different Flow Parameters	
Across a "Compression Shock Wave", Surface 2 - Case 1 -----	B.1
5.9 Experimental Values of the Ratio of Different Flow Parameters	
Across a "Compression Shock Wave", Surface 4 - Case 1 -----	B.2
5.10 Experimental Values of the Ratio of Different Flow Parameters	
Across a "Compression Shock Wave", Surface 2 - Case 2 -----	B.3
5.11 Experimental Values of the Ratio of Different Flow Parameters	
Across a "Compression Shock Wave", Surface 4 - Case 2 -----	B.4
5.12 Experimental Values of the Ratio of Different Flow Parameters	
Across a Expansion Wave, Surface 3 - Case 1 -----	B.5
5.13 Experimental Values of the Ratio of Different Flow Parameters	
Across a Expansion Wave, Surface 5 - Case 1 -----	B.6
5.14 Experimental Values of the Ratio of Different Flow Parameters	
Across a Expansion Wave, Surface 3 - Case 2 -----	B.7
5.15 Experimental Values of the Ratio of Different Flow Parameters	
Across a Expansion Wave, Surface 5 - Case 2 -----	B.8
5.16 Experimental Values of the Ratio of Different Flow Parameters	
Across a "Compression Shock Wave",	
Surface 2 - Position 1 - Static Conditions -----	B.9
5.17 Experimental Values of the Ratio of Different Flow Parameters	
Across a "Compression Shock Wave",	
Surface 2 - Position 1 - Velocity 1 -----	B.10

Table	Page
5.18 Experimental Values of the Ratio of Different Flow Parameters Across a "Compression Shock Wave", Surface 2 - Position 1 - Velocity 2 -----	B.11
5.19 Experimental Values of the Ratio of Different Flow Parameters Across a "Compression Shock Wave", Surface 4 - Position 1 - Static Conditions -----	B.12
5.20 Experimental Values of the Ratio of Different Flow Parameters Across a "Compression Shock Wave", Surface 4 - Position 1 - Velocity 1 -----	B.13
5.21 Experimental Values of the Ratio of Different Flow Parameters Across a "Compression Shock Wave", Surface 4 - Position 1 - Velocity 2 -----	B.14
5.22 Experimental Values of the Ratio of Different Flow Parameters Across a "Compression Shock Wave", Surface 2 - Position 2 - Static Conditions -----	B.15
5.23 Experimental Values of the Ratio of Different Flow Parameters Across a "Compression Shock Wave", Surface 2 - Position 2 - Velocity 1 -----	B.16
5.24 Experimental Values of the Ratio of Different Flow Parameters Across a "Compression Shock Wave", Surface 2 - Position 2 - Velocity 2 -----	B.17
5.25 Experimental Values of the Ratio of Different Flow Parameters Across a "Compression Shock Wave", Surface 4 - Position 2 - Static Conditions -----	B.18

Table	Page
5.26 Experimental Values of the Ratio of Different Flow Parameters Across a "Compression Shock Wave", Surface 4 - Position 2 - Velocity 1 -----	B.19
5.27 Experimental Values of the Ratio of Different Flow Parameters Across a "Compression Shock Wave", Surface 4 - Position 2 - Velocity 2 -----	B.20
1.B Measurements of Water Depth vs. Head Height at 0.1m -----	C.2
2.B Measurements of Water Depth vs. Head Height at 0.25m -----	C.2
3.B Velocity Calculations Using Pitot Tube of 1 mm Diameter -----	C.4
4.B Velocity Using High Speed Camera -----	C.6
5.B Velocity vs. Angle of Inclination of Table -----	C.6
6.B Velocity Differential of Reference Head Heights -----	C.7

List of Symbols

<u>Symbol</u>	<u>Description</u>	<u>Units</u>
a	Sonic Velocity	m/s
c	Celerity of a Wave	m/s
C_D	Drag Coefficient	
C_L	Lift Coefficient	
C_M	Moment Coefficient	
C_p	Pressure Coefficient	
D	Drag	N
g	Gravity	m/s ²
h	Height	mm
k	Ratio of Specific Heat Ratios	
L	Lift	N
M	Mach Number	
M	Moment	N-m
n	Manning's Friction Coefficient	s/m ^{1/3}
p	Pressure	Pa
q	Dynamic Pressure	Pa
R	Universal Gas Constant	J/kmol-K
S_o	Slope of Channel Bed	rad
T	Surface Tension	N/m
T	Temperature	K
y	Coordinate Direction	m
x	Coordinate Direction	m

<u>Symbol</u>	<u>Description</u>	<u>Units</u>
Fr	Froude Number	
L	Reference length	
Re	Reynolds Number	
T	Surface tension	N/m
V	Velocity	m/s
<u>Greek Letters</u>		
θ	Flow deflection angle in water	degrees
ν	Angle of Expansion Wave	degrees
δ	Max. flow deflection angle in air	degrees
ε	Max. shock wave angle	degrees
π	Numerical constant	
σ	Standard deviation	
λ	Wave length	m
β_1	Hydraulic jump wave angle	degrees
ρ	Density	kg/m ³
γ	Specific Heat Ratio	
μ	Dynamic Viscosity	Pa-s
ν	Kinematic Viscosity	m ² /s
ϕ	Angle of Inclination of Table	degrees

Subscripts

∞	Free Stream Conditions
o	Reference Conditions
1,i	Conditions Before Shock or Expansion Wave
2,j	Conditions After Shock or Expansion Wave
b	Flow Deflection Angle for Expansion in Water

Abstract

In the present research, the flow field associated with the ejection of a crew capsule from the fuselage of a high speed generic aircraft was experimentally investigated by means of the modified gas hydraulic analogy. For this, an existing hydraulic simulator was calibrated and modified to adapt it to the needs of the experiment. The analogy was evaluated for a five-sided capsule alone, and good quantitative agreement with the 2-D shock-expansion theory was obtained. It was found that the size of the model played a key role in the determination of good quantitative data. The analysis of the capsule interacting with a fuselage was made considering it at fixed vertical positions from the fuselage and moving with respect to the fuselage at different constant speeds. A clear difference in water depth ratio distribution on the surfaces of the capsule was found between the static and dynamic conditions and also differences occurred for the various velocities of separation. The agreement between theory and experiment was fair. It was concluded that larger models are needed to get good quantitative agreement between theory and experiment and that any separation study should be made applying a dynamic model.

CALIBRATION AND INITIAL TESTING OF A NEW HYDRAULIC SIMULATOR

I. Introduction

Safe emergency crew escape from an imperiled aircraft is a matter of great concern to any Air Force. The U.S. Air Force through the Air crew Protection Branch of Wright Laboratories located in WPAFB performs continuing research in this area.

One of the systems that has been subject to most extensive analysis is the F-111, the only aircraft of the USAF operational inventory which utilizes a capsule ejection system. In spite of the considerable amount of information that has been gathered for the different flight conditions, during the time the airplane has been in the Air Force, data have never been gathered on the separation aerodynamic characteristics of the capsule. This is a very complex phenomenon involving unsteady, compressible aerodynamics coupled with the dynamics of the ejected escape capsule and therefore does not easily lend itself to analytical or experimental modeling. The high cost of wind tunnel and flight tests limits testing of two body separation to basically two approaches: analytical methods and modeling techniques. The former can be accomplished using Computational Fluids Dynamics (CFD). Current CFD techniques, however, cannot simulate unsteady, two body separation. The latter, on the other hand, could be carried out applying the so called Gas Hydraulic Analogy (GHA), which presents an affordable method to model the complex aerodynamics of the separating bodies.

In order to analyze the feasibility of applying the analogy for the study of this particular problem, a two dimensional model of the forebody of a generic aircraft generally resembling that of the F-111 was built and utilized in conjunction with a hydraulic simulator (water table) located in room 104 of the Crew Escape Section, building 255 at WPAFB

1.2 Objective and Scope: The present research analyzes the feasibility of studying the separation aerodynamics of the crew capsule of a generic aircraft during the early stages of the ejection sequence. Its two main objectives were to study the aerodynamic parameters affecting the motion of the capsule through the application of the so-called "modified hydraulic analogy", with emphasis on those parameters permitting the prediction of the forces acting on its surface, and the difference in the value of the aerodynamic parameters for static and dynamic conditions. These data, once validated, can help to increase the knowledge in a phenomenon that is, at present, not well understood and that is also particularly difficult to model.

II. Theory Of The Gas Hydraulic Analogy

2.1. Introduction

The gas hydraulic analogy (G.H.A.), establishes an analogy between inviscid, non heat conducting, two-dimensional compressible flow of air with the incompressible, non heat conducting flow of water with a free surface.

The analogy was first used in 1911 when Isaacsen gave an experimental demonstration of it and "applied it to the study of nozzle flow and to sudden expansions in ducts" [Ref 12]. The rigorous mathematical substantiation, however, was presented only in 1938 when E. Preiswerk published his Doctoral Dissertation.

Little was done on the analogy until 1947, but beginning in that year several studies were conducted on the validity of the analogy to simulate supersonic flow conditions. Among the most conclusive of all the studies carried out, was the extensive study of Ippen et al. at the M.I.T. (1951-1952), which is often cited in the pertinent literature. In this study, the validity of the analogy for transonic and supersonic flow simulation was firmly established both qualitatively and quantitatively.

The G.H.A. method has a number of advantages: it offers a relatively easy implementation of analog tests, is visually clear, inexpensive and provides information rapidly, all of this is due to its ability to slow down dynamic events. It also allows the modeling of complex non stationary problems of fluid dynamics which are difficult if not impossible to solve with other simulation techniques. The most relevant limitations, on the other hand, are the fact that the analogy mathematically holds exactly only for a specific heat ratio of two, when vertical

accelerations are considered negligible and for a water depth slightly larger than one half of a centimeter.

The analogy has been shown to be valid for the simulation of not only supersonic flow but also of subsonic flow, both external and internal. Also the analogy has been applied to some hypersonic configurations. This has been done, however, only for qualitative analysis since the theory breaks down when high temperature ratios are considered and chemical reactions take place in the flow.

As can be seen, considerable effort has been devoted to the development of the analogy, and its validity as a useful experimental tool has been firmly established.

In the next section the formal derivation of the analogy will be presented along with the necessary modifications that make it applicable to obtain quantitative data.

2.2 Derivation of the Analogy

This derivation generally follows that of reference 12. In this derivation, only the mass and momentum conservation equations are necessary; the energy equation does not provide new relationships.

2.2.1 Gas Equations (Compressible Flow)

a. General Continuity

$$\frac{\partial \rho}{\partial t} + \frac{\partial(\rho v_i)}{\partial x_i} = 0 \quad (2.2.1)$$

b. General Momentum

$$\frac{\partial v_i}{\partial t} + v_j \frac{\partial v_i}{\partial x_j} = \frac{1}{\rho} \left[-\frac{\partial p}{\partial x_i} + \mu \frac{\partial}{\partial x_j} \left(\frac{\partial v_i}{\partial x_j} + \frac{\partial v_j}{\partial x_i} \right) \right] - g \left(\frac{\partial x_3}{\partial x_i} \right) \quad (2.2.2)$$

Assuming isentropic flow, the viscosity term and the pressure term can be eliminated from Eqn (2.2.2). The pressure is eliminated by means of Eqn. (2.2.3):

$$\frac{\partial p}{\partial x_i} = \gamma \left(\frac{p_o}{\rho_o^\gamma} \right) \rho^{\gamma-1} \frac{\partial \rho}{\partial x_i} \quad (2.2.3)$$

With this Eqn. (2.2.2) reduces to:

$$\frac{\partial v_i}{\partial t} + v_j \frac{\partial v_j}{\partial x_i} = -\gamma \left[\frac{p_o}{\rho_o^\gamma} \right] \rho^{\gamma-2} \frac{\partial \rho}{\partial x_i} - g \frac{\partial x_3}{\partial x_i} \quad (2.2.4)$$

These equations are now non-dimensionalized. For this, the following substitutions are made:

$$\bar{v}_i = \frac{v_i}{v_o} \quad \bar{\rho} = \frac{\rho}{\rho_o} \quad \bar{x}_i = \frac{x_i}{L} \quad \bar{g} = \frac{g}{g_o} \quad \bar{t} = t \frac{v_o}{L} \quad (2.2.5)$$

where all barred quantities are dimensionless and v_o , ρ_o , L and g_o are reference quantities.

Substituting Eqs. (2.2.5) into Eqn. (2.2.1) and Eqn. (2.2.2), yields:

$$\frac{\partial \bar{\rho}}{\partial \bar{t}} + \frac{\partial (\bar{\rho} \bar{v}_i)}{\partial \bar{x}_i} = 0 \quad (2.2.6)$$

$$-\frac{\partial \bar{\rho}}{\partial \bar{x}_i} = \frac{v_o^2}{\gamma \frac{p_o}{\rho_o}} (\bar{\rho}^{(2-\gamma)}) \left[\frac{\partial \bar{v}_i}{\partial \bar{t}} + \bar{v}_j \frac{\partial \bar{v}_j}{\partial \bar{x}_i} \right] \quad (2.2.7)$$

where the last term of Eqn. (2.2.4) has vanished based on the assumption that the effects of gravity are small.

For an ideal gas:

$$\frac{p_o}{\rho_o} = RT_o \quad (2.2.8)$$

$$a_o = \sqrt{\gamma RT_o} \quad (2.2.9)$$

where a_o is the speed of sound at the reference conditions. If use is made of the definition of Mach Number:

$$M_o = \frac{v_o}{a_o} \quad (2.2.10)$$

Eqn. (2.2.7) can be written as:

$$-\frac{\partial \bar{\rho}}{\partial x_i} = (\bar{\rho}^{-(2-\gamma)}) M_o^2 \left[\frac{\partial \bar{v}_i}{\partial t} + \bar{v}_j \frac{\partial \bar{v}_j}{\partial x_i} \right] \quad (2.2.11)$$

where $i, j = 1, 2$ since neither water nor air is considered to have a component of momentum in the x_3 direction, i. e., it is a 2-D flow.

2.2.2 Hydrodynamic Equations (Incompressible Flow)

For the incompressible flow of a free surface under the influence of gravity.

a. Continuity Equation

$$\frac{\partial h}{\partial t} + \frac{\partial (v_i h)}{\partial x_j} = 0 \quad (2.2.12)$$

b. Momentum Equation

Taking the momentum equation in general form (Eqn. (2.2.2)) and applying the conditions of irrotationallity, $\frac{\partial v_i}{\partial x_j} = \frac{\partial v_j}{\partial x_i}$, incompressibility, $\frac{\partial v_j}{\partial x_j} = 0$, and negligible friction $\mu = 0$, the equation for the x_3 direction can be written as:

$$\frac{\partial v_3}{\partial t} + v_1 \frac{\partial v_1}{\partial x_3} + v_2 \frac{\partial v_2}{\partial x_3} + v_3 \frac{\partial v_3}{\partial x_3} = -\frac{1}{\rho} \frac{\partial p}{\partial x_3} - g \frac{\partial x_3}{\partial x_3} \quad (2.2.13)$$

or in more compact form as:

$$\frac{\partial v_3}{\partial t} + \frac{d}{dx_3} \left[\frac{|v|^2}{2} \right] = -\frac{1}{\rho} \frac{\partial p}{\partial x_3} - g \quad (2.2.14)$$

After integration with respect to x_3 and some manipulation, Eqn. (2.2.14) becomes:

$$\frac{\partial}{\partial t} \int_o^y v_3 dy - (v_3)_y \frac{\partial y}{\partial t} - \left[\frac{|v|^2}{2} \right]_y + \left[\frac{|v|^2}{2} \right]_o = -\frac{1}{\rho} [p_o - p_y] - gy \quad (2.2.15)$$

where "y" refers to an arbitrary head in the fluid and "o" to the bottom of the fluid layer.

Assuming the vertical velocity to be negligible, Eqn. (2.2.15) becomes:

$$p_y = \rho gy + \rho \left[\left(\frac{|v|^2}{2} \right)_o - \left(\frac{|v|^2}{2} \right)_y \right] + p_o \quad (2.2.16)$$

If it is further assumed that the velocity distribution in the x_3 direction is uniform, then the second term in the RHS of Eqn. (2.2.16) vanishes and the pressure becomes hydrostatic:

$$p_y = \rho gy = \rho g(h - x_3) + p_o \quad (2.2.17)$$

With further manipulations, the final expressions of the momentum equation for the x_1 and x_2 directions are obtained:

$$\frac{\partial v_i}{\partial t} + \frac{1}{2} \frac{\partial}{\partial x_i} (|v|^2) = -g \frac{\partial h}{\partial x_i} \quad (2.2.18)$$

where $i=1, 2$ and use has been made of the fact that $\frac{\partial p}{\partial x_i} = \rho g \frac{\partial h}{\partial x_i}$ from Eqn. (2.2.17). At this point, Eqs. (2.2.12) and (2.2.18) are non-dimensionalized using the following transformations:

$$\bar{v}_i = \frac{v_i}{v_o} \quad \bar{x}_i = \frac{x_i}{L} \quad \bar{h} = \frac{h}{h_o} \quad \bar{t} = t \frac{v_o}{L} \quad (2.2.19)$$

The continuity equation becomes:

$$\frac{\partial \bar{h}}{\partial \bar{t}} + \frac{(\partial \bar{v}_i \bar{h})}{\partial \bar{x}_i} = 0 \quad (2.2.20)$$

The momentum equation can be written as:

$$\frac{v_o^2}{h_o} \left[\frac{\partial \bar{v}_i}{\partial \bar{t}} = \bar{v}_j \frac{\partial \bar{v}_j}{\partial \bar{x}_i} \right] = -g \frac{\partial \bar{h}}{\partial \bar{x}_i} \quad (2.2.21)$$

Making use of the definition of Froude Number:

$$Fr_o = \frac{v_o}{\sqrt{gh_o}} \quad (2.2.22)$$

Eqn. (2.2.21) becomes:

$$\frac{\partial \bar{h}}{\partial x_i} + Fr_o^2 \left[\frac{\partial \bar{v}_i}{\partial \bar{t}} + \bar{v}_j \frac{\partial \bar{v}_i}{\partial x_j} \right] = 0 \quad (2.2.23)$$

The corresponding equations are now compared to establish the analogy. Comparison of Eqs. (2.2.6) and (2.2.20) shows that for the analogy to hold, the non dimensional height of the water and the non dimensional density in the compressible flow have to be equal.

A comparison of the momentum Eqs. (2.2.11) and (2.2.23) shows that if the reference Mach Number in the compressible fluids is numerically equal to the reference Froude Number in the Hydraulic fluid, then the analogy is exact for $\gamma = 2$.

Furthermore if the expression for isentropic gas is considered:

$$\frac{p_o}{p} = \left(\frac{\rho_o}{\rho} \right)^\gamma \quad (2.2.24)$$

$$\frac{t_o}{t} = \left(\frac{p_o}{p} \right)^{\frac{(\gamma-1)}{\gamma}} \quad (2.2.25)$$

It is noted that for $\gamma = 2$:

$$\frac{t_o}{t} = \frac{\rho_o}{\rho} = \left(\frac{p_o}{p} \right)^{\frac{1}{2}} \quad (2.2.26)$$

Summarizing the analogous variables gives the following:

Table 2.1 Summary of Analogous Variables

WATER	GAS
$\sqrt{gh_o}$	$\sqrt{\gamma RT}$
v_i	v_i
\bar{h}	$\bar{\rho}, \bar{T}$
$(\bar{h})^2$	\bar{p}
\bar{t}	\bar{t}

It can be noted here that the derivation did not require the use of the energy equation. In this respect, it can be shown [Ref. 1] that the energy conditions are identical if $\bar{h} = \bar{\rho}$ and $\frac{p_o}{p} = \left(\frac{\rho_o}{\rho}\right)^2$. These conditions are satisfied by Eqs. (2.2.25) and (2.2.26) and do not result in any new relationship.

2.3 Consideration of Simplifying Assumptions

a. Flow is inviscid:

Even though no real flow is completely inviscid, this assumption is valid when the viscosity effects are small compared to other forces. The well known Reynolds number allows the characterization of the flow in this regard. Since it is a ratio of the inertia forces to the viscous forces, the higher its value, the more inviscidly the flow behaves. In the experiments carried out here, the range of free stream Reynolds numbers for the model was between 8×10^4 and 1.8×10^5 .

If, in spite of the high values of the Reynolds number, it is desired to model the viscous forces, the Reynolds Numbers in the two flows have to match.

$$\frac{V_w L_w}{\nu_w} = \frac{V_a L_a}{\nu_a} \quad (2.3.1)$$

where L_w and L_a are characteristic lengths for the body in water and in air respectively. From Eqn. (2.3.1), the following expression is obtained after substituting for the Froude and Mach numbers:

$$\frac{Fr \sqrt{gh} L_w}{\nu_w} = \frac{M \sqrt{\gamma RT} L_a}{\nu_a} \quad (2.3.2)$$

Since the analogy requires that the Froude and Mach numbers be numerically equal, Eqn. (2.3.2) can be written as:

$$\left(\frac{\nu_a}{\nu_w} \right)^2 \frac{gh}{\gamma RT} = \left(\frac{L_a}{L_w} \right)^2 \quad (2.3.3)$$

It can be seen that the scale ratio $\left(\frac{L_a}{L_w} \right)$ and the depth of the water can be independently varied, whereas the ratio of kinematic viscosity is temperature dependent.

Upon analysis of this expression it can be said that in order to obtain dynamic similarity in the viscous effects, the only parameter that can be modified without altering the flow conditions in each case is the length scale. This is because the water depth has to be made larger if the similarity is to be obtained by varying it, which invalidates the condition of shallowness of the water. Also the temperature of the air has to be increased beyond the range of real operating

conditions if dynamic similarity is to be obtained by this means. This, in turn, changes the ratio of kinematic viscosity. Finally if only the scale ratio is varied, dynamic similarity in the viscous forces is obtained when the size of the model in air is considerably smaller than that of the model in water. This imposes the further restriction for the model in air that its roughness should be scaled down in the same ratio if true similarity is to be achieved, imposing a further limit on the scale that can be used.

b. Flow is Irrotational:

For this condition to exist, it is necessary that the first condition of inviscid flow also hold. Since the viscosity effects seem small because the inertia forces are much larger than the viscous forces, the assumption of zero vorticity is valid.

c. Flow is Isentropic:

If the flow is inviscid and no appreciable heat transfer occurs, the assumption of isentropic flow is reasonable. The experiments were all performed in ambient water temperature and pressure so heat transfer was small in the test program.

d. Flow is Two-dimensional:

It was shown that if the velocity distribution over the depth is constant, the pressure distribution is hydrostatic. Substituting this condition in the "x" and "y" momentum equations for water, a form of the momentum equation is obtained that is analogous to the gas flow equations. So for the analogy to exist, this condition has to be met.

e. The Specific Heat Ratio γ is Two:

It was shown that for the analogy to produce perfect modeling, the specific heat ratio had to be two.

Since air has a specific heat ratio of 1.4, this seems to impose a serious restriction if quantitative data is desired. It is shown subsequently, however, that this restriction is not severe if the so-called modified analogy is applied.

2.4 Investigation of the Analogy

In the previous sections, the analogy was mathematically derived. In this section, an analysis of its validity is presented. In order to facilitate this, the necessary equations for hydraulic jumps and compression shocks as well as expansion waves for both water and air are presented. Details of the derivation of the equations can be found in references 1, 2 and 6.

The hydrodynamic problem will be considered first. The expression for the normal component of velocity in terms of the depths before (h_1) and after (h_2) a hydraulic jump is given by:

$$V_{n1} = \sqrt{gh_1} \sqrt{\frac{h_2}{h_1} \frac{1}{2} \left(1 + \frac{h_2}{h_1} \right)} \quad (2.4.1)$$

or in terms of Froude Number it can be written as:

$$\frac{h_2}{h_1} = \frac{1}{2} \left(\sqrt{8F_{n1}^2 + 1} - 1 \right) \quad (2.4.2)$$

where $F_{n1} = F_1 \sin \beta_1$

When considering an oblique hydraulic jump which occurs when a vertical boundary is deflected inward to a supercritical flow (Fig 1.a), several relations can be obtained for conditions before and after the jump:

$$\frac{h_1}{h_2} = \frac{2}{\sqrt{1 + 8(F_1)^2 \sin^2 \beta_1} - 1} \quad (2.4.3)$$

$$\tan \theta = \frac{\tan \beta_1 \left(\sqrt{1 + 8(F_1)^2 \sin^2 \beta_1} - 3 \right)}{2 \tan^2 \beta_1 - 1 + \sqrt{1 + 8(F_1)^2 \sin^2 \beta_1}} \quad (2.4.4)$$

$$(F_2)^2 = \frac{h_1}{h_2} \left[(F_1)^2 - \frac{1}{2} \frac{h_1}{h_2} \left(\frac{h_2}{h_1} - 1 \right) \left(\frac{h_2}{h_1} + 1 \right)^2 \right] \quad (2.4.5)$$

Fig. 2.2 shows a graphical solution for these equations. A QBASIC code was developed to obtain the same parameters with a more adequate resolution.

For the case of an expanding wave, which occurs when a vertical boundary is deflected outward from supercritical flow, a gradual decrease in the depth of the flow occurs. (Fig. 1.b) This gradual decrease is defined by lines of constant depth radiating from the boundary discontinuity and no perceptible energy dissipation occurs. This fan shaped region is delineated by the angles β_1 and β_2 measured with respect to the initial and final flow deflection. These angles are given by: $\beta_1 = \sin^{-1} \frac{1}{F_1}$ and $\beta_2 = \sin^{-1} \frac{1}{F_2}$.

If F_1 the Froude Number before the expansion, h_1 the height before the expansion and θ_b the angle of deflection of the flow that produces the expansion are known, then the equation to be used is:

$$\theta_1 + \theta = \sqrt{3} \tan^{-1} \frac{\sqrt{3}}{\sqrt{F^2 - 1}} - \tan^{-1} \frac{1}{\sqrt{F^2 - 1}} \quad (2.4.6)$$

where θ , the integration constant, takes on the following values:

$$\theta = 0 \text{ when } F = F_1$$

$$\theta = \theta_b \text{ when } F = F_2$$

Equating the specific energy heads before and after the expansion and dividing through by h_1 , the following expression is obtained:

$$\frac{h_2}{h_1} = \frac{F_1^2 + 2}{F_2^2 + 2} \quad (2.4.7)$$

For the case of air, the following expressions are obtained:

The density ratio is given by:

$$\frac{\rho_2}{\rho_1} = \frac{M_1^2 \sin^2 \beta (\gamma + 1)}{M_1^2 \sin^2 \beta (\gamma - 1) + 2} \quad (2.4.8)$$

This equation can be worked out to give the density ratio in terms of β angle of shock wave and δ flow deflection angle, which is exactly identical to that obtained for the density ratio across an oblique jump.

Temperature and pressure ratios are given by:

$$\frac{T_2}{T_1} = \frac{\left(M_1^2 \sin^2 \beta - \frac{\gamma - 1}{\gamma - 2} \right) \left(M_1^2 \sin^2 \beta + \frac{2}{\gamma - 1} \right)}{\frac{(\gamma + 1)^2}{2\gamma(\gamma - 1)} M_1^2 \sin^2 \beta} \quad (2.4.9)$$

$$\frac{p_2}{p_1} = \frac{\left(M_1^2 \sin^2 \beta - \frac{\gamma - 1}{2\gamma} \right)}{\frac{\gamma + 1}{2\gamma}} \quad (2.4.10)$$

Or in more compact form:

$$\frac{T_2}{T_1} = \left(\frac{P_2}{P_1} \right) \left(\frac{\rho_1}{\rho_2} \right) \quad (2.4.11)$$

$$\frac{p_2}{p_1} = \frac{\frac{(\gamma + 1)}{(\gamma - 1)} \frac{\rho_2}{\rho_1} - 1}{\frac{(\gamma + 1)}{(\gamma - 1)} - \frac{\rho_2}{\rho_1}} \quad (2.4.12)$$

Finally the value of Mach Number after the shock wave is given by:

$$M_2 = \sqrt{M_1^2 - \frac{2 \left(1 - \left(\frac{\rho_2}{\rho_1} \right)^2 \right)}{\frac{\rho_1}{\rho_2} (\gamma + 1) - (\gamma - 1)}} \left(\frac{p_1}{p_2} \frac{\rho_2}{\rho_1} \right) \quad (2.4.13)$$

For changes occurring in the absence of shock waves, isentropic flow is assumed. In this case,

$$\frac{p_2}{p_1} = \left(\frac{\rho_2}{\rho_1} \right)^\gamma \quad (2.4.14)$$

and from the perfect gas law,

$$\frac{T_2}{T_1} = \left(\frac{\rho_2}{\rho_1} \right)^{\gamma-1} \quad (2.4.15)$$

The value of the local Mach Number is obtained from the energy equation,

$$\frac{V_1^2}{2} + \frac{\gamma}{\gamma-1} \frac{p_1}{\rho_1} = \frac{V_2^2}{2} + \frac{\gamma}{\gamma-1} \frac{p_2}{\rho_2} \quad (2.4.16)$$

by use of Eqn. (2.4.14)

$$\frac{M_1^2 + \frac{2}{\gamma-1}}{M_2^2 + \frac{2}{\gamma-1}} = \left(\frac{\rho_2}{\rho_1} \right)^{\gamma-1} \quad (2.4.17)$$

so that finally M_2 may be expressed in terms of the density ratio and the initial Mach Number:

$$M_2 = \sqrt{\frac{M_1^2 + \frac{2}{(\gamma-1)}}{\left(\frac{\rho_2}{\rho_1}\right)^{\gamma-1}} - \frac{2}{(\gamma-1)}} \quad (2.4.18)$$

Now that the equations for oblique shock and expansion waves have been established, a critical examination of the analogy is made.

Upon observation of the equations developed in Section 2.2, two restrictions clearly show up. The first one is the fact that the analogy is only applicable to one or two dimensional flow. This is because the water depth (z axis) represents the density, so only two dimensions remain for the geometric representations of the flow.

The second restriction occurs because the analogy equations hold strictly for the ideal, isentropic flow of a gas with $\gamma = 2.0$

Other restrictions that are not obvious from the analysis of the equations developed so far are presented now. The internal energy equivalency is not exact because in a gas the change in internal energy is used to increase the entropy as well as affect the dynamic properties of the flow whereas in water no further influence on the flow conditions occur [Refs. 1, 3].

Another difficulty arises from the fact that the wave velocity of the surface-wave propagation is not exactly given by Eqn. (2.4.19), but rather by Eqn. (2.4.20) below [Ref. 3]

$$c = \sqrt{gh} \quad (2.4.19)$$

$$c = \sqrt{\left(\frac{g\lambda}{2\pi} + \frac{2\pi T}{\rho\lambda}\right) \tan \frac{2\pi h}{\lambda}} \quad (2.4.20)$$

where:

g = gravity (m/s^2)

λ = wave length (m)

T = surface tension (N/m)

ρ = density (N/m^3)

Applying a series approximation to Eqn. (2.4.20), it can be written as:

$$c = \sqrt{gh} \left[1 + 2 \frac{\pi^2 T}{g\rho\lambda^2} + O\left(\left(\frac{h}{\lambda}\right)^2\right) \right] \quad (2.4.21)$$

From Eqn. (2.4.21) it is observed that unless $\lambda \gg h$ or $h \rightarrow 0$, the vertical acceleration is not negligible. Also, for very short waves, the surface tension T predominates and the so-called capillary ripples appear. These are entirely a surface phenomena and are not part of the analogy. If the surface tension is considered negligible the following is verified regarding Eqn. (2.4.20): [Ref. 7]

$$\text{for } \lambda < 2h \quad \tan \frac{2\pi h}{\lambda} \cong 1 \Rightarrow c = \sqrt{\frac{g\lambda}{2\pi}}$$

(2.4.22)

$$\text{for } \lambda > 40h \quad \tan \frac{2\pi h}{\lambda} = \frac{2\pi h}{\lambda} \Rightarrow c = \sqrt{gh} \quad (2.4.23)$$

Laitone showed [Ref. 3] that c is independent of λ only for water depths of the order of 0.00635m (0.25 in).

2.5 Modification of the Analogy for Quantitative Application

As was shown in section 2.2.3, the analogy can be established by direct comparison of the fundamental equations of water and air and a list of the relationships is shown in Table 2.1. This set of relationships will be termed "Direct Analogy".

As a way of improving the theoretical agreement of the analogy, a modification to the analogy was first proposed by Ippen et al. [Ref. 1] This modification can be better understood by observing Fig. 2.3 which shows the theoretical correlation between analogous water and air characteristics for a particular case. It is clear from the figure that a strict adherence to the direct analogy does not seem desirable since there is good correlation only between the height ratio of water and the density ratio of air. It is therefore "proposed to use the depth ratio only to determine the analogous density ratio and then to calculate with this density ratio the temperature, pressure and local Mach Number values by means of the aerodynamic relations". In other words, if it is desired to make use of the analogy to get quantitative results, it should be considered it to hold only as far as air density and water depth ratios are concerned. In order to illustrate this point, a 10° flow deflection angle is considered for three reference initial Froude and Mach numbers and the direct and modified analogy are applied to get the pressure ratio.

Table 2.2 Calculation of Pressure Ratio Using

Direct and Modified Analogy

Initial M=F	$\frac{h_2}{h_1}$	$\frac{\rho_2}{\rho_1}$	$\left(\frac{p_2}{p_1}\right)_T$ (1)	$\left(\frac{p_2}{p_1}\right)_M$ (2)	% Differ. (1-2)	$\left(\frac{p_2}{p_1}\right)_D$ (3)	% Differ. (1-3)
2.0	1.443	1.458	1.706	1.680	1.5	2.082	-22.0
3.0	1.612	1.655	2.055	1.976	3.8	2.599	-26.5
4.0	1.811	1.885	2.505	2.355	6.0	3.538	-41.2

(1) Theoretical Value

(2) Modified Analogy

(3) Direct Analogy

It can be seen that a considerable improvement is obtained when the modified analogy is applied. It must be noted, however, that this improvement is limited to the degree of correlation of the curves of density ratio for air and water depth ratio. Table 2.3 shows numerical values of correlation between the two ratios for some reference Froude and Mach numbers.

**Table 2.3 Difference in Theoretical Correlation of
Water Depth and Air Density Ratios**

M=F	$\frac{h_2}{h_1}$	$\frac{\rho_2}{\rho_1}$	% Differ.
2.0	1.443	1.458	1.03
2.2	1.471	1.492	1.41
2.4	1.503	1.530	1.76
2.6	1.538	1.570	2.04
2.8	1.574	1.611	2.30
3.0	1.612	1.655	2.60
3.2	1.651	1.700	2.90
3.4	1.690	1.744	3.10
3.6	1.730	1.791	3.41
3.8	1.770	1.838	3.70
4.0	1.811	1.885	3.92

Having established the nature of the modified analogy, an outline of the procedure for the determination of aerodynamic parameters is presented here:

The subscript "i" is conventionally used as the region preceding the change in flow conditions due to a shock or an expansion and "j" as the region after the discontinuity producing the change in flow conditions.

a) The depths h_i and h_j are determined experimentally. In this case, h_i can be the water depth of the undisturbed flow which can be obtained from Table 4.2.

b) After the corresponding water depths have been determined, the ratio h_j / h_i is calculated and assumed to be equivalent to the density ratio across

the discontinuity for the supersonic flow. Here is where the modification to the direct analogy takes place.

c) Now the corresponding pressure ratio can be calculated applying the aerodynamic relations. For conditions behind a shock wave, the Rankine-Hugoniot equation is applied:

$$\frac{p_j}{p_i} = \frac{6\left(\frac{\rho_j}{\rho_i}\right) - 1}{6 - \left(\frac{\rho_j}{\rho_i}\right)} \equiv \frac{6\left(\frac{h_j}{h_i}\right) - 1}{6 - \left(\frac{h_j}{h_i}\right)} \quad (2.5.1)$$

For conditions behind an expansion, the isentropic equation of state is used:

$$\left(\frac{p_j}{p_i}\right) = \left(\frac{\rho_j}{\rho_i}\right)^{1.4} = \left(\frac{h_j}{h_i}\right)^{1.4} \quad (2.5.2)$$

For surfaces whose flow conditions are affected by surfaces located upstream from them, ratio of local pressure to free stream is calculated considering the previous pressure ratios in the following fashion:

$$\frac{p_n}{p_\infty} = \frac{p_n}{p_{n-1}} \frac{p_{n-1}}{p_{n-2}} \dots \frac{p_1}{p_\infty} \quad (2.5.3)$$

With the pressure ratio, several aerodynamic parameters of interest can be obtained. The pressure coefficient is considered first and is defined as:

$$C_p \equiv \frac{p - p_\infty}{q_\infty} \quad (2.5.4)$$

where:

$$q_{\infty} = \frac{1}{2} \rho_{\infty} V_{\infty}^2 = \frac{\gamma}{2} p_{\infty} \left(\frac{p_{\infty}}{\gamma p_{\infty}} \right) V_{\infty}^2 \quad (2.5.5)$$

Using the definition of Mach Number, Eqn. (2.2.5) can be written as:

$$q_{\infty} = \frac{\gamma}{2} p_{\infty} M_{\infty}^2 \quad (2.5.6)$$

So finally the pressure coefficient becomes:

$$C_p = \frac{2}{\gamma M_{\infty}^2} \left(\frac{p}{p_{\infty}} - 1 \right) \quad (2.5.7)$$

The lift and drag coefficients, as well as the moment coefficient, are considered next. The lift, drag and moment are defined as:

$$\begin{aligned} L &= C_L q_{\infty} A \\ D &= C_D q_{\infty} A \\ M &= C_M q_{\infty} A(l) \end{aligned} \quad (2.5.8)$$

where:

C_i = coefficient

q_{∞} = dynamic pressure

l, A = reference length and area

Dividing both sides by $a_\infty^2 = \frac{\gamma p_\infty}{\rho_\infty}$ and solving for the coefficients, the following expressions are obtained:

$$\begin{aligned} C_L &= \frac{2L}{\gamma A M_\infty^2 p_\infty} \\ C_D &= \frac{2D}{\gamma A M_\infty^2 p_\infty} \\ C_M &= \frac{2M}{\gamma A I M_\infty^2 p_\infty} \end{aligned} \quad (2.5.9)$$

The forces on the body in question can be determined from the pressure distribution over the body. This, in general, requires the integration of the pressure over the surfaces, but for flat surfaces of smooth geometry, the pressure is constant over the surfaces and integration is not required.

The lift coefficient will be considered to illustrate this:

$$L = \sum p_k A_k \quad \text{where } k = \text{number of surfaces}$$

$$C_L = \frac{2}{\gamma M_\infty^2} \left[\frac{1}{p_\infty} \frac{\sum p_{\perp k} A_k}{\sum A_k} \right] \quad (2.5.10)$$

where $p_{\perp k}$ is the component of the pressure normal to the direction of the flow.

If the body is at an angle of attack α , then this angle has to be included in the calculation of the component.

The ratio $\frac{p_{\perp k}}{p_\infty}$ can be obtained from Eqn. (2.5.3) and the value of the ratio

for each surface is obtained as explained before. In like manner, the other coefficients can be derived.

Even though the coefficients derived above are the parameters of most concern, it is possible to obtain some more information about the flow by using what is already known:

d) Now that the pressure and density ratios are known, the corresponding temperature ratio can be calculated.

$$\frac{T_2}{T_1} = \left(\frac{p_2}{p_1} \right) \left(\frac{\rho_1}{\rho_2} \right) \quad (2.5.11)$$

e) Also the Mach Number behind the shock wave can be calculated by means of the corresponding equation:

$$M_2 = \sqrt{ \left(M_1^2 - \frac{2 \left(1 - \left(\frac{\rho_1}{\rho_2} \right)^2 \right)}{\left(\frac{\rho_1}{\rho_2} \right) (\gamma + 1) - (\gamma - 1)} \right) \left(\frac{p_1}{p_2} \cdot \frac{\rho_2}{\rho_1} \right) } \quad (2.5.12)$$

where:

$$\frac{\rho_1}{\rho_2} = \frac{h_1}{h_2}$$

III. Experimental Apparatus

In this chapter a description of the hydraulic simulator and its associated data processing system is given along with a description of the models used in the experiments.

3.1 Hydraulic Simulator

Only a general description of the simulator will be given here and emphasis will be placed on the modifications carried out on the system in order to make it operational. The interested reader can find a more detailed description in Ref 9.

The simulator is located in room 104 of building 255 at WPAFB in area B and is shown in Figure 3.2. The test area consists of a glass plate with mirror surface finish to ensure smoothness of the flow. The working section is limited to a triangular region bounded by the nozzle and two sides formed by inward-propagating wavelets generated by the two ends of the nozzle.

In order to obtain the desired test conditions, the slope of the glass can be adjusted from +1 degree (counterclockwise) to -5 degrees (clockwise) (See Fig. B.10), so that uniform flow can be obtained. The flow rate through the simulator is controlled by a gate valve installed downstream of a centrifugal motor pump. The velocity, in turn, is controlled by the total head in the feeding tank. The nozzle is adjusted to leave a 6.4 mm gap between the glass and the nozzle. This produces a water layer of approximately the same thickness which theoretically makes the celerity of the waves independent of λ , the wave length.

The test section does not have side walls which was found to result in variations of water depth as a function of head heights and also of accelerating flow in the downstream direction for angles of inclination less than that of uniform flow.

A collection tank located downstream from the glass plate is used to collect all the running water for recirculation. This tank is connected to the feeding tank through the pump thus completing the recirculation path. The motor pump is very well isolated so that no vibration is communicated to the simulator. Also, a filter is teed off from the outlet of the pump so that the water can be recirculated to remove impurities such as dust or debris. The feeding tank has four pieces of honeycomb to straighten the flow and suppress turbulence before the flow exits through the nozzle.

A traversing mechanism is installed on top of the test region. This mechanism is designed for mounting the escape capsule to simulate its separation from the primary model on the horizontal plane. Other equipment such as cameras can be attached to the traverse which displaces transversally by means of a micro stepping motor controlled by a programmable controller and a thumbwheel interphase.

3.2 Modifications on the Simulator

Several modifications had to be made to the simulator before it could be used for this set of experiments. On what follows a description of the modifications is given:

Installation of a graduated scale in the head tank

The head tank had two scales (graduated in millimeters), attached to the outside of the transparent sections of each lateral wall. It was found that these scales were unreliable because part of the scale was blocked by the frame of the tank and also because the meniscus effect on the wall of the tank made the reading difficult.

In order to solve this problem, a scale of the appropriate lengths graduated in millimeters was installed inside the tank far from the walls. The effect of the

meniscus was minimized by taking the readings with the camera from underneath the water surface. The scale is vertically adjustable and its zero reading can be aligned with the surface of the table by means of a cathetometer.

Installation of a camera to visualize the head height

As was mentioned above, the flow rate and hence the head height is controlled by the operator by means of the gate valve. This valve is located in such a position that it is not possible to visualize the head height readings on the scale when the valve is being manipulated. This situation made the adjustment of head height with a single operator extremely inefficient.

This problem was solved by installing a video camera aimed at the scale. The camera was connected to a TV monitor located besides the valve thus making the adjustments in head height very easy.

Installation of drain lines

It was found that the simulator was not capable of handling negative (counterclockwise) angles greater than approximately 0.5° because the water present in the troughs would reverse its direction and start flowing over from underneath the table.

This problem was solved by installing drain lines from the end of the trough closest to the feeding tank and directed to the collecting tank.

Installation of traverse bar to mount photographic equipment

In order to obtain images of the profile of the flow on the surfaces of the models while the capsule was moving, a transverse bar and the corresponding mounts for the photographic equipment were built and attached to the motor.

The bar would move along with the capsule, enabling the cameras to keep a constant focal length throughout the process.

3.3 Image Acquisition and Data Analysis System

This section contains a brief description of the equipment used to obtain and analyze the images for any particular case that needs to be investigated. A more detailed description can be found in Ref. 9 and the corresponding user's manual.

The process may be divided into three categories: Image acquisition, image processing and image data analysis.

For the image acquisition, photographic cameras are used. The surface displacement profile as well as the surface displacement pattern can be recorded both for static and dynamic cases. For the former, the cameras can be conveniently mounted on tripods, whereas for the latter the cameras are mounted on a specially designed bar which is attached to the traversing mechanism so that consistent photographic results can be ensured when the capsule is moving.

Illumination is provided by two 500-W lamps that are attached to the main frame. These lamps can be conveniently located to obtain the desired effect.

The system also has 5-watt argon-ion laser sheet generator which can be used to greatly enhance the wave profile if the flow is seeded with a florescent dye. This system, however, can at present be used only for very simple geometries such as for example, a wedge.

The image processing system consists of a 35 mm film scanner and a commercial software for optimizing images called "Photostyler". This software offers a variety of image processing algorithms such as image correction and enhancement, image transformation and composition, filtering, edge detection and contouring, etc.

The image data analysis consists of a software package called "IPPLUS" that has the capability of measuring the outline of any object in the image. It also measures distances between points or lines of different objects, areas, perimeters and angles.

Its basic unit of measure is the pixel, but provided there is a reference of known length in the image, any unit can be used.

Also, a data analysis software package called "Sigma Plot" can be used. This software package can statistically process data and display it in two and three dimensional graphics.

The host computer is an IBM AT-compatible PC (Gateway 2000) with an INTEL 80386 microprocessor and an 8037 coprocessor.

Even though not a part of the data acquisition and analysis system, the compumotor system for the traverse mechanism is programmed, controlled and operated via the computer and therefore a brief description is included here.

The controller is programmed from the EDITOR submenu and operated from the TERMINAL EMULATOR sub menu of the XWARE directory. The system is capable of producing very complex profiles by combining the acceleration, velocity and displacement commands with other high level functions. For a detailed description of this system, refer to the corresponding user's manual.

3.4 Models

The models consisted of a crew capsule and a fuselage of the forebody of a generic supersonic airplane and can be seen in Figs. 3.1(a) and 3.1(b). The shape of the models generally resembles that of the F-111, the only existing airplane with an ejectable crew capsule in the USAF inventory, but includes a number of simplified features.

The basic criterion on which the building of the model was based was the ability to easily utilize the shock-expansion theory to compare theoretical and experimental results. Therefore a complicated geometry was avoided with three specific purposes:

- a) Facilitate calculation of aerodynamic data using the theory.
- b) Ensure attached waves at all times in the compression zone.
- c) Avoid, whenever possible, flow separation due to sharp corners in the expansion zones.

As can be seen in section 4.1.2, the range of interest for the Mach Numbers was from 2.0 to 4.0, therefore it was for this range that the analysis was made. The compression zones were analyzed first and the model in water was initially considered. An analysis of Fig. 2.2 indicates that the water wave becomes detached for the combination $Fr = 2.0$ and $\theta = 19.57^\circ$, therefore any flow deflection angle smaller than this one will ensure an attached wave.

For the case of air, the maximum shock wave angle before detachment can be calculated from Eqn. (3.2.1):

$$\sin^2 \epsilon_m = \frac{1}{\gamma M_1^2} \left\{ \frac{\gamma+1}{4} M_1^2 - 1 + \left[(\gamma+1) \left(1 + \frac{\gamma-1}{2} M_1^2 + \frac{\gamma+1}{16} M_1^2 \right) \right]^{\frac{1}{2}} \right\} \quad (3.3.1)$$

Once this angle is known, the flow deflection angle that produces such an angle can be obtained via:

$$\cot \delta_{\max} = \left(\frac{\gamma+1}{2} \frac{M_1^2}{M_1^2 \sin^2 \epsilon_m - 1} - 1 \right) \tan \epsilon_m \quad (3.3.2)$$

Using a Mach Number value of 2.0 in this expression, it yields a maximum flow deflection angle that is higher than that for water ($\delta = 22.97^\circ$). This indicates

that it is the model in water that dictates the maximum flow deflection angle that can be used for the compression region in the simulation . It was decided to select values well below the detachment zone to account for possible errors in establishing the test conditions. With the above information at hand, angles of 15° and 12° for upper and lower surfaces of the compression zones of the capsule were chosen (surfaces 4 and 2 respectively). These angles are important for the expansion zones as well if they follow the compression regions because compression angles that are too large are going to impose large deflection angles in the expansion regions which could lead to flow separation. This is especially true if a simple geometry is desired for the model.

For the expansion region there is limited information that can be obtained from the theory because the latter does not take into account the viscous effects that produce the separation, so only a qualitative analysis is presented.

It can be shown that the maximum flow deflection angle is theoretically given by:

$$\pm v_{\max} = \frac{\pi}{2}(\sqrt{k} - 1) \quad (3.3.3)$$

where $k = \sqrt{\frac{\gamma+1}{\gamma-1}}$

For a gas with $\gamma = 1.4$, $v_{\max} = 130.45^\circ$ and for water ($\gamma = 2.0$), $v_{\max} = 65.9^\circ$, so angles well below that for water should be used. In the interest of keeping the shape of the model simple, the surfaces following the compression area were made parallel to each other and to the centerline of the fuselage. This implied that the turning angles were numerically equal to those of the compression region, i. e., 12° and 15°. For the region following these expansions, the surface was made at an angle of 35°. All of these angles were well below the theoretical value of maximum flow deflection before separation.

An early study [Ref 9], showed that Teflon possesses good hydrophobic properties and therefore produces a very small meniscus upon contact with water. Based on this, the models were made from Teflon and carefully machined to get the best possible surface finish. It is important to mention that due to defects in fabrication, the angles of the capsule were slightly different from the angles originally selected.

IV. Experimental Procedure

4.1 Calibration of the Hydraulic Simulator

4.1.1. Objective

The importance of the calibration of the hydraulic simulator cannot be overemphasized, since the accuracy is a matter of crucial importance in applying the analogy. Therefore, several weeks were spent in calibration tests of the simulator.

The objective of this part of the thesis was to obtain the best possible test conditions. For this, two aspects were given special consideration: the determination of Froude Number as a function of an easily controllable parameter, head height in this case, and also the verification of the necessary angles to get uniform velocity. This last requirement has been traditionally considered as the standard way to indirectly meet the assumption of zero shear along the bottom surface. In other words, when uniform velocity is established, the bottom surface shear equals the component of the gravity force and accelerations from this source can be disregarded.

It is pointed out here that no attempt was made to evaluate the bidimensionality of the flow within the working section since such condition had been established by Liu et al at an earlier stage [Ref. 9]

4.1.2 Froude Number versus Head Height

As was said previously, one of the main tasks was to get an accurate representation of the Froude Number. This dimensionless parameter relates inertia forces and gravity forces and is defined as:

$$F_r = \frac{V}{\sqrt{gL}} \quad (4.1.2.1)$$

where:

V= Velocity of the Flow

g= Acceleration of gravity

L= Length parameter

For this case and that of open channels, L is equal to h which is the depth of the water. So Eqn. (4.1.2.1) becomes:

$$F_r = \frac{V}{\sqrt{gh}} \quad (4.1.2.2)$$

Early runs suggested the convenience of expressing the Froude number as a function of head heights because they were a direct function of the gate valve controlled by the operator. This was concluded after discarding initial attempts to obtain the Froude number by means of the visual determination of the shock wave angles produced by a test wedge of known semi-angle δ (See Fig. 2.2) This was due to the difficulty in the accurate determination of the angles and also due to the low resolution that the method had.

Several measurements in the test area indicated a clear variation of the water depth as a function of head heights. The water depth variation for an ample spectrum of head heights was measured at two positions downstream from the nozzle along the centerline of the table: .1 m and .25 m. The results were best fitted using a polynomial fit in MATLAB and the plot is shown in Fig. 4.1. This allowed establishing an initial estimate of the flow velocity as a function of head height by means of the energy equation:

$$V = Cd\sqrt{2g(h_h - h_t)} \quad (4.1.2.3)$$

where:

V = Velocity of the Flow

g = Acceleration of Gravity

h_h = head height

h_s = water depth

C_d = Discharge Coefficient (initially estimated to be 0.93 [Ref. 9])

The plot for the velocities obtained using this expression is shown in Figure 4.2. Since the velocity and water depth were known at this point, it was possible to get an initial estimate of the Froude number as a function of head heights. From this it was determined that the range of head heights necessary to cover the values of Froude numbers needed for the test was between 20 and 80 mm.

It was considered necessary at this stage to confirm the validity of these results using other procedures. For this purpose, two different procedures were examined. As a first approach, different glass Pitot tubes were built and tested. After some experimentation, it was determined that a one millimeter diameter tube was suitable to perform these measurements. Even though the data obtained for locations 0.05 m downstream from the nozzle correlated well for the range of interest with that of Eqn. (4.1.2.2), as shown in Fig. B.2, they were discarded because of the error associated with the capillary effects. (See Appendix C). The second approach was to determine the velocity of a float between two points in the flow using a high speed camera (See Fig. B.9). Several trials indicated that the best measuring conditions in terms of repeatability and resolution were obtained using a camera speed of 1,000 frames per second, the points separated 0.05 m and the test location at 0.1 m downstream from the nozzle. The values of velocity obtained by this procedure were plotted and compared with the values from Equation (4.1.2.2). The results of the two methods correlated very well. (See Fig. 4.2).

With the information available at this stage, it was possible to re-estimate the value of the discharge coefficient in the following fashion:

From the energy equation (Eqn. (4.1.2.3)):

$$V = Cd\sqrt{2g(h_h - h_s)}$$

the discharge coefficient is solved for as shown:

$$Cd = \left[\frac{V^2}{2g(h_h - h_s)} \right]^{1/2} \quad (4.1.2.4)$$

Where V and h_s are experimentally measured values. The following table shows the calculated value of discharge coefficient for the reference head height:

Table 4.1
Value of Discharge Coefficients for Reference Heights

Head Height (mm)	Discharge Coefficient Cd
20	0.836
40	0.909
50	0.911
60	0.907
80	0.922
AVERAGE VALUE OF Cd:	0.91255±0.0067

It can be seen, upon calculation of the average, that the value of Cd for a head height of 20 mm has been discarded. For this Chauvenet's criterion was used [Ref. 8]. The reason for discarding this value lies not only on the fact that a large discrepancy exists in Cd , but also on the fact that a larger uncertainty was present

for all the experimentally calculated parameters in this region. For this reason in all subsequent analysis an uncertainty of two standard deviations was assigned to this value of head height.

At this point, it was possible to get an expression of the Froude number as a function of head height independent from Eqn. (4.1.2.2). It is relevant to point out here that these values were obtained for zero angle of inclination of the table.

Numerical values of Froude number versus head height obtained from the energy equation and the fitted expression for head height, are presented in Table 4.2 whereas the plot of these data is shown in Fig 4.3.

Table 4.2
Values of Head Height versus
Water Depth, Velocity and Froude #

h (mm)	hs (mm)	Vel (m/s)	Fr #
8.0000	7.8602	0.0478	0.1721
10.0000	7.8326	0.1880	0.6786
12.0000	7.8058	0.2616	0.9457
14.0000	7.7798	0.3185	1.1536
16.0000	7.7546	0.3667	1.3303
18.0000	7.7302	0.4093	1.4870
20.0000	7.7066	0.4478	1.6294
22.0000	7.6838	0.4832	1.7610
24.0000	7.6618	0.5162	1.8839
26.0000	7.6406	0.5472	1.9998
28.0000	7.6202	0.5766	2.1098
30.0000	7.6006	0.6044	2.2147
32.0000	7.5818	0.6311	2.3153
34.0000	7.5638	0.6567	2.4119
36.0000	7.5466	0.6813	2.5051
38.0000	7.5302	0.7050	2.5951
40.0000	7.5146	0.7279	2.6824
42.0000	7.4998	0.7502	2.7670
44.0000	7.4858	0.7717	2.8493
46.0000	7.4726	0.7927	2.9294
48.0000	7.4602	0.8132	3.0074
50.0000	7.4486	0.8331	3.0835

Table 4.2
Values of Head Height versus
Water Depth, Velocity and Froude #

h (mm)	hs (mm)	Vel (m/s)	Fr #
52.0000	7.4378	0.8526	3.1578
54.0000	7.4278	0.8716	3.2304
56.0000	7.4186	0.8902	3.3014
58.0000	7.4102	0.9084	3.3709
60.0000	7.4026	0.9262	3.4389
62.0000	7.3958	0.9437	3.5055
64.0000	7.3898	0.9609	3.5708
66.0000	7.3846	0.9778	3.6347
68.0000	7.3802	0.9944	3.6974
70.0000	7.3766	1.0107	3.7590
72.0000	7.3738	1.0267	3.8193
74.0000	7.3718	1.0425	3.8786
76.0000	7.3706	1.0580	3.9367
78.0000	7.3702	1.0733	3.9938
80.0000	7.3706	1.0884	4.0498
82.0000	7.3718	1.1033	4.1048
84.0000	7.3738	1.1180	4.1588
86.0000	7.3766	1.1324	4.2119
88.0000	7.3802	1.1467	4.2640
90.0000	7.3846	1.1608	4.3151
92.0000	7.3898	1.1748	4.3654
94.0000	7.3958	1.1885	4.4147
96.0000	7.4026	1.2021	4.4632
98.0000	7.4102	1.2156	4.5108
100.000	7.4186	1.2289	4.5575

4.1.3 Uniform Flow

Several attempts were made to obtain an analytic expression of the angle of inclination of the table needed for uniform flow.

The initial attempt was to make use of Manning's formula, extensively utilized to determine uniform flow in channels:

$$V(m/s) = \frac{R_h^{3/2}}{n} S_o^{1/2} \quad (4.1.3.1)$$

where:

V= Velocity

n= Coefficient of surface roughness

R_h = Hydraulic Radius defined as the ratio of the wetted perimeter
and the cross sectional area of the flow.

S_o = Slope of the surface defined as the sine of the inclination of the
surface. For small angles (< 5.7degrees) this expression can be
approximated as the angle, i.e., $\sin\phi \approx \phi$

Comparing the results obtained using this equation with those experimentally determined, a large divergence was found. Different assumed cross sections (rectangular and elliptic), were used to estimate the hydraulic radius, but the discrepancy remained unaltered. It was concluded that Manning's equation was not applicable in this case due to the absence of side walls in the simulator.

An alternate approach consisted of modeling the flow as a slug of fluid acted upon by forces due to surface shear stress and gravity alone and moving on an infinitely wide plate.

This assumption made the fluid independent of its longitudinal position on the plate and for this case the following expression was derived:

$$\phi = \sin^{-1} \left[\frac{4}{3} \text{Re}_{h_s}^{-1} Cd^2 \frac{(h_h - h_s)}{h_s} \right] \quad (4.1.3.2)$$

where: $\text{Re}_{h_s} = \frac{Vh_s}{\nu}$ Reynolds Number based on the water depth

Cd = discharge coefficient 0.91

h_s = water depth

h_h = head height

A large discrepancy (approximately 1°), was found between experimental and theoretical values using this expression. It was finally concluded that for the control volume analyzed, the presence of transversal components of the flow due to the water flowing off the plate, invalidated the assumption of mass conservation in the longitudinal direction causing this discrepancy.

At this point, it was decided to make direct use of the experimental values assigning a bigger value of error in areas where uncertainty was present. The experimental method used to get velocity variations consisted of measuring velocities using the high speed camera at one location downstream from the nozzle and compare it to the velocity at the nozzle. Initially a point 1.0 m downstream from the nozzle was selected, but the appearance of turbulent spots merging to form a moderately turbulent flow in this region made the experimentally obtained values of velocity very unreliable.

Considerable effort was made to minimize this turbulence which seemed to be triggered by small disturbances originating at the nozzle. For this purpose the distilled water was changed for the possibility of contamination by dirt or impurities, the head and collection tank as well as the surface of the table were thoroughly cleaned and the nozzle was dismounted, carefully checked for irregularities and cleaned before being reinstalled.

Since all of this produced only a marginal improvement, a new location was selected. A visual inspection indicated that the area around 0.5m was essentially free of turbulence. A calculation of the transition Reynolds number for incompressible flow along a smooth flat plate, indicated that for a position 0.45m downstream of the nozzle and for the range of velocities and temperatures used, the flow stayed below the value of 500,000 normally considered to be transition value from laminar to turbulent flow [Ref. 5]. (For the maximum velocity of 1.101 m/s, a temperature of 20° C at 0.45 m downstream, the Reynolds number was approximately 493,000).

Therefore, the location 0.45m downstream from the nozzle was selected. The measurements were made for five angles (from 0 to 2 degrees in increments of 0.5) for each one of the five basic head heights of 20, 40, 50, 60 and 80mm.

The velocity variation was determined for each angle of inclination of the table between zero and two degrees in increments of one half of a degree and then plotted and best-fitted using MATLAB (see Appendix C). The intersection of each fitted curve with the abscissa yielded the value of zero velocity variation as shown in Figs. B.3 to B.7 and so the value of uniform flow for the particular head height under consideration was determined (See Figs B.8(a) and B.8(b). Each value of zero velocity variation was plotted and best-fitted against head height. The corresponding plot is shown in Figure 4.4.

The experimental data showed a general linear trend so in the absence of an analytical expression against which to compare these data, a linear fit was chosen. This was in agreement with the trend shown by the analytical expressions derived above. It is important to mention that a quadratic fit would yield a curve passing closer to every point but for low values of head height, it predicted an inflection point for intermediate values of head height in order to get uniform flow, a result against common sense.

It is also important to mention that the rather large values of uncertainty for higher values of head height, were due to the way in which the uncertainty in the displacement for the determination of the error in velocity is established. This uncertainty is given by: $w_{\Delta} = \delta t v$ which indicates that the error grows when the velocity grows (For a more clear explanation of this, refer to Appendix C).

It is important to point out here that upon observation of Tables 5.B and 6.B in Appendix C, the velocity at station 0.45 was *consistently* greater than that of the nozzle and therefore the angles needed for uniform velocity were actually negative, i.e. the water must flow "uphill" (See Fig. B.10). It was concluded that since the simulator does not have lateral walls, the flow undergoes an expansion upon leaving the nozzle.

4.1.4 Error in the Data

During the calibration, great care was exercised to get rid of every possible source of error. It is, however, well known that error is inherently present in every experimental work and therefore a quantitative analysis of the error is given here.

An statistical analysis of the collected data was done largely based on Ref. 8. For each set of data an arithmetic mean was obtained. Since the data gathered for each condition was less than 20 measurements, a recommended relation for the sample standard deviation was used [Ref. 8]:

$$\sigma = \left[\frac{\sum_{i=1}^n (x_i - x_m)^2}{n-1} \right]^{1/2} \quad (4.1.4.1)$$

The only difference with the population expression for the standard deviation is the $n-1$ factor in the denominator of the square root, which makes the best estimate for the standard deviation slightly larger.

In some cases Chauvenet's criterion for rejection of dubious data points was used [Ref. 8]. For the determination of the uncertainty in the results, the expression derived by Kline and McClintock [Ref. 8] was used. It is important to remember that this expression is valid if the result is a function of independent variables and the uncertainties in the independent variables are all given with the same odds. In this case, the uncertainty is given by:

$$W_R = \left[\left(\frac{\partial R}{\partial x_1} W_1 \right)^2 + \left(\frac{\partial R}{\partial x_2} W_2 \right)^2 + \dots + \left(\frac{\partial R}{\partial x_n} W_n \right)^2 \right]^{1/2} \quad (4.1.4.2)$$

4.1.4.1 Water Depth

In order to obtain more consistent results, the depth was calculated from the arithmetic mean of the maximum and minimum depths where the maximum depth was measured at the instant when the tip of the measuring probe first touched the water surface and the minimum depth was measured when the tip constantly touched the water surface. The plot of water depth as a function of head height is shown in Figure 4.1. The error bars were considered to be one value of the sample standard deviation.

4.1.4.2 Head Height

Readability of an instrument is defined as "the closeness with which its scale can be read" [Ref. 8]. For the graduated scale inside the head tank, a readability of 0.5 mm is assumed based on a spacing of graduation of 1mm. This produces an uncertainty well within the uncertainty of the points.

4.1.4.3 Flow Velocity

The criteria for considering a measurement valid were the following:

- a) Each measurement was taken only three times if it was exactly repeatable.
- b) Each measurement was taken five times if it was not exactly repeatable.
- c) Where these criteria were not met, several measurements were taken (only case was head height of 20mm).
- d) Chauvenet's criteria to eliminate dubious data points was used.

The values of velocity for each head height were averaged and the sample standard deviation in each case was obtained. Also the uncertainty was determined by the method mentioned above.

For the uncertainty in the velocity differential between points located at 0.1 m and 0.45 m downstream from the nozzle, the procedure consisted of projecting the uncertainty at zero degree angle inclination of the table over to the abscissa about the point of intersection of the curve with the abscissa (See Fig. B.8.a))

For the cases of a head height of 20 and 40 mm, the uncertainty on the abscissa was the difference of the intersection points for a quadratic and linear fit (See Fig. B8.b)). To illustrate this, use is made of the following numbers for 20 mm:

Intersection of linear fit with abscissa occurs at -0.55° . Intersection of quadratic fit with abscissa occurs at -0.34° , (the minus sign indicating counterclockwise rotations) so the angular value for uniform velocity at 20 mm is $0.55 \pm 0.21^\circ$.

4.1.4.4 Froude Number

As was pointed out above, the Froude Number is determined as the ratio of the flow velocity and the square root of the product of the gravity and the water depth. Since both numerator and denominator were experimentally calculated, there is error associated to them and therefore the expression for the Froude Number also contains an amount of error which needs to be calculated.

The expression for the Froude Number as a function of head height when the error is included is given by:

$$F_r = \frac{V(1 \pm \epsilon_v)}{\sqrt{gh(1 \pm \epsilon_h)}} \quad (4.1.4.4.1)$$

where: $\epsilon_v = \frac{w_v}{V}$ and $\epsilon_h = \frac{\sigma_h}{h}$

and V = Velocity of the flow (m/s)
 w_v = Error in Velocity
 σ_h = Sample Standard Deviation
 h = Water Depth (mm)

Assuming small errors, this expression can be written as:

$$F_r = \frac{V}{\sqrt{gh}} \left[1 \pm \left(\epsilon_v + \frac{1}{2} \epsilon_h \right) \right] \quad (4.1.4.4.2)$$

Table 4.3 shows the associated error for the reference head heights. The plot for the Froude number as a function of head height is shown in Fig. 4.3.

Table 4.3 Associated Error in Froude Number

Head Height (mm)	Velocity (m/s)	Water Depth (mm)	Froude Number	Error in %
20	0.414	7.687	1.647	5.40
40	0.727	7.487	2.701	1.86
60	0.922	7.360	3.452	3.53
80	1.101	7.258	4.051	2.96

4.1.5 Sensitivity of Aerodynamic Parameters

Now that the error band has been established for the Froude Number, the effect that a Froude number slightly off the correct value has on the aerodynamic parameters can be analyzed. From Eqs (2.4.3) and (2.4.4), it can be seen that a +5% variation in the values of some reference Froude numbers produce the following variations in the water depth ratio:

Table 4.4 Effect of a 5% Variation in the Froude Number on the Height Ratio

Flow Deflec. Angle	Froude Number	$\frac{h_i}{h_j}$ Depth Ratio	$\frac{h_i}{h_j}$ with 5% variation	$\Delta\%$ Between the Ratios
16.6	2	1.800	1.810	-0.6
16.6	2.25	1.839	1.866	-1.5
16.6	2.5	1.903	1.939	-1.9
16.6	2.75	1.976	2.019	-2.2
16.6	3.0	2.055	2.104	-2.4
16.6	3.25	2.138	2.196	-2.7
16.6	3.5	2.223	2.283	-2.7
16.6	3.75	2.309	2.375	-2.9
16.6	4.0	2.398	2.469	-3.0

As was seen in Section 2.5, the modified analogy consists of equating the water depth ratio to the density ratio so, if this water depth ratio has an associated error, it is going to affect the numerical values of the aerodynamic parameters. From the table above it can be inferred that the water depth ratio is not very sensitive to errors in the Froude Number, but this sensitivity grows for increasing values of the latter.

On a strict aerodynamic sense now, it will be seen how a small variation in the density ratio affects the value of pressure ratio and pressure coefficient across a shock.

The density ratio is propagated from a Mach number of 2.0 to a value of 4.0 via the following equation:

$$\frac{\rho_j}{\rho_i} = \frac{(\gamma+1)M_1^2}{2+(\gamma-1)M_1^2} \quad (4.1.5.1)$$

A +5% variation to the value of the density ratio is added and the numerical values are evaluated in the Rankine Hugoniot equation and in the expression of the pressure coefficient:

$$\frac{p_j}{p_i} = \frac{\left[6\left(\frac{\rho_j}{\rho_i}\right)-1\right]}{\left[6-\left(\frac{\rho_j}{\rho_i}\right)\right]} \quad (4.1.5.2)$$

$$Cp = \frac{2}{\gamma M^2} \left(\frac{p_j}{p_i} - 1 \right) \quad (4.1.5.3)$$

Again some reference values are given in Table 4.5 below.

**Table 4.5 Variation of Aerodynamic Parameters with a 5% Variation
in the Density Ratio**

Mach number	$\frac{p_j}{p_i}$	$\frac{p_j}{p_i}^*$	C_p	$C_{p_v}^*$
2.0	4.500	4.938	1.250	1.406
2.25	5.740	6.366	1.337	1.514
2.5	7.125	8.000	1.400	1.600
2.75	8.721	9.934	1.448	1.676
3.0	10.333	11.949	1.482	1.738
3.25	12.156	14.301	1.509	1.799
3.5	14.125	16.935	1.531	1.858
3.75	16.240	19.879	1.548	1.918
4.0	18.500	23.167	1.563	1.979

* Values with a 5% variation in density ratio

It is clear from this table and Figs. 4.5 and 4.6, that the pressure ratio and the pressure coefficient are quite sensitive to variations in the density ratio and that therefore they are quite sensitive to variations in the water depth ratio. Notice that this analysis is valid only for compression zones that are preceded by undisturbed flow.

For the case of expansion regions, the equation relating pressure ratio to density ratio is given by Eqn. (2.5.2), renumbered here for convenience:

$$\frac{p_j}{p_i} = \left(\frac{\rho_j}{\rho_i} \right)^{1.4} \quad (4.1.5.4)$$

It can be seen, upon analysis of this expression, that the variation in the pressure ratio only depends on the error present in the density ratio and therefore is the same for any value of the latter. So for example a 5% deviation from the true value of density ratio, will produce a 7% variation in the pressure ratio, whereas a 10% deviation in the former produces a 14.3% error in the pressure ratio.

For the case of the pressure coefficient, the effect of the pressure ratio in preceding regions has to be taken into account so if these values are in error, the value of C_p will deviate from the theoretical value.

4.2 Description of the Experimental Procedure

This section contains a description of the procedure followed to obtain the experimental data from the models. It is divided in three parts: the description of the image acquisition procedure used for the capsule alone, the description of the same procedure used for the capsule/fuselage system and the explanation of the procedure for processing and analyzing the images.

It is important to indicate here that the purpose of running the experiments for the capsule itself was to determine, with a simple case, the degree of accuracy that was to be expected for the more complex case of the capsule interacting with the fuselage.

4.2.1 Capsule

For the capsule, it was decided to run two cases within the range of interest. The cases are shown in Table 4.6:

Table 4.6 Experimental Runs for Capsule

M=F	Angle of Attack of Capsule α Degrees	Inclination of Table θ Degrees
3.10	0°	0.81
3.77	0°	1.08

On every lateral surface of the capsule, a one-centimeter-wide tape of graph paper was glued along the upper end and through the total length as can be seen in the pictures on pages A.40 and A.41. This tape was used as a longitudinal positional reference and more importantly to provide an easy dimensional reference needed for the software package used to determine the wave profile.

After placing the model inside the test area and setting the desired conditions of flow velocity and angle of inclination, images of the wave profile on each lateral surface were obtained. At this stage, care had to be exercised to get the best possible contrast of the wave on the surface. This was done by making adjustments to the light conditions with the use of additional lamps.

4.2.2 Capsule and fuselage

For this condition, it was decided to run several different cases all of which are summarized in Table 4.7 below.

Table 4.7 Cases Studied for Capsule/Fuselage System

Froude Number	Type of Motion	Position of Capsule wrt Fuselage	Velocity of Displacement of Capsule
3.08	Static	0.25 L	N.A.
		0.75 L	
	Dynamic	0.25 L	0.1 Fr 0.2 Fr
		0.75 L	0.1 Fr 0.2 Fr

In this set of experiments, emphasis was placed on the determination of the differences of the flow behavior for the static and dynamic cases. Also the effect of proximity and velocity of "vertical" displacement of the capsule with respect to the fuselage were investigated.

The procedure for the acquisition of the images was the same as that of the capsule, but for the dynamic case the cameras were mounted on the transverse beam mentioned in Section 3.1 and remotely operated. The cameras moved with the model and the images of the wave profile on the shock surfaces were obtained. The selection criteria of the test conditions were established for this case as follows:

a) Proximity:

The parameter used here was the capsule "cord length" $L=18.9\text{cm}$, and the position was referred to as fractions of L . Several trials indicated that, for the range of velocities used, it was not possible to place the capsule at zero angle of attack inside the "shock wave" produced by the fuselage because the flow would not remain attached or else would show the characteristic unsteady undular behavior of flow near critical condition.

In order to solve this problem, it was decided to place the capsule inside the shock wave of the fuselage at an angle with respect to the fuselage. This angle was chosen to be such that the capsule would meet the incoming flow at zero angle of attack. This angle was equal to that of the front deflecting surface of the fuselage, i.e., 11.5 degrees (See Fig. 3.1)

An analysis of this configuration using the hydraulic equations to calculate the parameters before and after a hydraulic jump, shows the following conditions (See Figs. 2.2 and 5.25):

Initial Froude Number:	3.08
Flow Deflection Angle:	11.5 degrees
"Shock Wave" Angle:	29.76 degrees
Froude Number after Initial Shock:	2.152
Water Height Ratio (Across Jump):	1.733

These are now the initial conditions for the capsule. Doing a similar analysis it is possible to see that the conditions after the shock wave produced by the capsule are:

Table 4.8 Conditions After the Shock Wave Produced by the Capsule

Surface 2	Surface 4
Fr= 1.25	Fr=1.52
$h_3/h_2 = 1.819$	$h_4/h_2 = 1.525$
$\beta_{23} = 48.1^\circ$	$\beta_{24} = 40.15^\circ$

Notice that this is a simplified analysis since no consideration is given to the effect of the fuselage that, for this region, is characterized by the expansion produced by the cavity.

In spite of the rather low values of the Froude Numbers predicted by the theory, the flow remained fairly stable on both surfaces indicating probably that the velocities were higher than what this analysis predicted due to the presence of the expansion.

Another factor that had to be taken into account was the fact that enough separation was needed between capsule and fuselage to provide visual access for the camera.

With these factors considered, the first position was selected to be at 25% of L, i.e. 4.72cm. This distance was measured from the tip of the capsule to the initial point of the cavity.

The second position was selected such that the effect of the fuselage on the flow around the capsule was essentially different from that of the first position. This was to facilitate the determination of the differences between the two cases. The second position was chosen to be 75% of L, i.e., 14.7cm.

b) Velocity of Displacement

The two displacement velocities selected for the capsule were tied to the incoming free stream Froude number. Limitations in the velocity that the

Compumotor System could attain, constrained the displacements of the capsule to two velocities. Several trials were made and velocities of 10% and 20% of the incoming Froude number were chosen. This corresponded to 0.083 m/s and 0.167 m/s respectively. It is important to mention that the codes were so written as to ensure that the acceleration of the capsule from zero to the chosen velocity took place before it reached the selected position, so that at these points the capsule was moving with constant velocity.

4.2.3 Processing and Dimensioning of the Images

Inasmuch as a more or less complete explanation of the procedure is given in Ref. 9, only a brief description of the image processing and analysis will be given here. Emphasis will be placed on those areas where special care must be exercised to ensure that the data being obtained is accurate.

The process is the following:

a) **Digitization of Images:** Is performed by a 35mm scanner which can be brought up via Photo Styler on the PC. Several iterations can be made to optimize the image. The final image is displayed within Photo Styler.

b) **Processing of the Image:** Once in Photo Styler, several changes can be made to the image to get the desired result which is a well delineated wave profile. Among the most important functions are Brightness and Contrast, Edge Enhancement, Sharpen Filters, Smoothing Filters and Trace Contour. For a detailed description of each function, refer to the user's manual. Once the image is ready, it can be saved in the Tiff format (*.TIF)

c) **Image Dimensioning:** This is by far the most important part of the whole process because the measurements to get the wave profile are made here. Calibration is essential for proper interpretation of the data. The procedure for dimensioning the image is described in step by step fashion in the

corresponding user's manual, but in order to improve the results, the following aspects must be borne in mind: The reference dimension should be selected from areas in the picture that have the best possible resolution and that are free of distortion and use should be made of the "aspect ratio" function to establish the ratio between the vertical and horizontal directions in the image. This was important for this set of experiments since the reference was more easily measured horizontally whereas all the measurements were done vertically.

At this stage, it is possible to start the measurements. Before measuring the wave profile on a photograph, a known 1 cm. dimension on the model was measured on the photograph, as a check of the goodness of the calibration. The standard procedure used here for the experiments was to use the LINE function from the MEASUREMENTS sub menu of IPPLUS to trace two lines over the graph paper attached to the model that were a known distance apart. Then the function THICKNESS was used to determine the actual separation on the photograph for comparison to the known distance dimension on the model. Any difference between these values provided a correction factor for the measurements of the wave profile.

For the actual determination of the numerical values of the wave profile, the following method was used (See Fig. 4.8):

The wave profile was automatically traced using the AUTO TRACE function inside the MEASUREMENTS sub menu. The reference line, which was at a known distance from the surface of the table was traced using the LINE function. The THICKNESS function was used to get an average of the distance between the wave profile and reference line. Several measurements were made at discrete points from the reference line to the wave profile. These data were saved for further analysis.

An average of the data at these discrete points was obtained in order to determine the corresponding standard deviation. This average was compared to that obtained using the THICKNESS function as a means of checking the quality of the data. With this information available, it was possible to perform the calculations described in section 2.5 to get the desired data. It is important to mention that the THICKNESS function only provided the average value of the coordinates of the wave profile and no other statistical quantity.

V. Results And Discussion

This chapter is divided into two sections. The first section presents the results and the analysis for the crew capsule alone. The second section contains the results along with the analysis of the crew capsule and fuselage in their different configurations.

5.1 Crew Capsule

As was pointed out in Chapter IV, the objective of this particular set of experimental runs with the crew capsule was to determine the degree of agreement between the theoretical and experimental values for a case which would easily lend itself for a simple comparative analysis. It was thereby sought to establish the degree of accuracy that was to be expected in the modeling of the more complex case of ejection.

5.1.1 Theoretical Values

For the two cases under consideration, use was made of the shock-expansion theory to determine the ratios of the parameters of interest. This was done using the equations of the 2-D shock-expansion theory to compute the flow parameters before and after the shock, in conjunction with tables C.13, C.12 and C.6 of Ref. 6.

**Table 5.1 Theoretical Values of Ratio of Different Flow Parameters
Across a Compression Shock Wave**

Cases	Surfaces	M_∞	δ	$\frac{\rho_i}{\rho_\infty}$	$\frac{p_i}{p_\infty}$
1 ($M=F=3.1$)	2	3.08	16.6	2.1905	3.1877
	4	3.08	11.2	1.7761	2.2667
2 ($M=F=3.77$)	2	3.77	16.6	2.458	3.880
	4	3.77	11.2	1.943	2.627

**Table 5.2 Theoretical Values of the Ratio of Different Flow Parameters
Across an Expansion Wave**

Cases	Surface	M_i *	ν	M_j *	$\frac{p_j}{p_i}$
1 ($M=F=3.1$)	3	2.235	17.05	2.996	0.039
	5	2.517	11.5	3.066	0.4327
2 ($M=F=3.7$)	3	2.674	17.05	3.60	0.255
	5	3.031	11.5	3.70	0.385

* M_i = Mach number before the expansion
 M_j = Mach number after the expansion

5.1.2 Experimental Results

For this analysis, Tables 5.8 through 5.14 were used in conjunction with Figs. 5.1 through 5.16. For each one of the two cases, depth ratio, pressure ratio and pressure coefficient are presented for surfaces 2, 3, 4 and 5. For each plot a theoretical value based on the 2-D shock-expansion theory is presented as a solid line. Also the dashed line represents the average of the values of pressure and the dash-dotted lines represent the error band obtained from the standard deviation of the data. It is important to mention that these values were obtained operating the

average and the corresponding standard deviation of the water depth (density) ratio through the Rankine-Hugoniot equation and therefore not all the error "semi-bands" are of equal width.

It is important to point out that surface 6 is not presented because of the large discrepancy between theoretical and experimental values due to flow separation occurring at the sharp edge between surface 5 and 6. This separation was easily observable and was characterized by the flow following a trajectory more or less parallel to surface 5 and merging with the rest of the flow well downstream from the point of separation and also by a region of very low flow velocity in the zone adjacent to surface 6.

The compression surfaces were characterized by hydraulic jumps whose surface profiles were regular in shape, with practically no oscillation present. On each surface, an overshoot with respect to the theoretical value of the water depth occurred. This overshoot took place because the model not only decelerated the flow in the longitudinal direction, but also imparted an upward acceleration to it. In this case the restoring force is gravity and the damping is provided by the shear force of the surface. The interaction of the three forces produce variations in the profile of the jump until equilibrium is reached. The shape of the profile is Froude number dependent. In this case, the overshoot observed was larger for larger velocities and also its peak moved downstream on the surface as the velocity of the flow, and consequently its Froude number, increased. It is relevant to mention that it was not possible to observe an equilibrium region of water depth downstream from the jump, indicating that the surfaces were highly dominated by the transition portion of the hydraulic jump. It could also be seen that for the first case the overshoot began to decrease while still on the surface of the model, whereas for the second case the decrease seemed to occur only due to the presence of the

expansion. It is also interesting to observe that for bigger angles, the overshoot was correspondingly bigger.

Upon application of the modified analogy it can be seen that an average 93% agreement between theoretical values of density ratio and experimental values of water depth ratio was obtained, very close to the maximum possible theoretical agreement according to Fig. 2.3 (See analysis in Section 2.5). For this, the arithmetic average of the experimental values was considered. In one case only (surface 2 ($\delta=16.6^\circ$) for the second case), the average of water depth was larger than the theoretical value using the shock-expansion theory indicating, probably, a dependency of the vertical acceleration component on the value of the angle. It is relevant to mention here that the effect of the boundary layer on the model is to effectively thicken the profile making the flow deflection angle slightly larger and therefore the water height ratio bigger. This has then the effect of bringing the experimental values to a closer agreement with the shock expansion theory. This effect however is marginal and still what largely makes this ratio bigger than that predicted by the hydraulic theory, is the presence of vertical accelerations. The fact that the overshoot occurred at large values of longitudinal positions on the compression surfaces is a first indication that the size of the model should be larger.

In the expansion zones, there is a clearly observable region of transition where the flow gradually decreases its height until equilibrium is reached. This rather large transition increases the average of water depth and as a consequence a poorer agreement between theory and experiment is obtained. If an average is taken of the values where an approximate water depth equilibrium has been reached, a much better agreement is obtained. A criterion to determine where equilibrium has been reached after the expansion is not readily available and this is

another reason to consider a model of bigger dimensions. With a larger model, the undesirable effects of transition occur in a much smaller portion of the corresponding surface of the model and consequently equilibrium is reached over a larger portion of the model.

An estimate of the proper dimensions of the model can be obtained if the length of the jump can be computed. This is based on the assumption that the equilibrium condition for the water depth is reached immediately after the jump. Even though no firm analytical basis exists for the determination of the length of the jump [Ref. 11], some empirical equations have been developed for channels. One that looks particularly suitable is given by Ivanchenko [Ref. 4]:

$$L = 10.6(d_2 - d_1)\lambda^{-0.185}$$

where:

d_1 = Initial Depth (Before Jump)

d_2 = Final Depth (After Jump)

λ = Kinetic Flow Factor

The kinetic factor as defined by Bakhmeteff [Ref. 4], is twice the ratio of the kinetic energy head to the potential energy head contained in each pound of liquid flowing at depth d . This is equivalent to the Froude number raised to the second power.

It must be noted that this is only an estimate and that a set of experimental runs are needed to check the validity of these analytical results.

As was noted in section 4.1.5, the pressure ratio as well as the pressure coefficient are sensitive to errors in the density ratio so in applying the modified analogy, the error in the water depth ratio is carried over to the pressure ratio and pressure coefficient. This is more noticeable in the expansion regions where the effect of the pressure ratio of the preceding region as well as the high values of

density ratio for the calculation of the pressure coefficient is to produce values of C_p that are actually positive.

5.2 Capsule and Fuselage

For this analysis use is made of Tables 5.15 through 5.21 in conjunction with Figs. 5.17 through 5.24. It is important to mention that, based on the rather poor correlation obtained for the capsule alone on the expansion surfaces, only the compression regions of the capsule are analyzed for this case.

An analysis of the water depth ratio on surfaces 2 and 4 for the static and dynamic cases, reveals that there is a clear variation in the distribution of this parameter when the capsule is moving. This variation is characterized differently for the two surfaces: While for surface 4 (the one facing the fuselage), there is a drop in the water depth ratio for the dynamic conditions, on surface 2 there is an increase in the same parameter. This behavior was the same for position 1 and position 2, the only difference being the numerical values. It was also possible to observe that a small difference in water depth ratio existed between the two dynamic cases considered.

The differences in water depth ratio for the static and dynamic cases can be explained by the change in the angle of attack due to the motion of the capsule. In fact, the main effect of the "vertical" displacement of the capsule is to modify the angle at which the flow encounters the capsule. This change produces a higher effective flow deflection angle on surface 2 and a lower angle on surface 4. This accounts for the rise and drop in water depth ratio for surface 2 and 4 respectively.

A quantitative analysis of density and pressure distribution on the compression surfaces is possible if the following simplifying assumptions are made:

- a) The only effect of the fuselage on the flow around the capsule is

to decrease its velocity across the "shock wave" originating at the tip (See Fig. 5.25), and to deflect it an angle equal to that of the fuselage so that the angle of attack of the capsule is zero degrees inside the shock produced by the fuselage.

b) Since the effect of any expansion wave on the flow is to produce a small depression as the flow goes through a certain small angle of deflection. the interaction of a hydraulic jump and an expansion is to cause large total disturbances of the water surface. These disturbances, however, were not present on the compression surface 4 as can be seen in the corresponding pictures (See pictures on page A.40 and A.41), and therefore it was assumed that the expansion mainly reflected from the jump front and did not affect the water depth distribution on that surface. Using the hydraulic theory and the 2-D shock expansion theory, the following results are obtained:

Table 5.3 Theoretical Results of
Hydraulic Parameters

F Before H. J.	θ	Water Depth Ratio	F After H. J.	Pressure Ratio (En. 2.5.1)
3.08	11.5	1.733	2.14	2.202
2.11	16.6	1.820	1.24	2.373
2.11	11.2	1.520	1.52	1.813

**Table 5. 4 Theoretical Results Using
Shock-Expansion Theory**

M Before Shock	δ	Density Ratio	M After the Shock	Pressure Ratio
3.08	11.5	1.792	2.50	2.317
2.50	16.6	1.972	1.80	2.681
2.50	11.2	1.623	2.04	1.996

Table 5.5 Experimental Results

F Before H. J.	θ	Water Depth Ratio	Pressure Ratio	% Variation *
3.08	11.5	1.74	2.216	4.3
	16.6	1.46	1.709	36.4
	11.2	2.25	3.333	67

* Difference With Respect to 2-D Shock-Expansion Theory

The rather large value of water depth ratio on surface 4 can be explained by the fact that the surface is too short. As a consequence of this, the water overshoots and before it can reach equilibrium is deflected by the expansion. As a result, the average value is high because the surface is highly dominated by the transition region. For surface 2, the value of water depth ratio was less expected since both theories predict higher results. A geometric analysis of the angle of the wave produced by the fuselage and the position of the capsule, showed the former

directly impinging on surface 2, which was confirmed by direct observation of the model in water. The convergence of the two shocks (jumps) is to produce a "slight additional deflection of the flow away from the surface" [Ref. 2]. This deflection occurs below the point of intersection of the two jumps, but is usually small and therefore does not fully explain the lower water depth profile on the surface.

In order to estimate the effect of the change in the effective angle of attack in the density and pressure ratios, the 2-D shock-expansion theory was used to obtain these ratios and then they were compared with the water depth ratios obtained from the experiments applying the modified analogy.

For the capsule moving with V1, the effective angle of attack of the capsule was 3.63° and the Mach Number was 2.457, a slight variation in direction as well as in magnitude. With these initial conditions for the capsule, the following data was obtained:

Table 5.6 Theoretical Results of Pressure and Density Ratio For Static and Dynamic Case 1

Condition	Surface	Density Ratio	% Variation	Pressure Ratio	% Variation
Static	2	1.970		2.684	
	4	1.622		1.995	
V 1	2	2.213	-12.3	3.243	-20.8
	4	1.403	13.5	1.613	19.2

**Table 5.7 Experimental Results of Pressure and
Density Ratio For Static and Dynamic Case 1**

Condition	Surface	Density Ratio	% Variation	Pressure Ratio	% Variation
Static	2	1.458		1.706	
	4	2.25		3.334	
V 1	2	1.694	-16.2	2.127	-24.7
	4	1.276	43.3	1.409	57.7

The variation in density and pressure ratio on surface 2 are similar for both cases whereas for surface 4 the difference in % of variation is approximately four times. Based on this information, it could be said that the change in flow condition is primarily due to the change in effective angle of attack on surface 2. For surface 4 the difference between the theoretical and experimental case was believed to occur mainly due to the inadequate dimensions of the model. A more definite answer could be found analyzing further cases.

The analysis of additional cases revealed an interesting situation occurring for the theoretical calculation of the flow parameters using the hydraulic theory and the calculation of flow parameters using the 2-D shock expansion theory for V 2. In both cases the theories predicted separation because the combination of flow deflection angle due to the new effective angle and Froude and Mach numbers respectively, yielded no solution for surface 4. This situation did not occur in the experimental cases where the flow remained attached at all times for these configurations. This could indicate that the variation in the flow conditions cannot

be solely explained by the motion of the capsule since this approach predicted separation which in reality did not occur.

A comparison of the flow parameters between the two velocities showed an expected behavior for surface 4, i.e., for higher velocities, higher water depth ratios occurred. For surface 2 the same trend was observed, which was not predicted by the change in the effective angle of attack approach. This could also indicate the presence of an effect due to the fuselage. These aspects are inconclusive and it is felt that more experimentation is needed to explain this behavior.

VI. Conclusions And Recommendations

6.1 Conclusions

A. It is possible to obtain substantially better quantitative agreement between theoretical and experimental values if the so called "modified" analogy is used in the range of Froude numbers considered.

B. The so called "Modified" Gas Hydraulic Analogy presents itself as a good tool for the modeling of simple separation cases when the appropriate model size and shape are considered. This is mainly because of the relatively simple way in which quantitative as well as qualitative data of simulated unsteady conditions can be obtained.

C. There is a marked difference in the water depth distribution on the surface of the capsule when static and dynamic cases are considered. Based on this, it is clear that in order to model the separation aerodynamic of the capsule more in accordance to reality when the Gas Hydraulic Analogy is used, it is necessary to include the motion of the capsule.

D. Different motion profiles produce different water depth distributions and consequently different values for the aerodynamic parameters, so a careful selection of the motion profile of the capsule must be made.

E. The size of the model is of crucial importance if good quantitative data is desired. If the model is too small, the agreement between theoretical and experimental values is poor. The geometry of the model is also important if flow separation is to be avoided since separation will occur if the angles of the body are too large. The determination of the correct size and shape should be done based mainly on a set of experimental runs.

F. The presence of boundary layer on the surfaces of the models, which is not considered in the derivation of the analogy, has the effect of bringing the

experimental values in closer agreement with the theory by producing an effective shape of the model that causes bigger flow deflection angles.

G. It is possible to get a good representation of the velocity of the flow on a hydraulic simulator of the type used, by determining the variation of the water depth as a function of head height; this provided the value of the discharge coefficient is well known.

6.2 Recommendations

A. The Hydraulic Simulator has been brought to operational state but there are a number of aspects that need be addressed to improve its performance. The determination of the conditions under which uniform flow is achieved is still inconclusive. This is specially true for lower Froude numbers (between 20 and 40 mm of Head Height). It is recommended that a new calibration procedure be implemented to improve the test conditions. This should include taking more velocity and water depth measurements, with special consideration of the low head height range.

B. The cause of the ripples created at the nozzle exit that were responsible for the appearance of turbulent spots merging to create a turbulence flow between 0.5 and 1.0 meter downstream from the nozzle, should be investigated and corrected.

C. The interactions and reflections of shock and expansion waves in water is a factor present in any case where the separation of two bodies is analyzed. If accurate quantitative data is needed, a study of the effect of these factors on the water depth distribution is necessary. It is therefore recommended that in any further study of this type, a careful analysis of this aspect be included.

D. In order to make the experimenter more self-sufficient, it is highly advantageous to implement a small photographic lab so that the acquired images

can be processed immediately. This will provide an enormous saving in time to the person performing the experiments (At present, the film must be developed at Multimedia Center, Building 19, Area B at WPAFB)

E. It is definitively worthwhile to investigate a way of making the laser line generator more efficient. The way it is set up now allows its use in very simple geometries and if a new position is needed the system has to be re-aligned which is extremely time consuming if the model has a more complicated geometry.

F. The method of processing the numerical data must be improved, For this, an integrated computer code can be implemented that processes the coordinates of the water profile to calculate from them all the flow parameters of interest along with the corresponding plots.

G. Once all these problems have been corrected, new avenues of investigation can be attempted, such as ejection with different motion profiles, ejection at transonic speeds and modeling of ejection rockets by water jets to name a few.

VII. References

- (1) Ippen, A.T., Harleman, D. R. F. et al Studies on the Validity of the Hydraulic Analogy to Supersonic Flow Parts I through V. Air Force AF-TR-5985 1950-1952.
- (2) Ippen, A. T. Mechanics of Supercritical Flow Proceedings of the A.S.C.E., Vol 75 N° 9, 1949.
- (3) Laitone, E. V. "A Study of Transonic Gas Dynamics by the Hydraulic Analogy" Journal of the Aeronautical Sciences Vol 19 N° 4, 1952.
- (4) Bakhmeteff, B. et al The Hydraulic Jump in Terms of Dynamic Similarity Transactions of the A.S.C.E. N° 101, 1936.
- (5) Daugherty, R. L. et al Fluid Mechanics With Engineering Applications MacGraw-Hill 5th Ed., 1989.
- (6) Zucrow, M. and Hoffmann, J. Gas Dynamics Vol I John Wiley and Sons, 8th Ed., 1976
- (7) Robertson, J. M. Hydrodynamics in Theory and Applications Prentice Hall, 1965.
- (8) Anderson, J. D. Modern Compressible Flow MacGraw-Hill, 1982.
- (9) Liu, P. et al A Hydraulic Simulator for Physical Modeling of Unsteady Hypersonic Flow WR-TR-92-3123, 1993.
- (10) Ippen, A. T. et al Verification of Theory for Oblique Standing Waves Transactions of A.S.C.E., 1954

- (11) Chow, V. T. Open Channel Hydraulics MacGraw-Hill Co., 1959
- (12) Warren, C. H. Application of the Hydraulic Analogy to Internal Subsonic Flow U.S. Army Missile Command Report N° RG-TR-67-19, 1967.
- (13) Liepmann, H. W. and Roshko, A. Elements of Gas Dynamics John Wiley and Sons, 8th Ed., 1967.
- (14) Ferri, A. Elements of Aerodynamics of Supersonic Flow Mac Millan Co. N.Y., 1949.

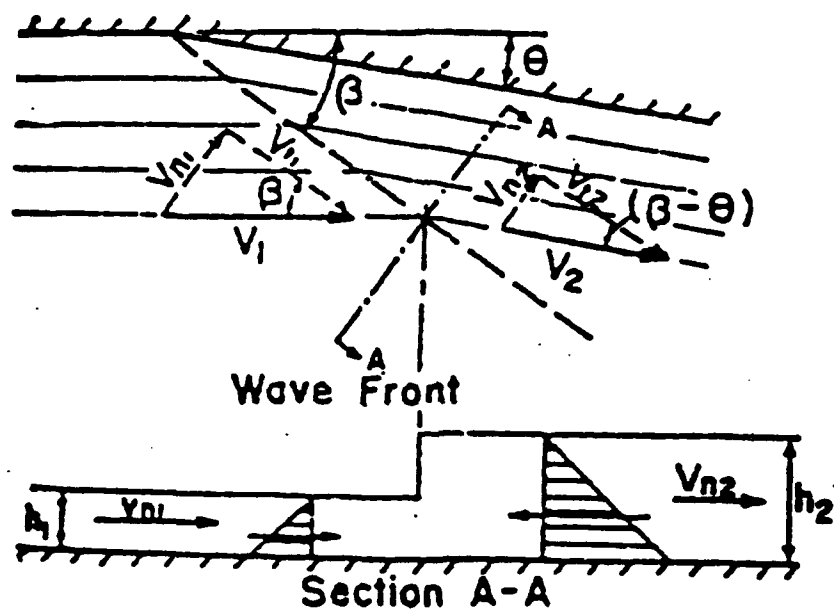


Fig. 2.1(a) Oblique Hydraulic Jump From Ref. [10]

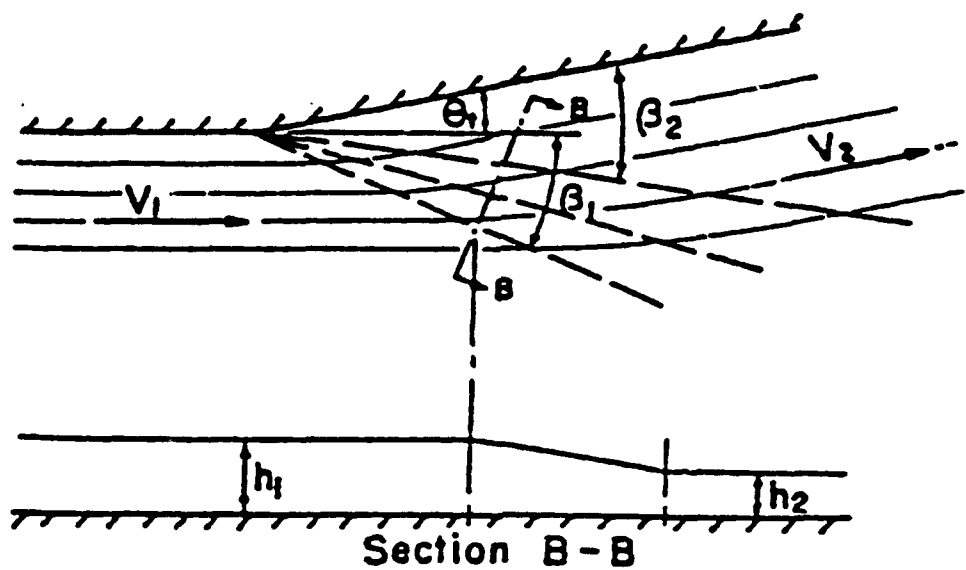


Fig. 2.1(b) Oblique Expansion Wave From Ref. [10]

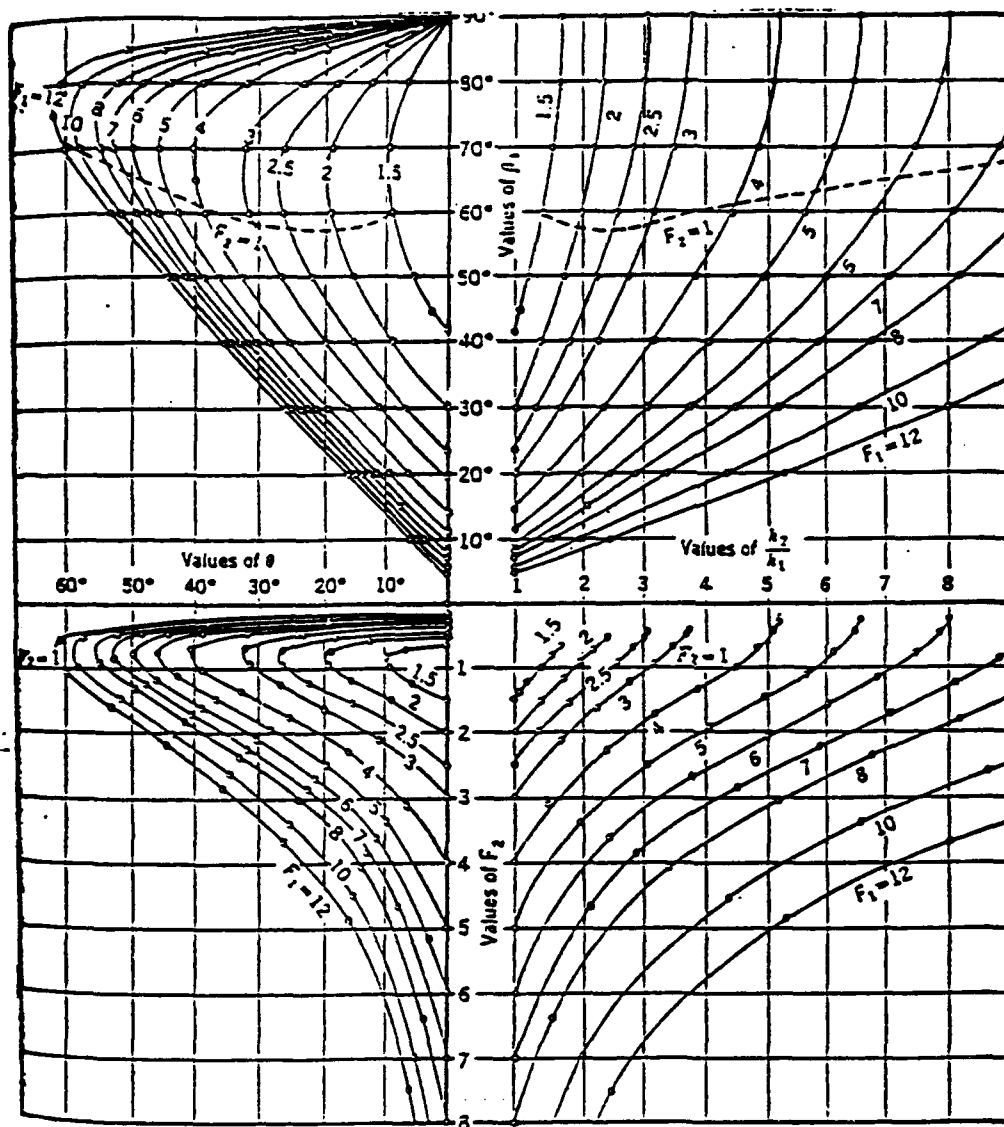


Fig. 2.2 Graphical Relationship Between $F_1, \theta, \beta_1, F_2$ and $\frac{h_2}{h_1}$ for Water From Ref. [2]

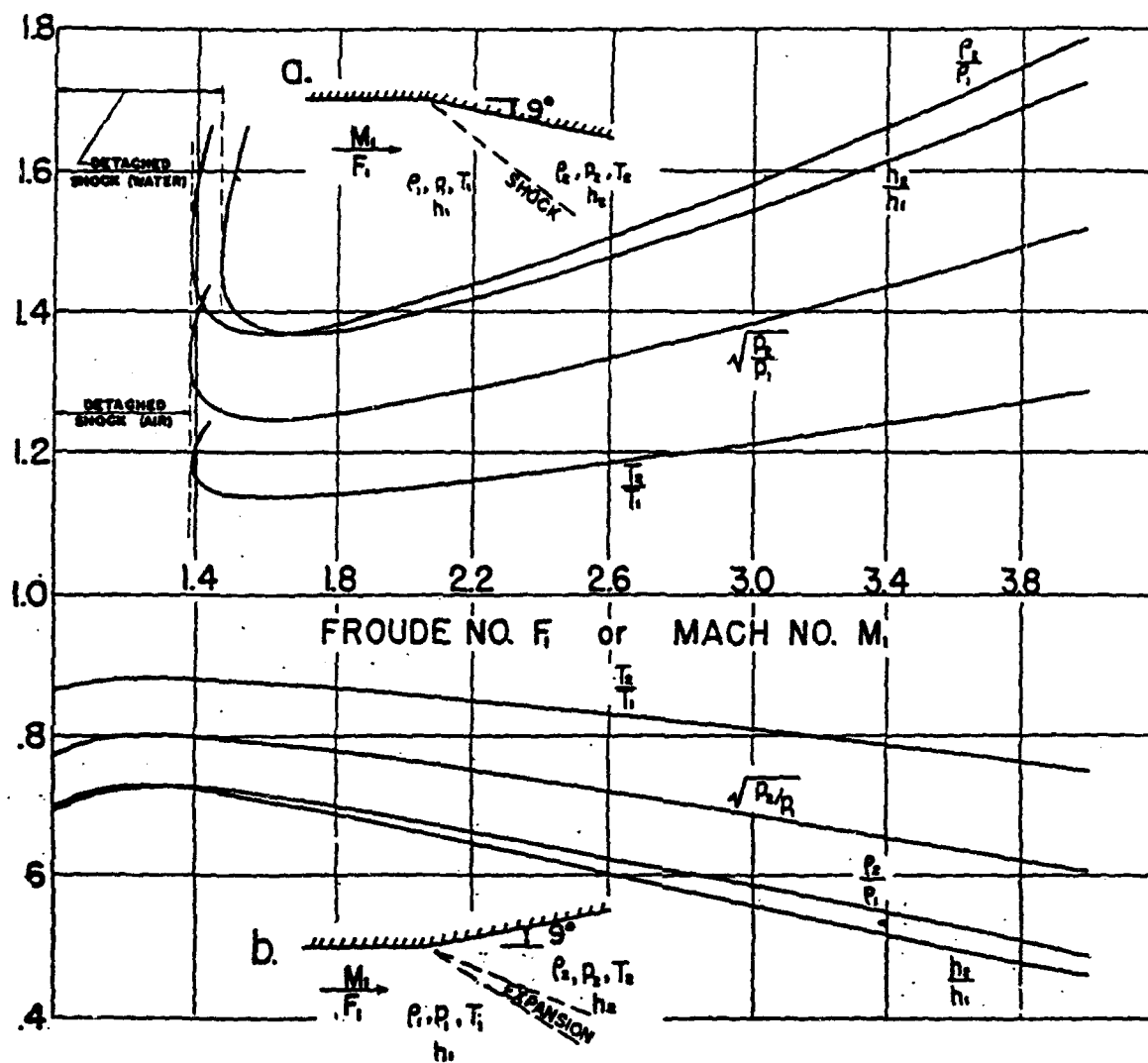
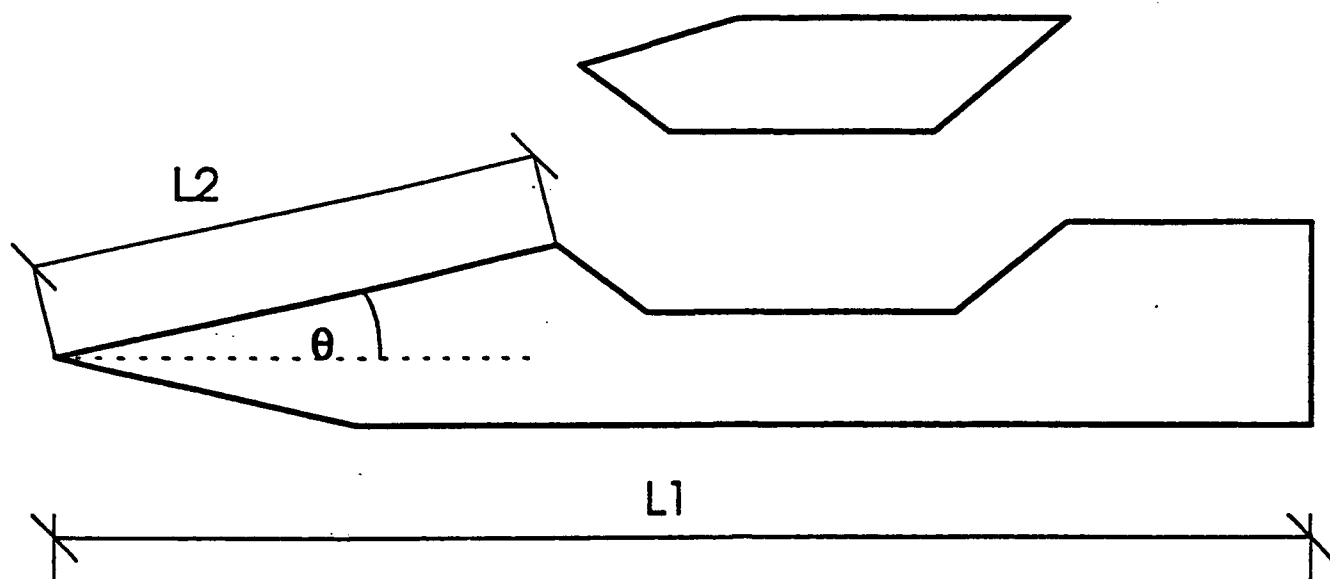


Fig. 2.3 Theoretical Correlation Between Analogous Water and Air Characteristics for $F_1 = M_1$ From Ref. [1]

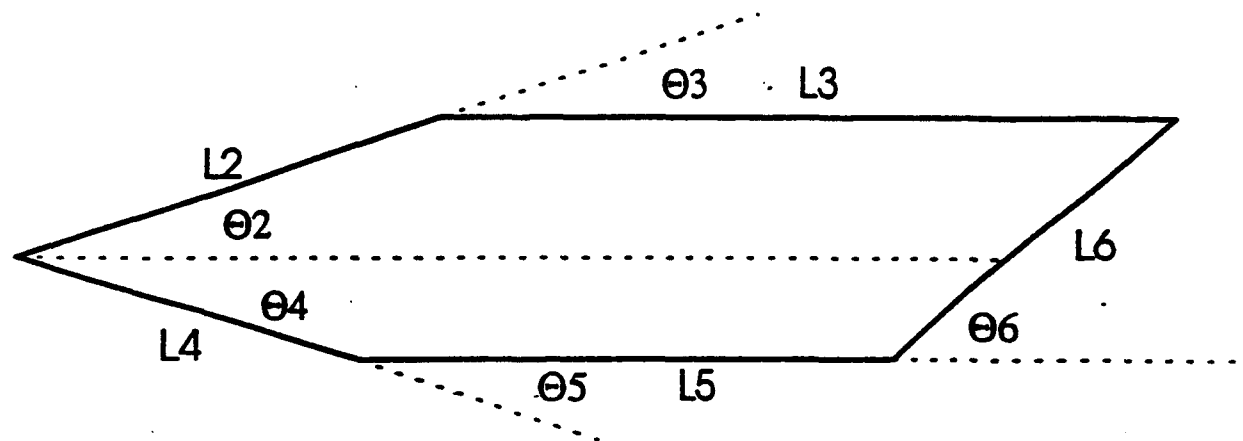


Theta = 11.5 degrees

L1 = 53 cm

L2 = 19 cm

Fig. 3.1(a) Model Used on the Experiments



L2 = 8.8 cm

Theta 2 = 16.6 deg

L3 = 10.6 cm

Theta 3 = 17.05 deg

L4 = 6.8 cm

Theta 4 = 11.2 deg

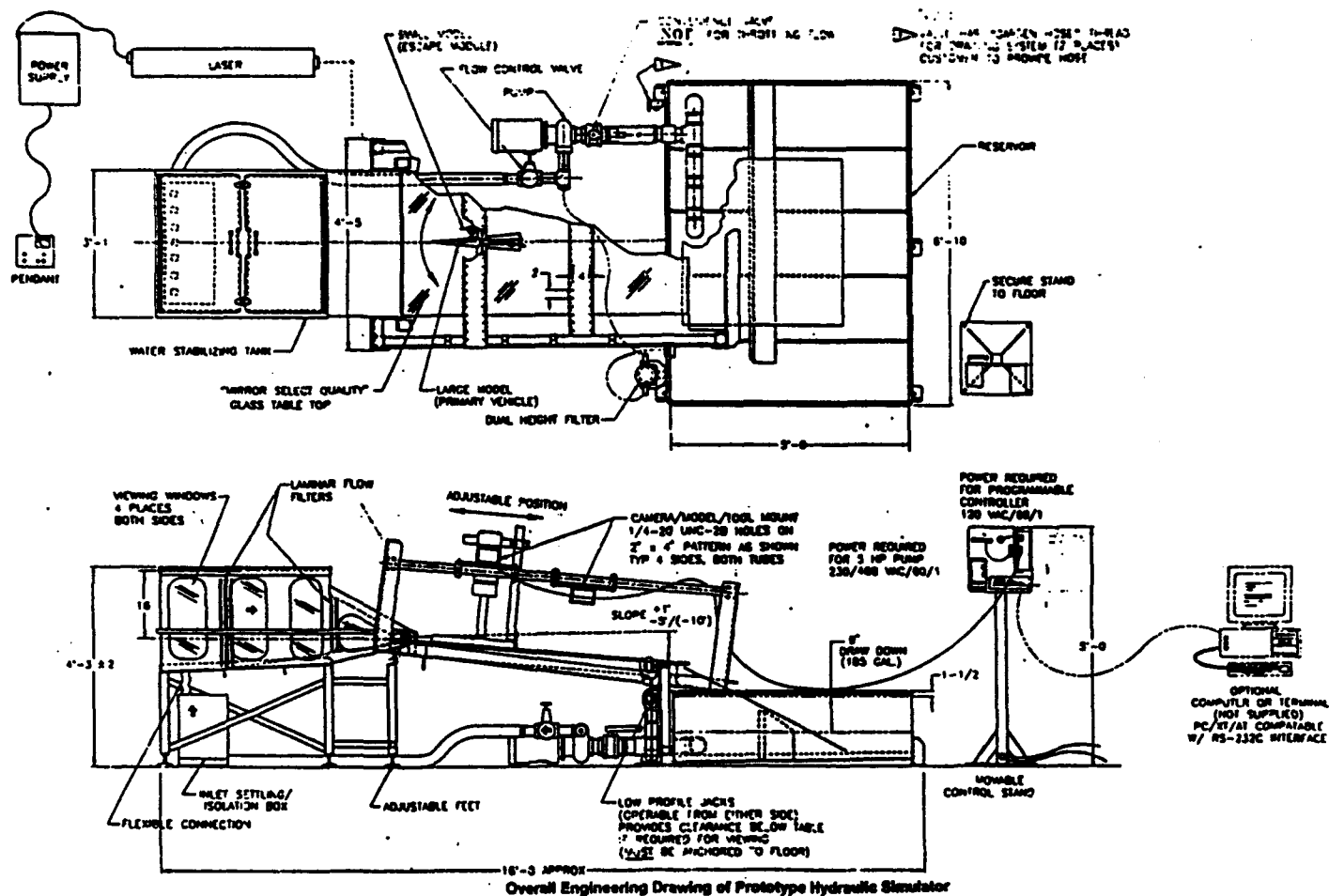
L5 = 7.0 cm

Theta 5 = 11.5 deg

L6 = 6.4 cm

Theta 6 = 36.4 deg

Fig. 3.1 (b) Model Used on the Experiments



3.2 Hydraulic Simulator

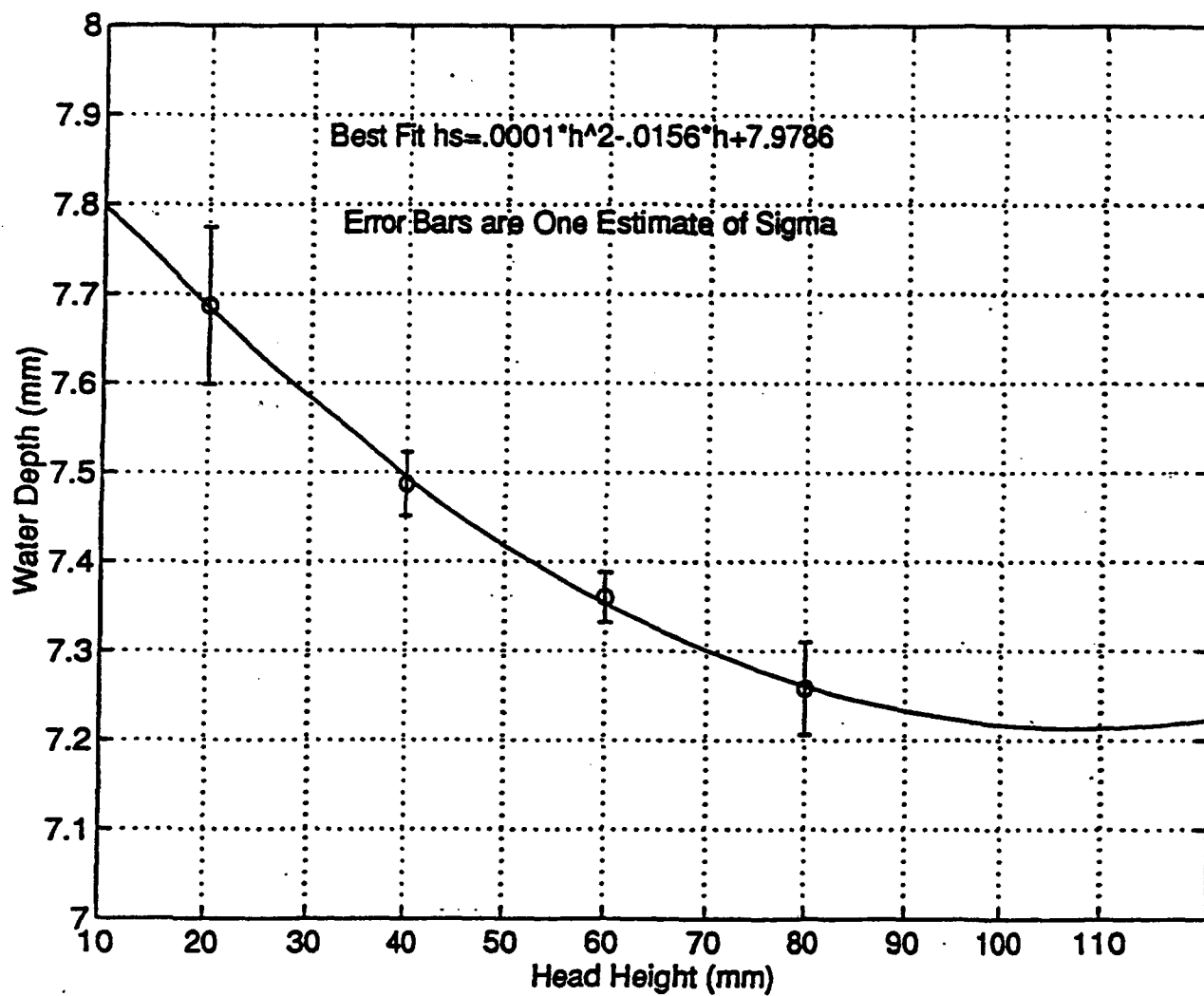


Fig. 4.1 Best Fit of Water Depth vs Head Height

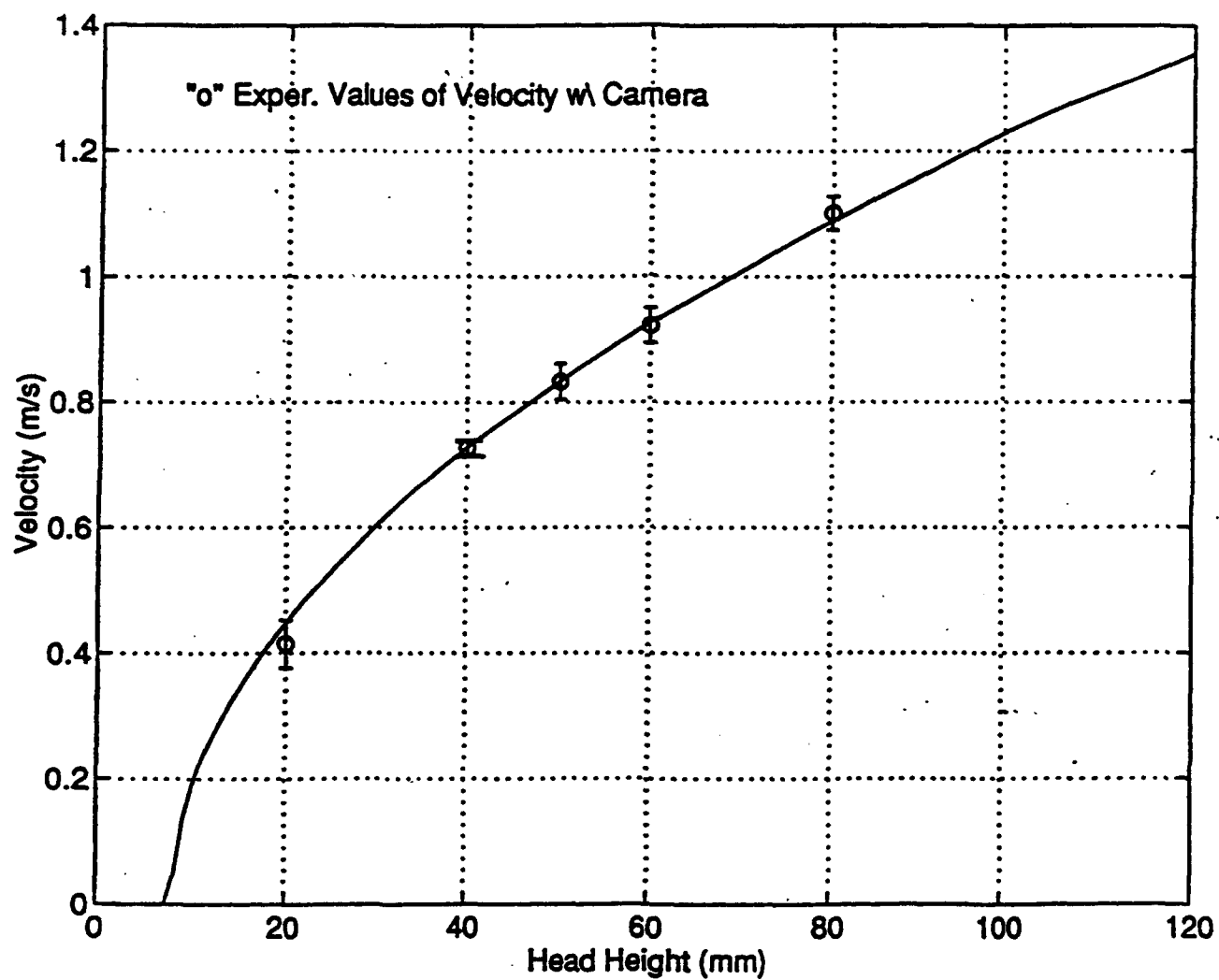


Fig. 4.2 Velocity Measurements Using High Speed Camera as Compared to the Velocity from the Energy Equation

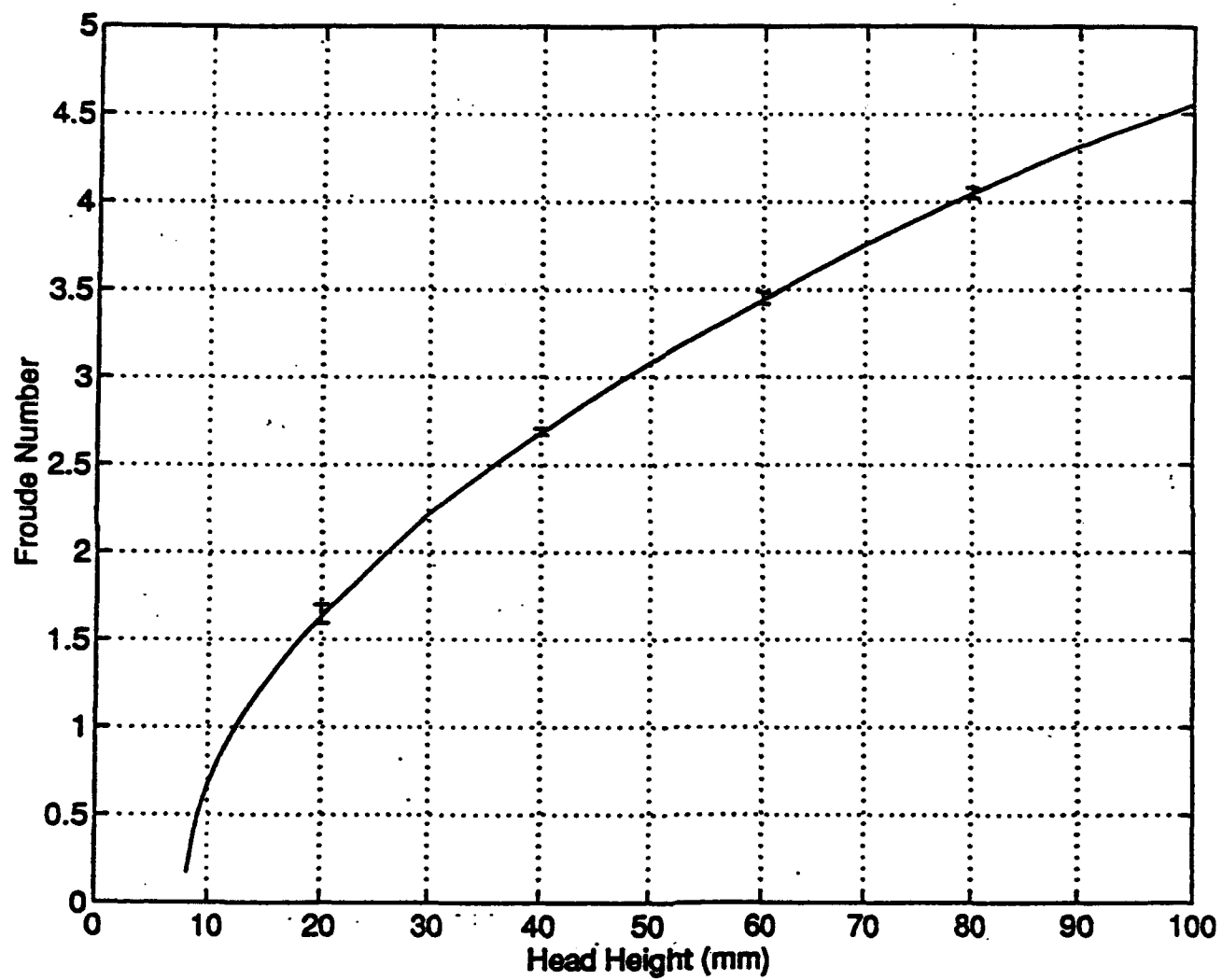


Fig. 4.3 Froude Number vs Head Height

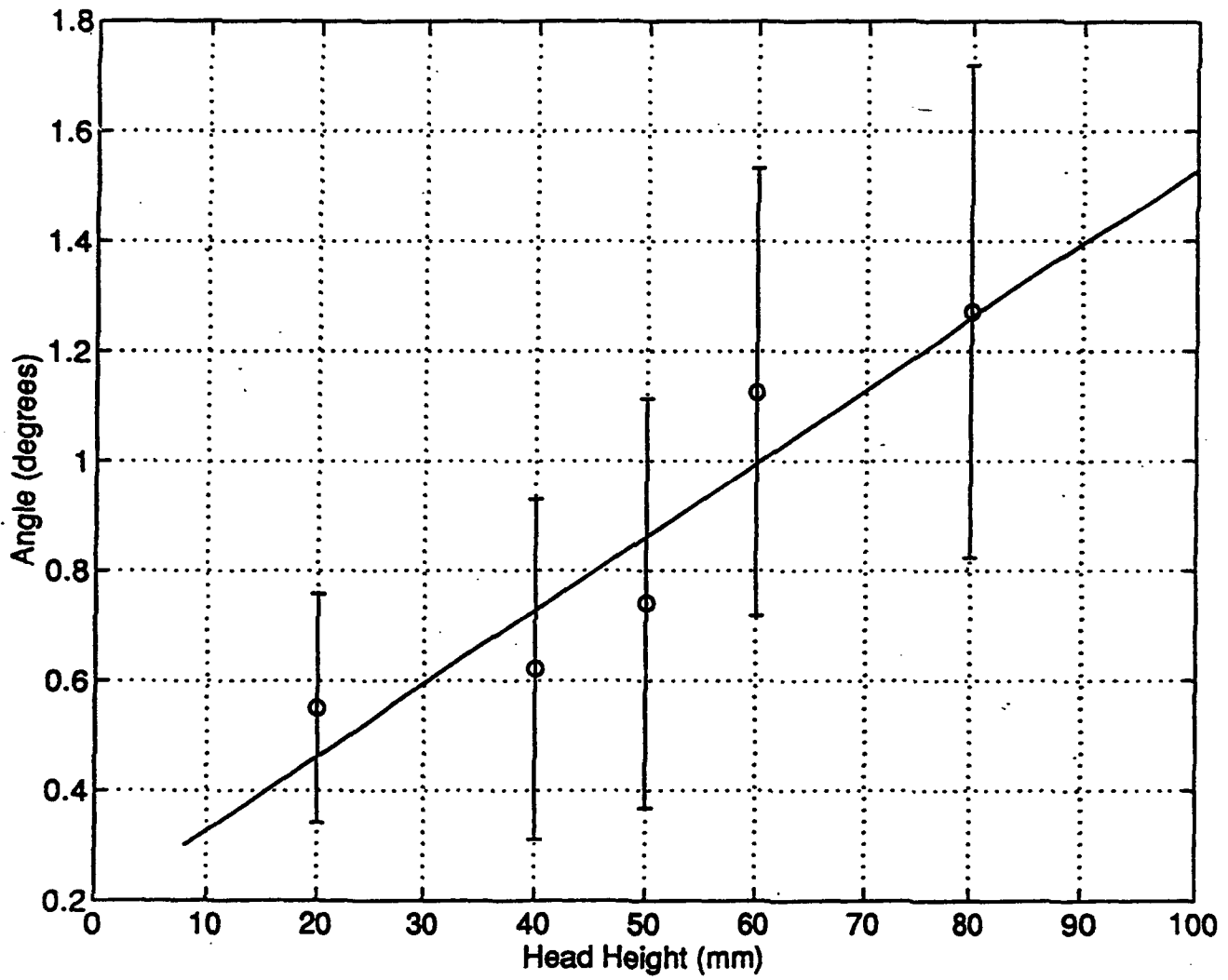


Fig. 4.4 Uniform Velocity vs Head Height

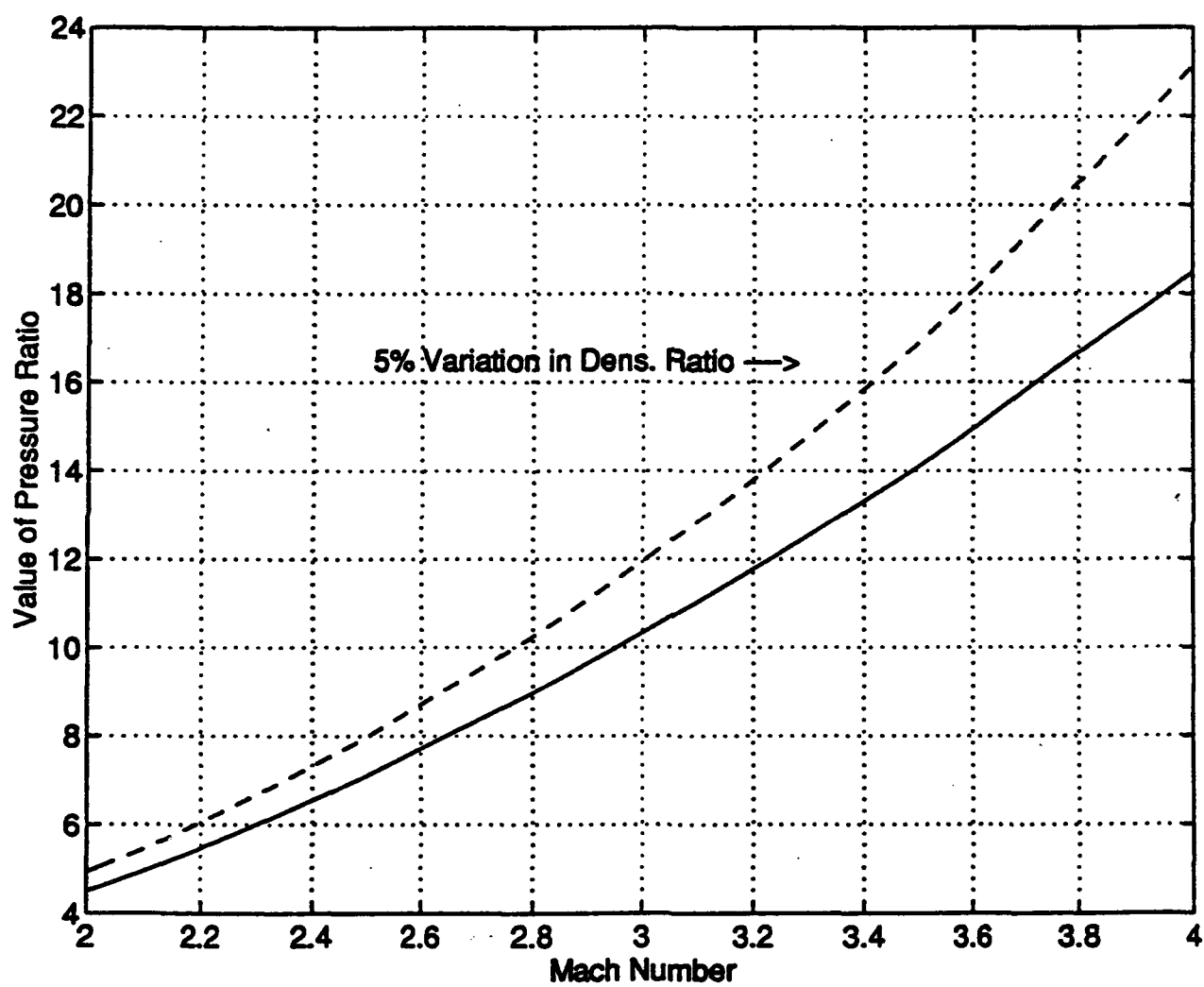


Fig. 4.5 **Pressure Ratio Sensitivity as a Function of Mach Number**

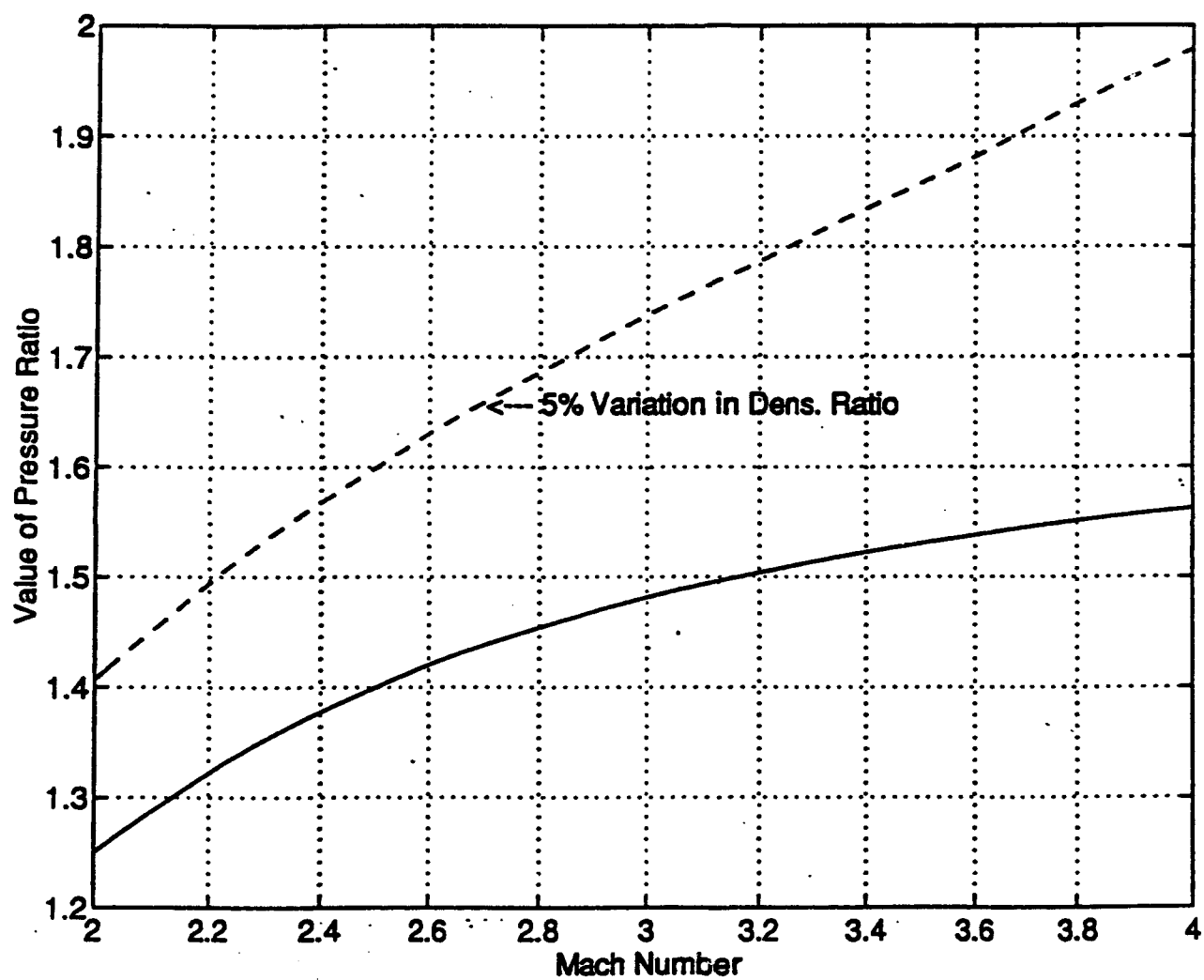
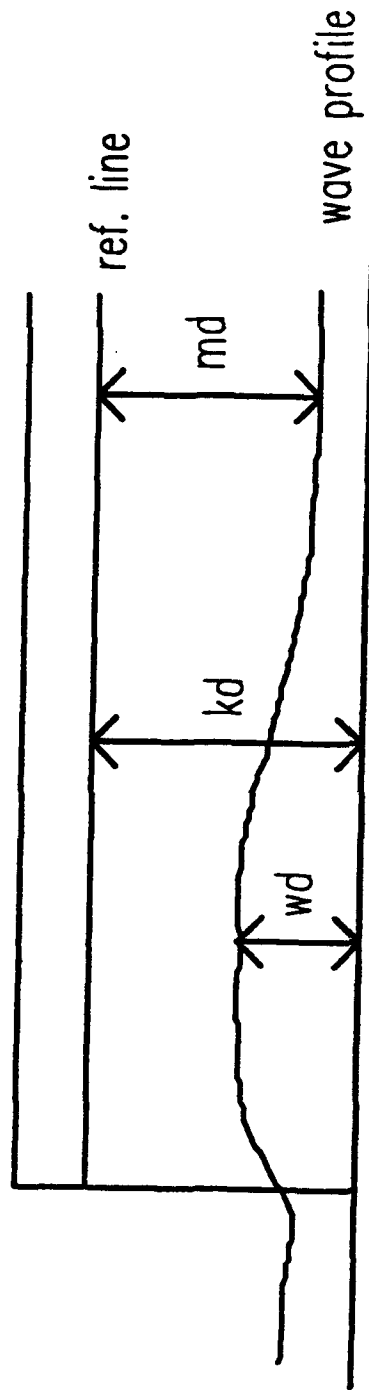


Fig. 4.6 Pressure Coefficient Sensitivity as a Function of Mach Number



wd = Water Depth
 kd = Known Distance
 md = Measured Distance

Fig. 4.7 Water Depth Measurements on Model

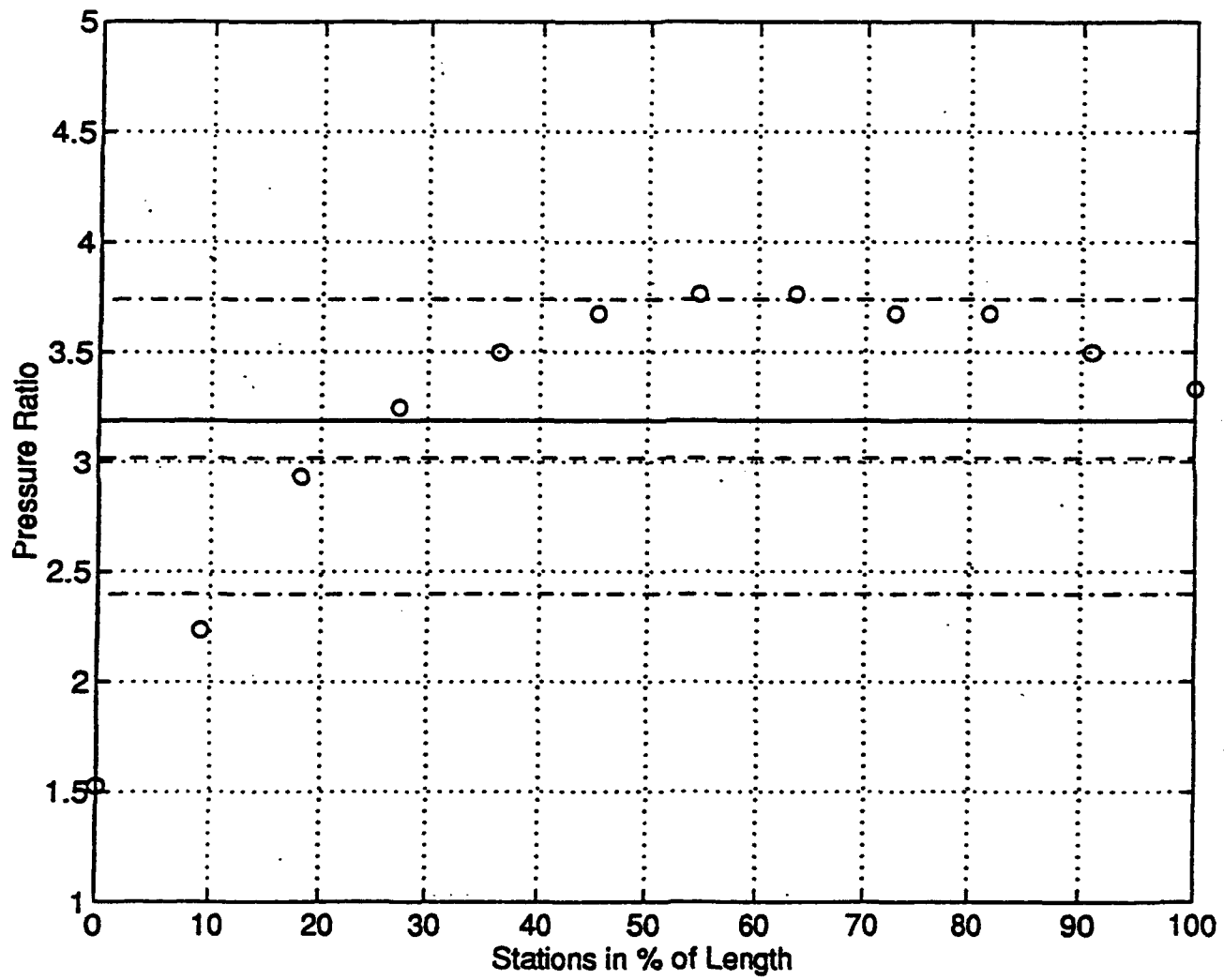


Fig. 5.1 Pressure Ratio for Surface 2 of Case 1

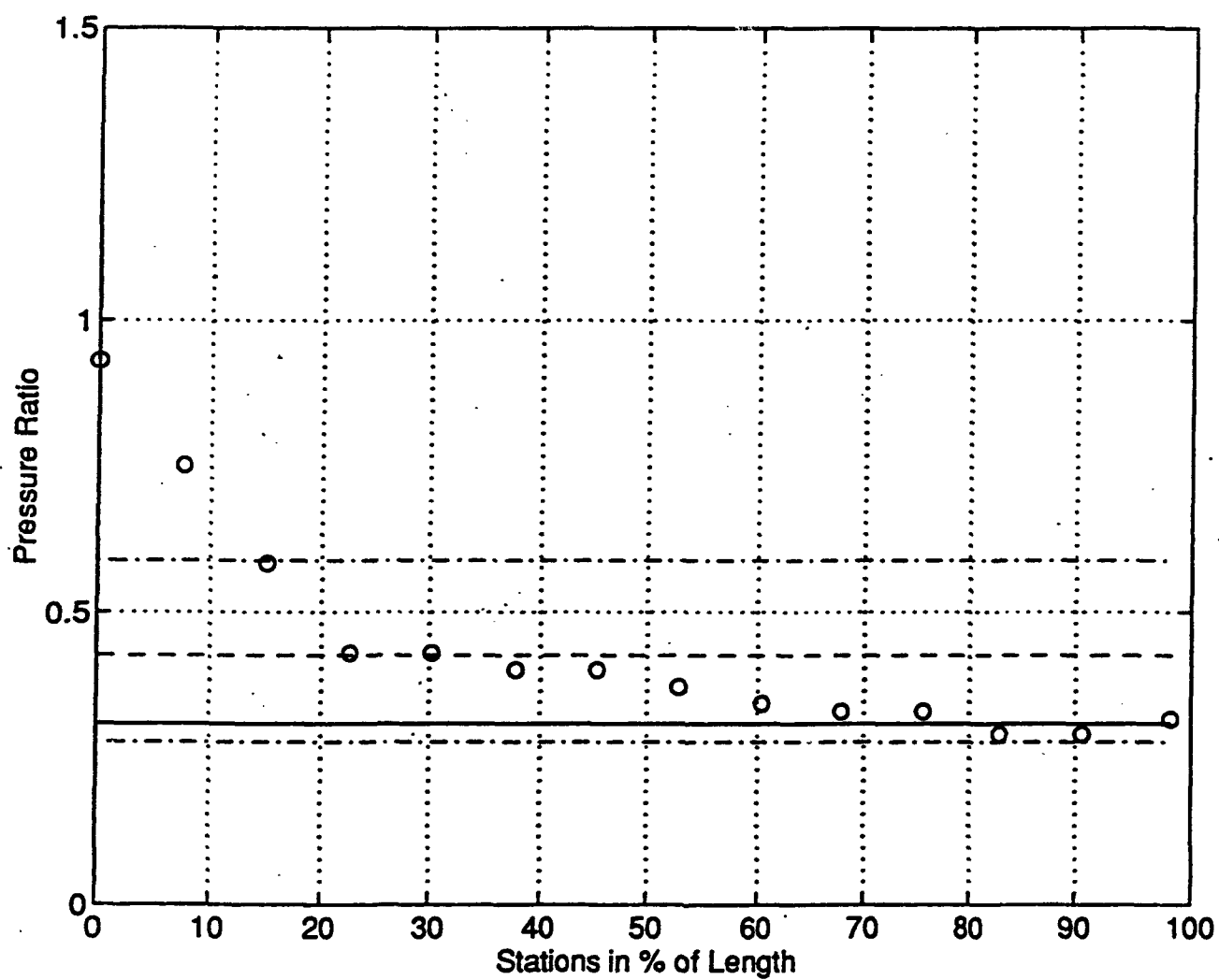


Fig. 5.2 Pressure Ratio for Surface 3 of Case 1

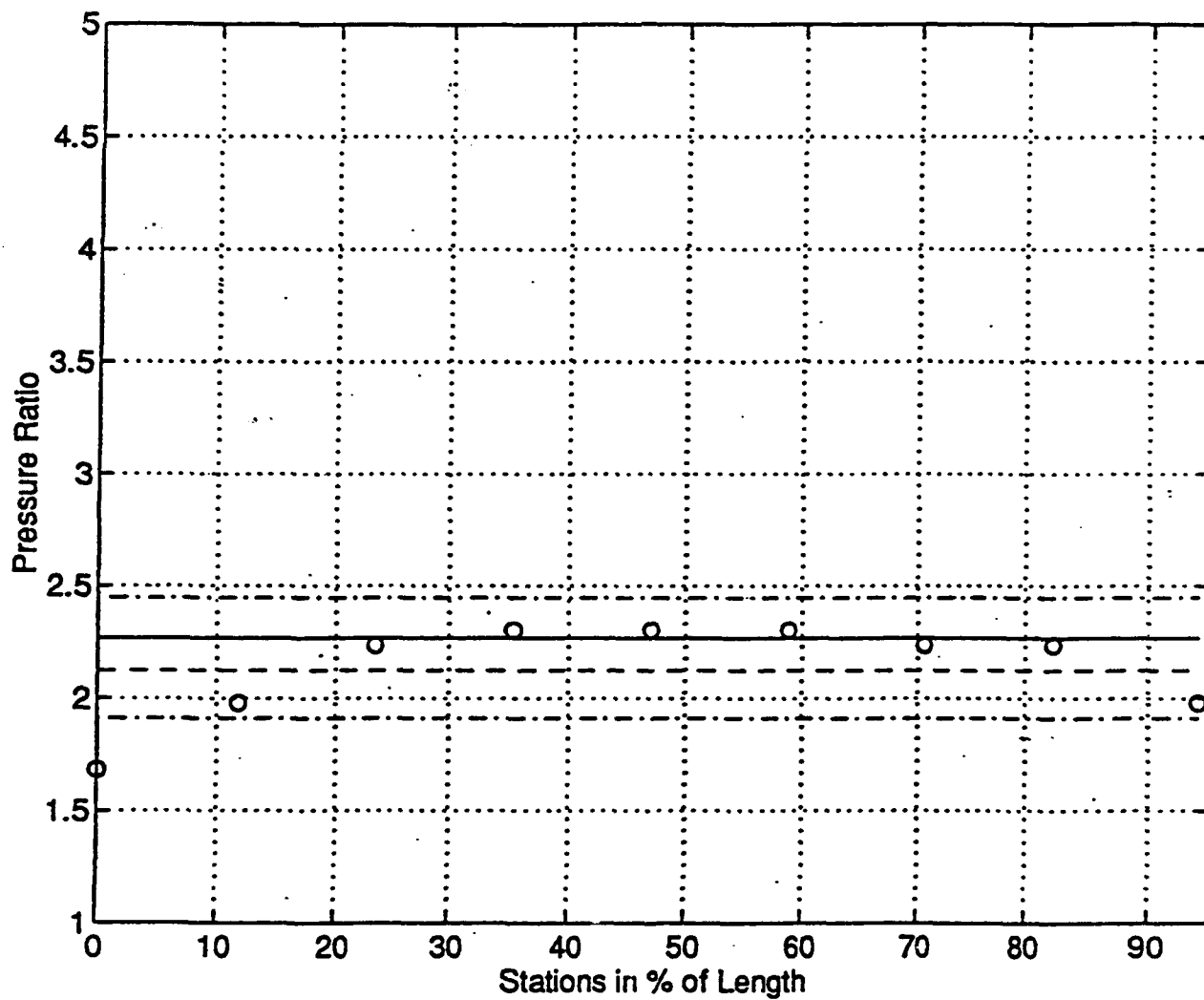


Fig. 5.3 Pressure Ratio for Surface 4 of Case 1

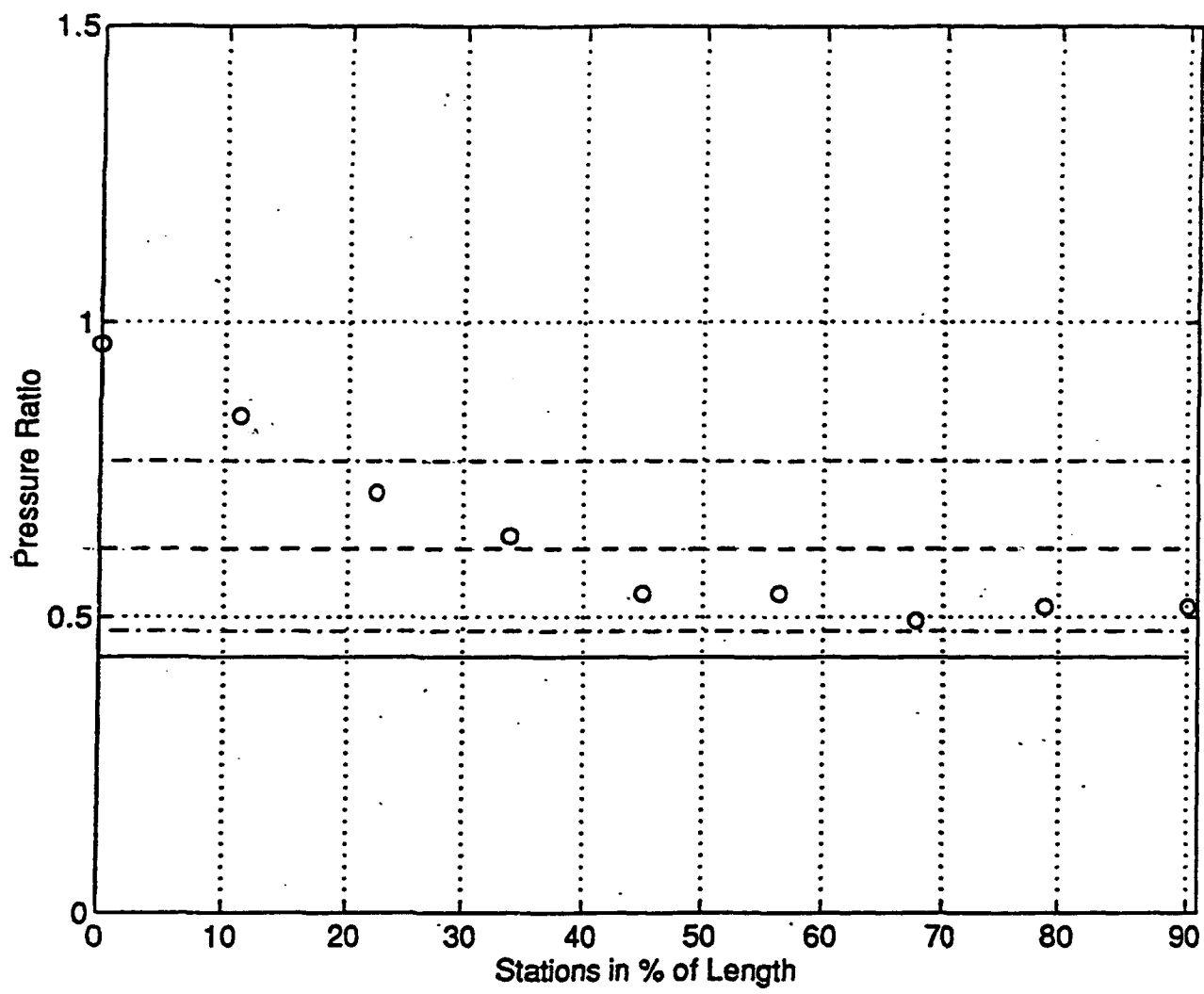


Fig. 5.4 Pressure Ratio for Surface 5 of Case 1

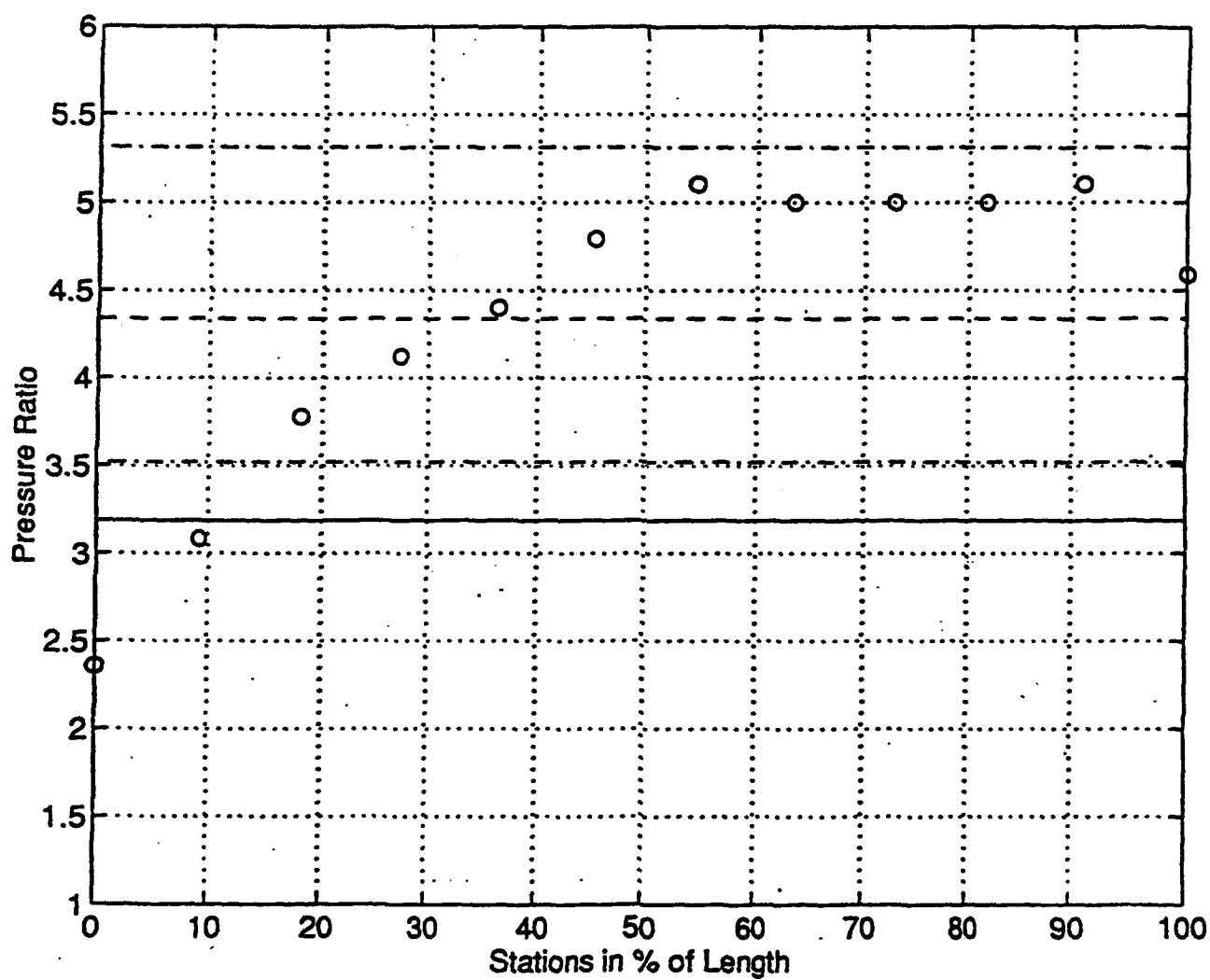


Fig. 5.5 Pressure Ratio for Surface 2 of Case 2

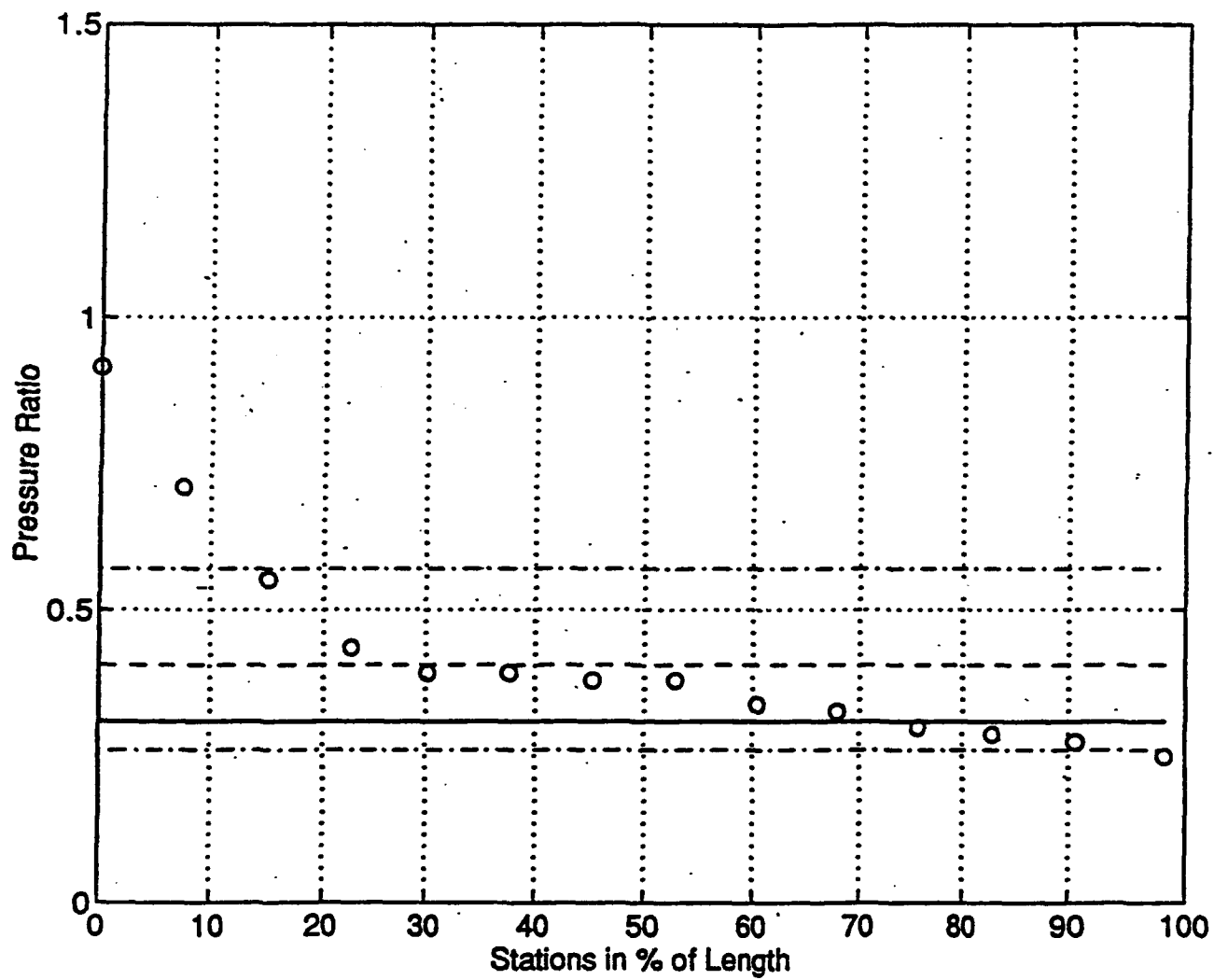


Fig. 5.6 Pressure Ratio for Surface 3 of Case 2

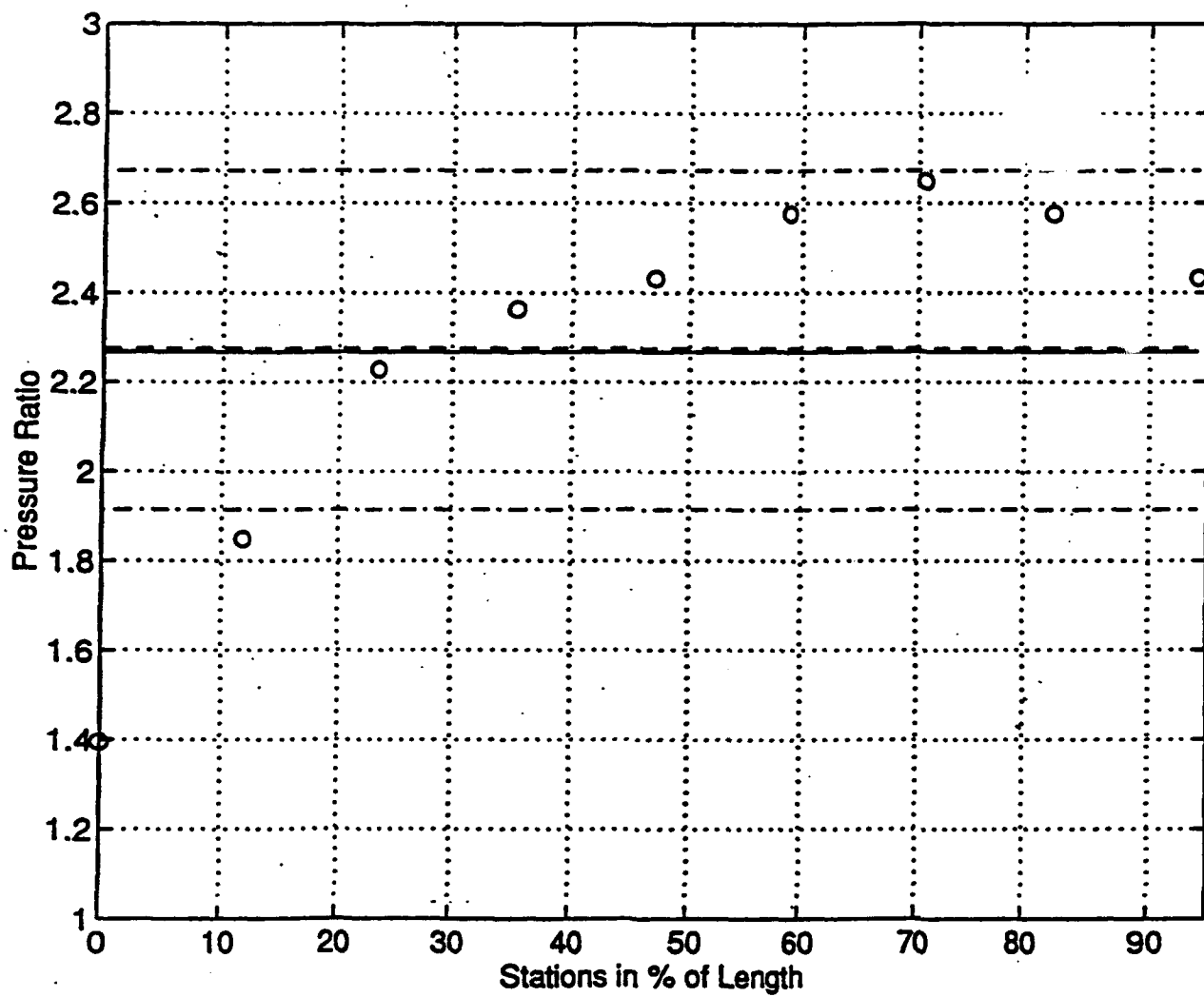


Fig. 5.7 Pressure Ratio for Surface 4 of Case 2

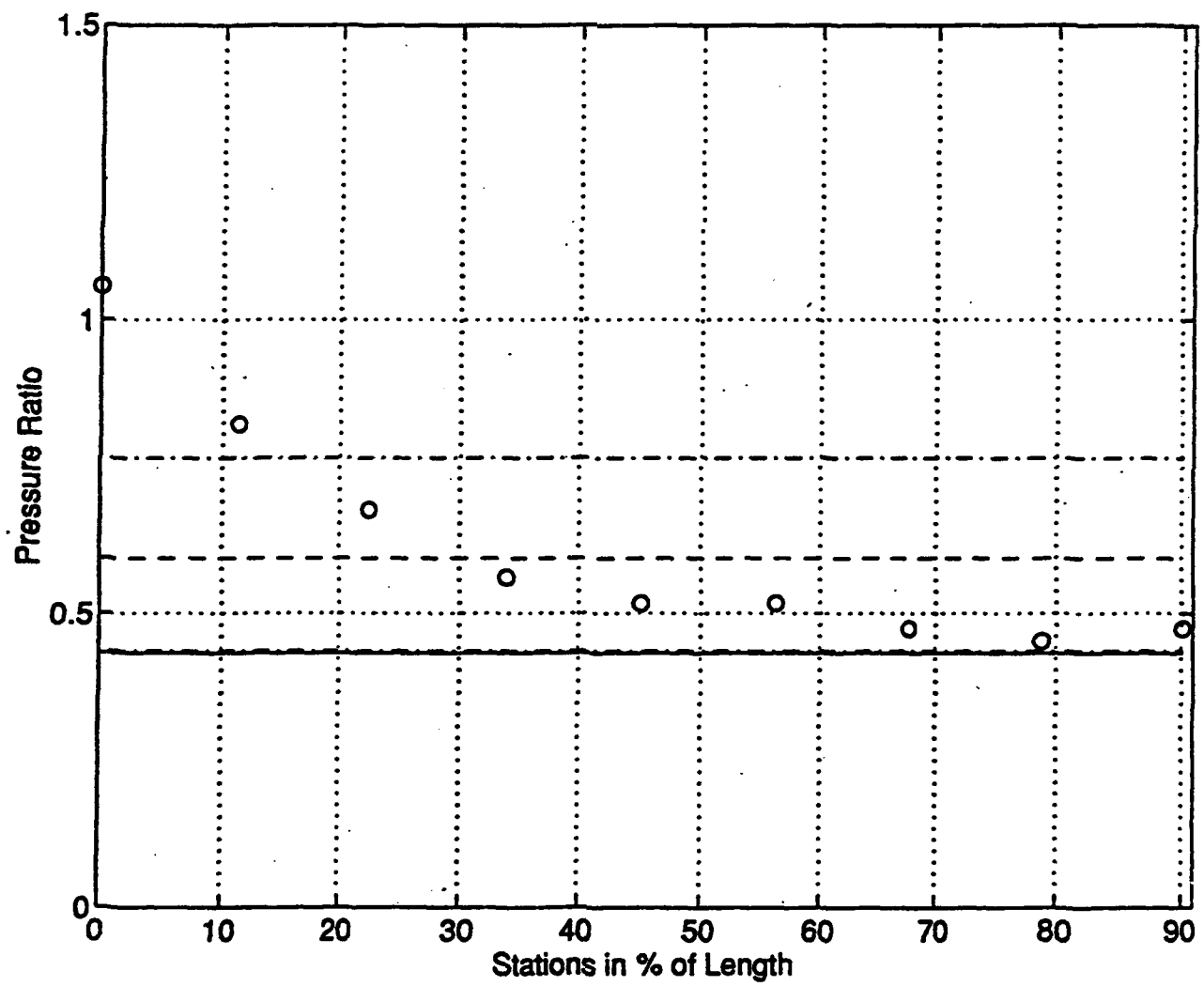


Fig. 5.8 Pressure Ratio for Surface 5 of Case 2

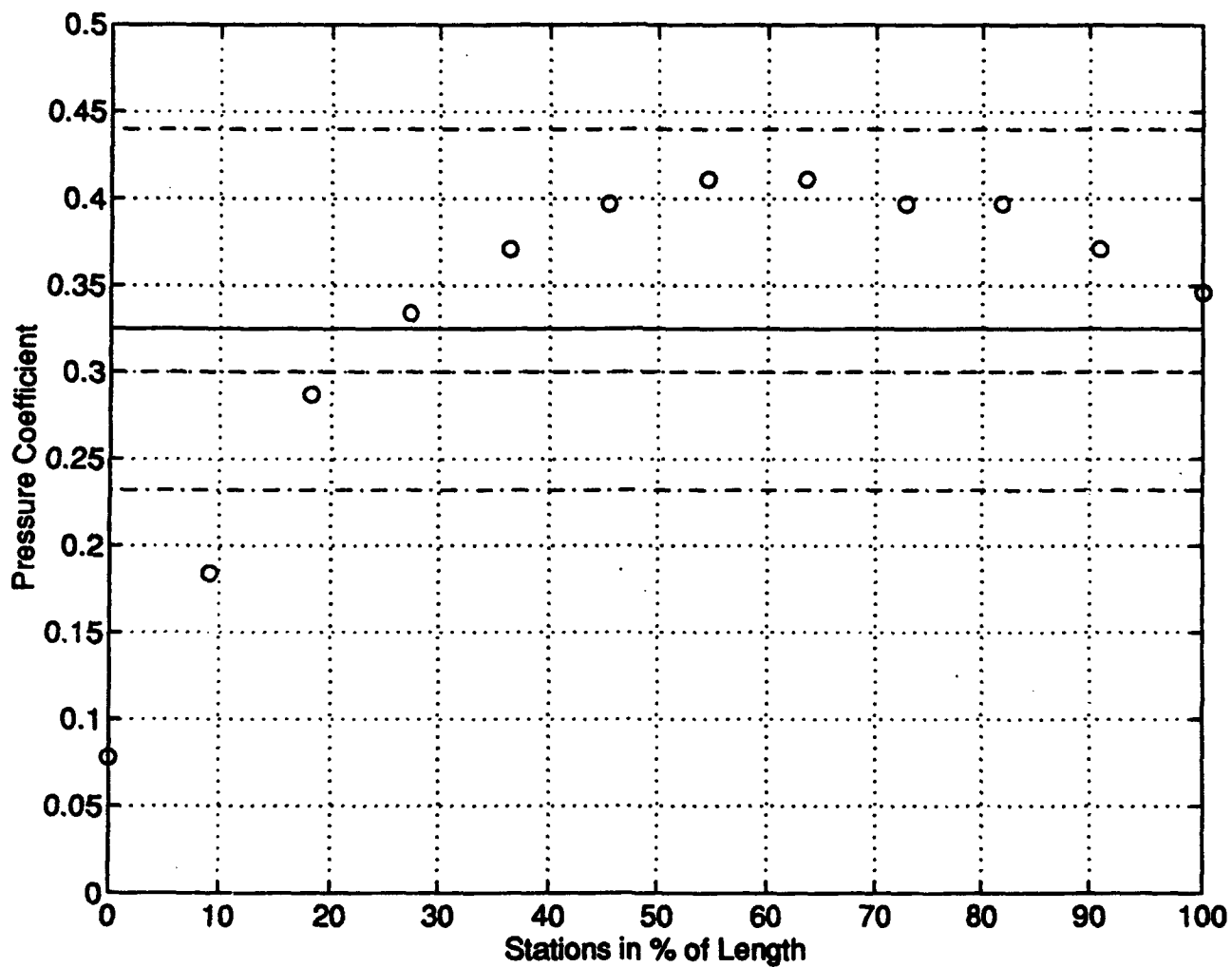


Fig. 5.9 Pressure Coefficient for Surface 2 of Case 1

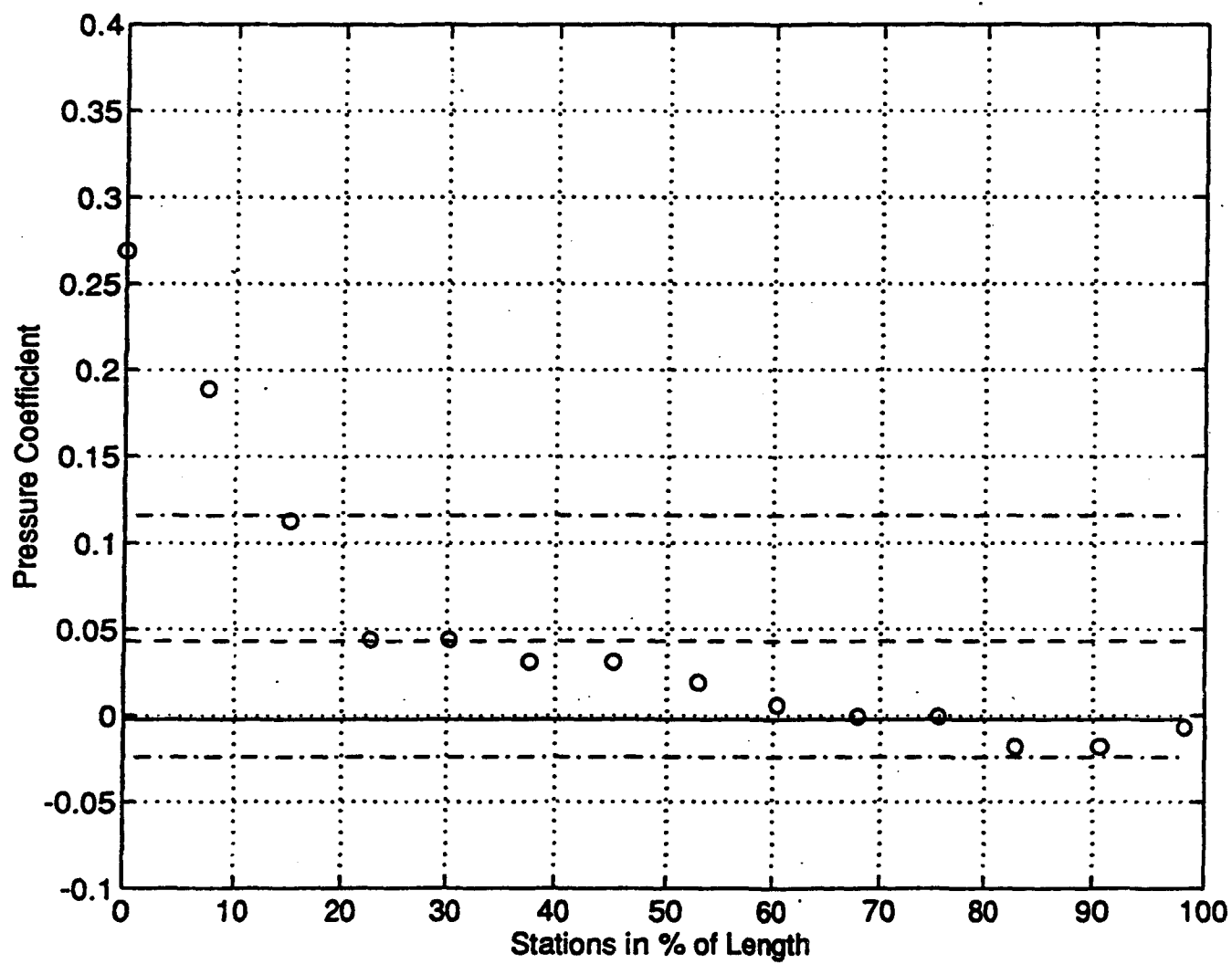


Fig. 5.10 Pressure Coefficient for Surface 3 of Case 1

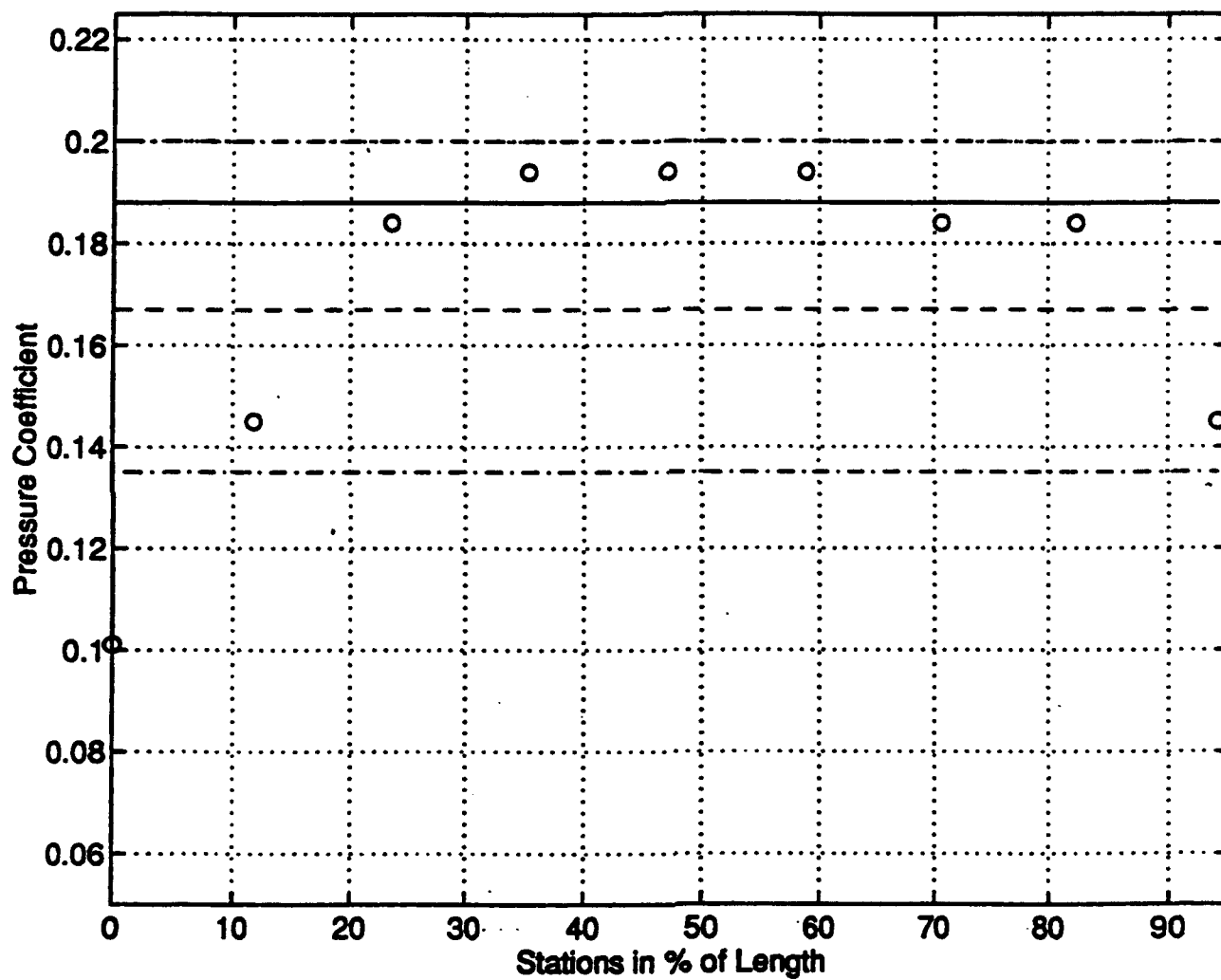


Fig. 5.11 Pressure Coefficient for Surface 4 of Case 1

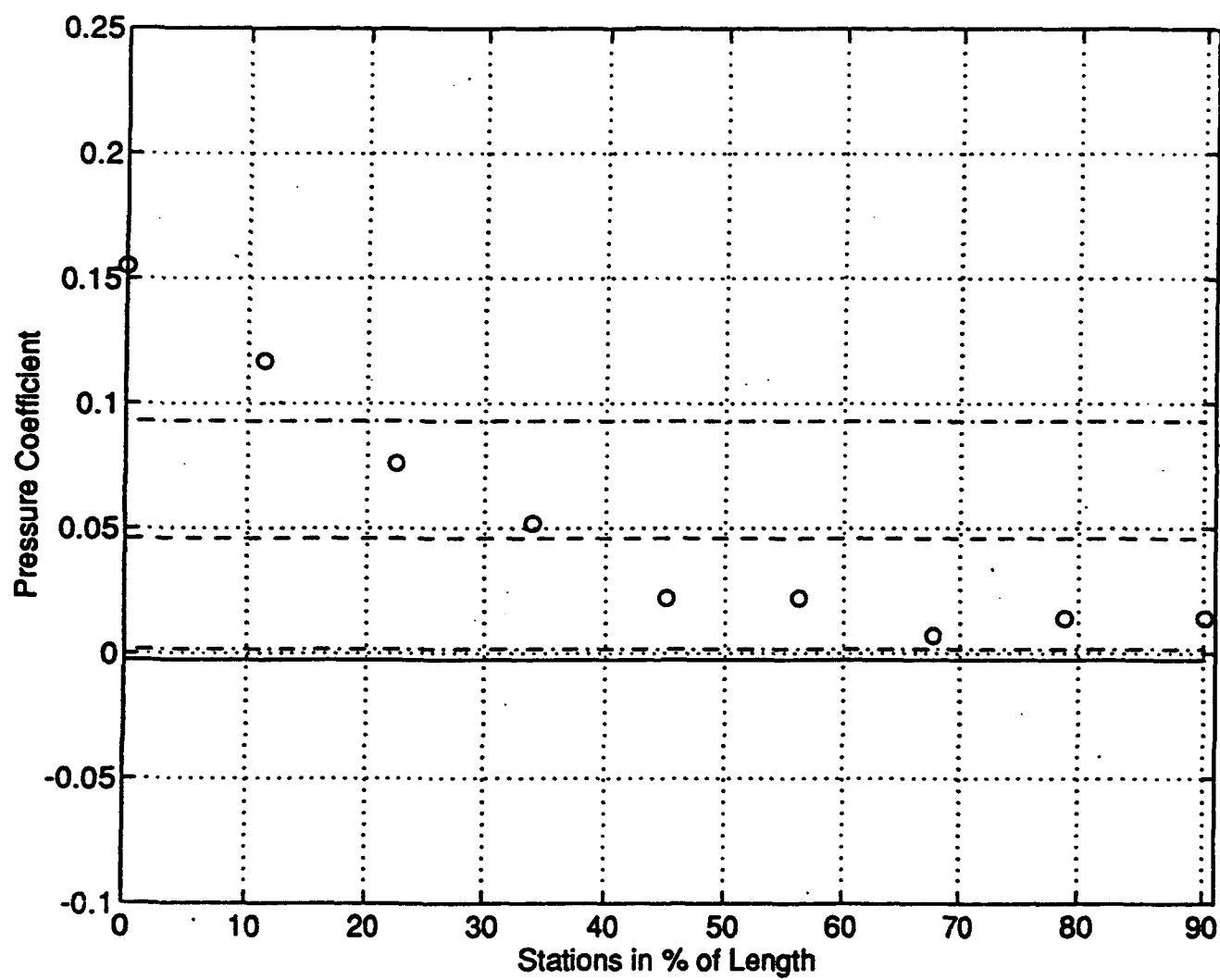


Fig. 5.12 Pressure Coefficient for Surface 5 of Case 1

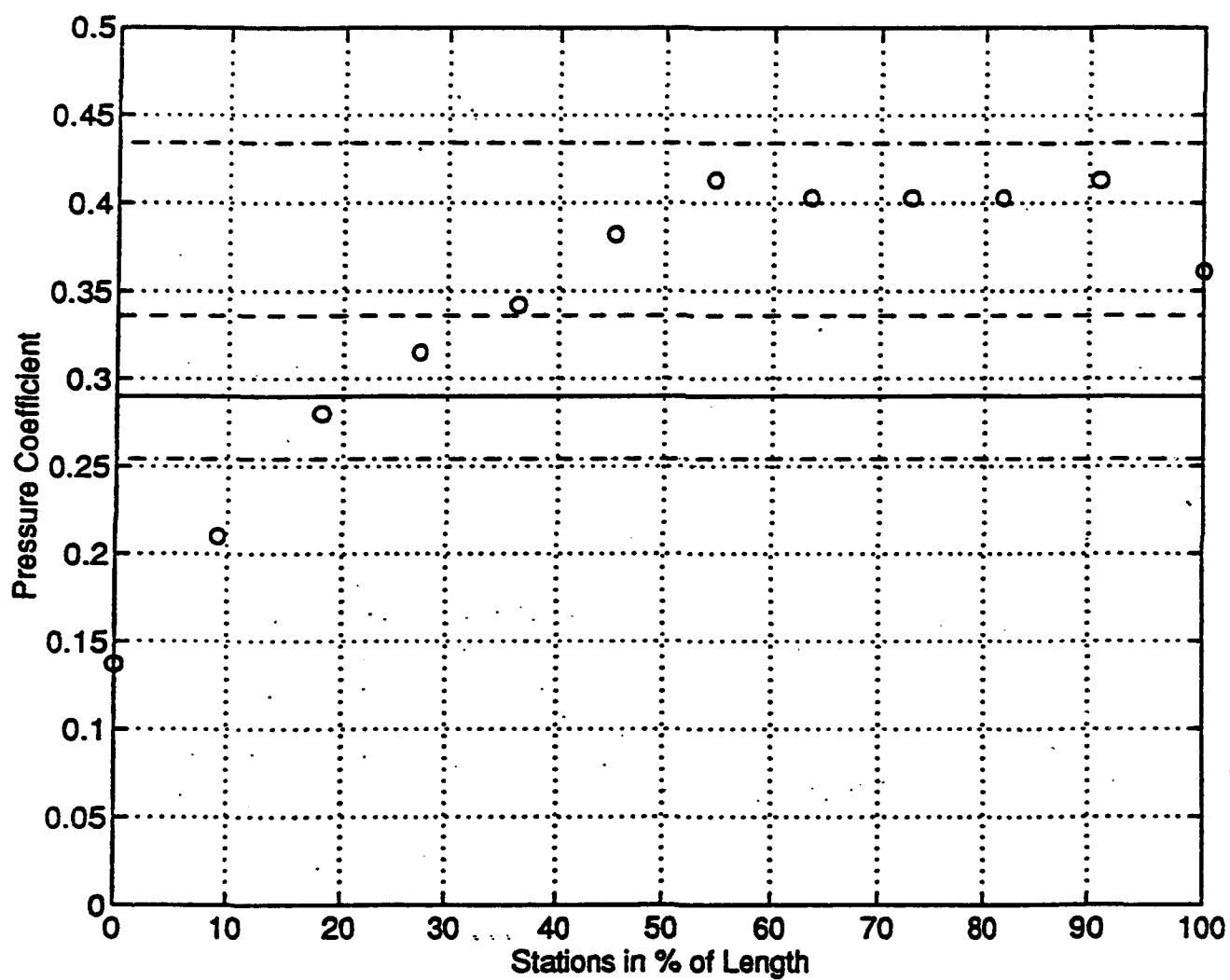


Fig. 5.13 Pressure Coefficient for Surface 2 of Case 2

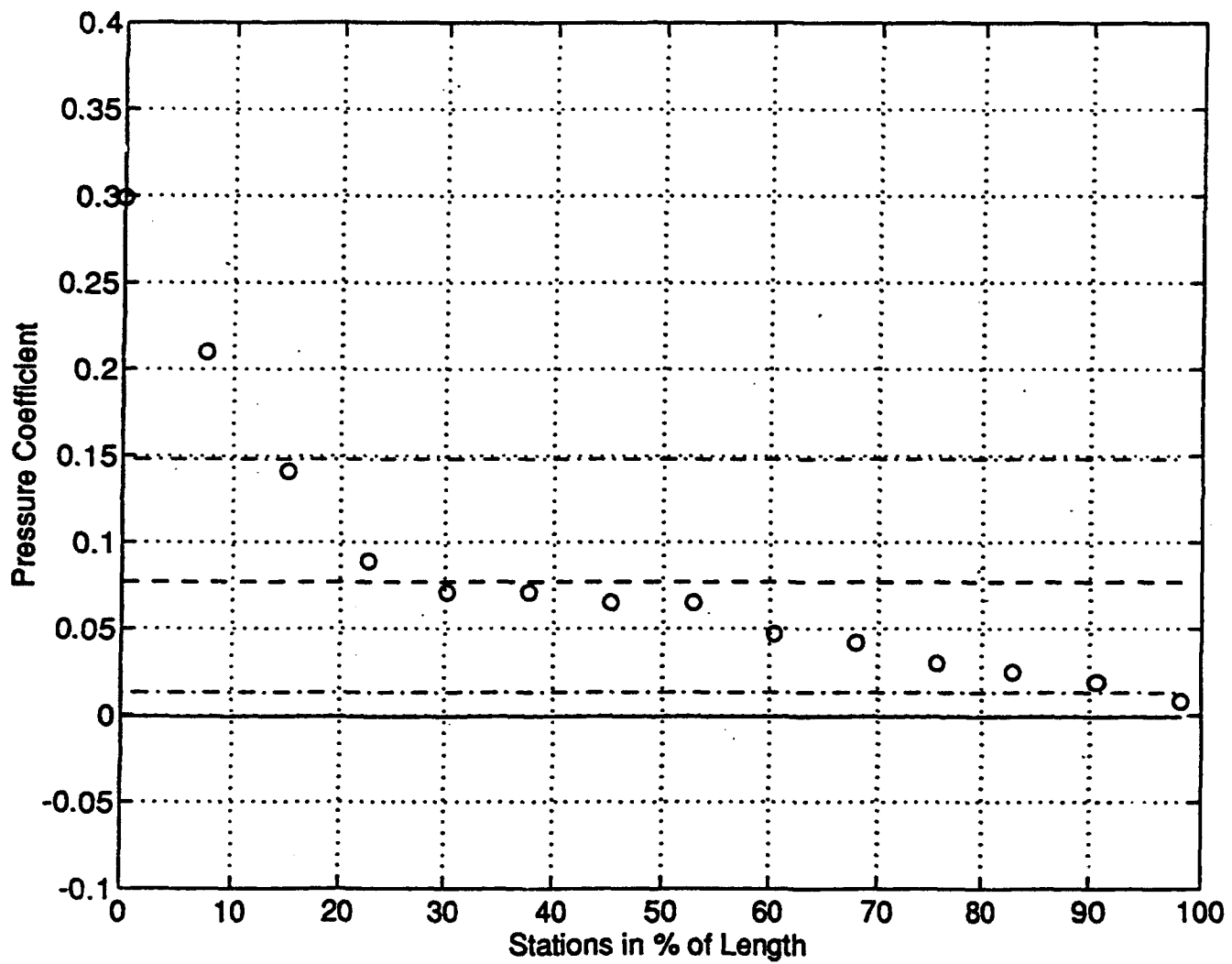


Fig. 5.14 Pressure Coefficient for Surface 3 of Case 2

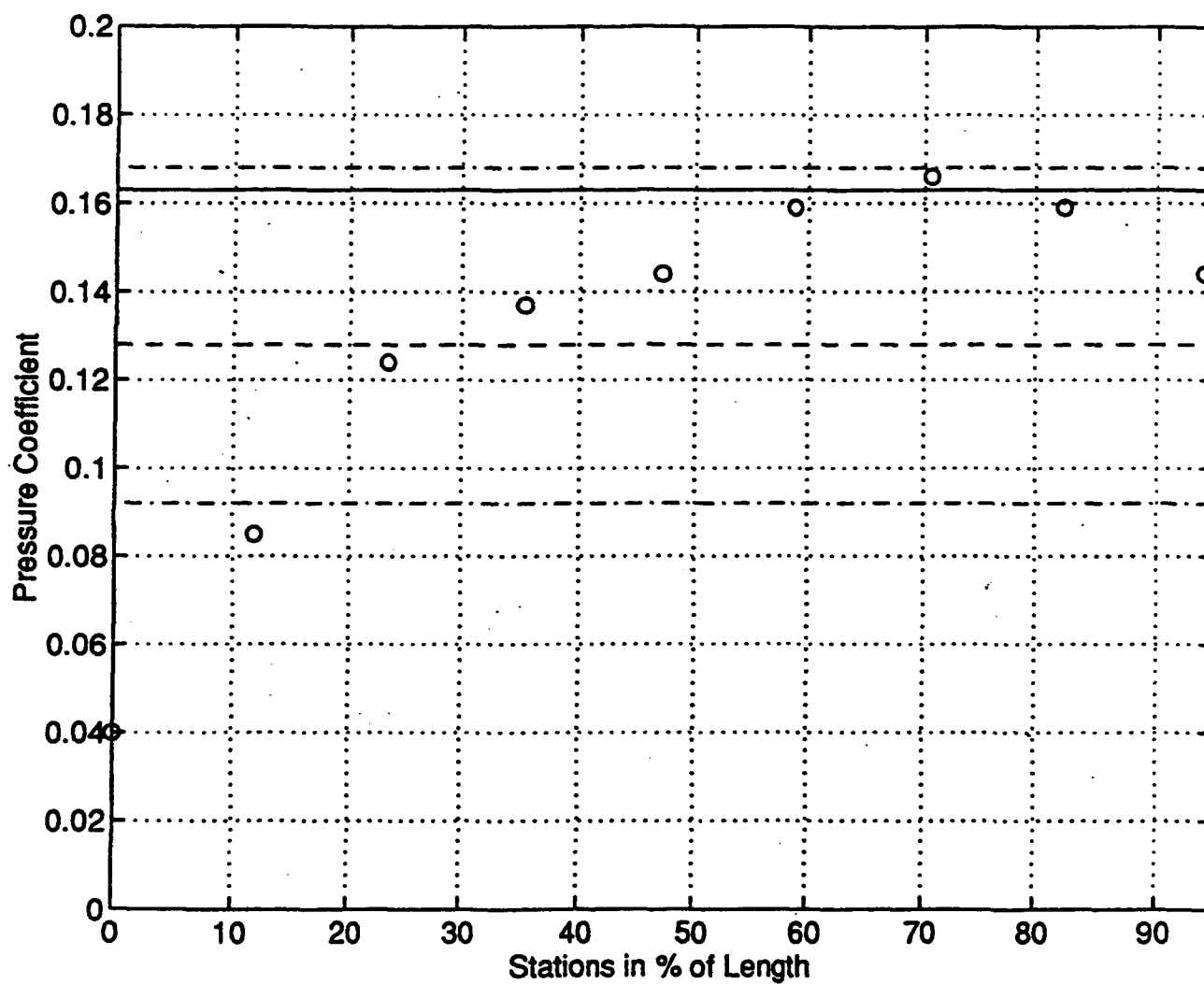


Fig. 5.15 Pressure Coefficient for Surface 4 of Case 2

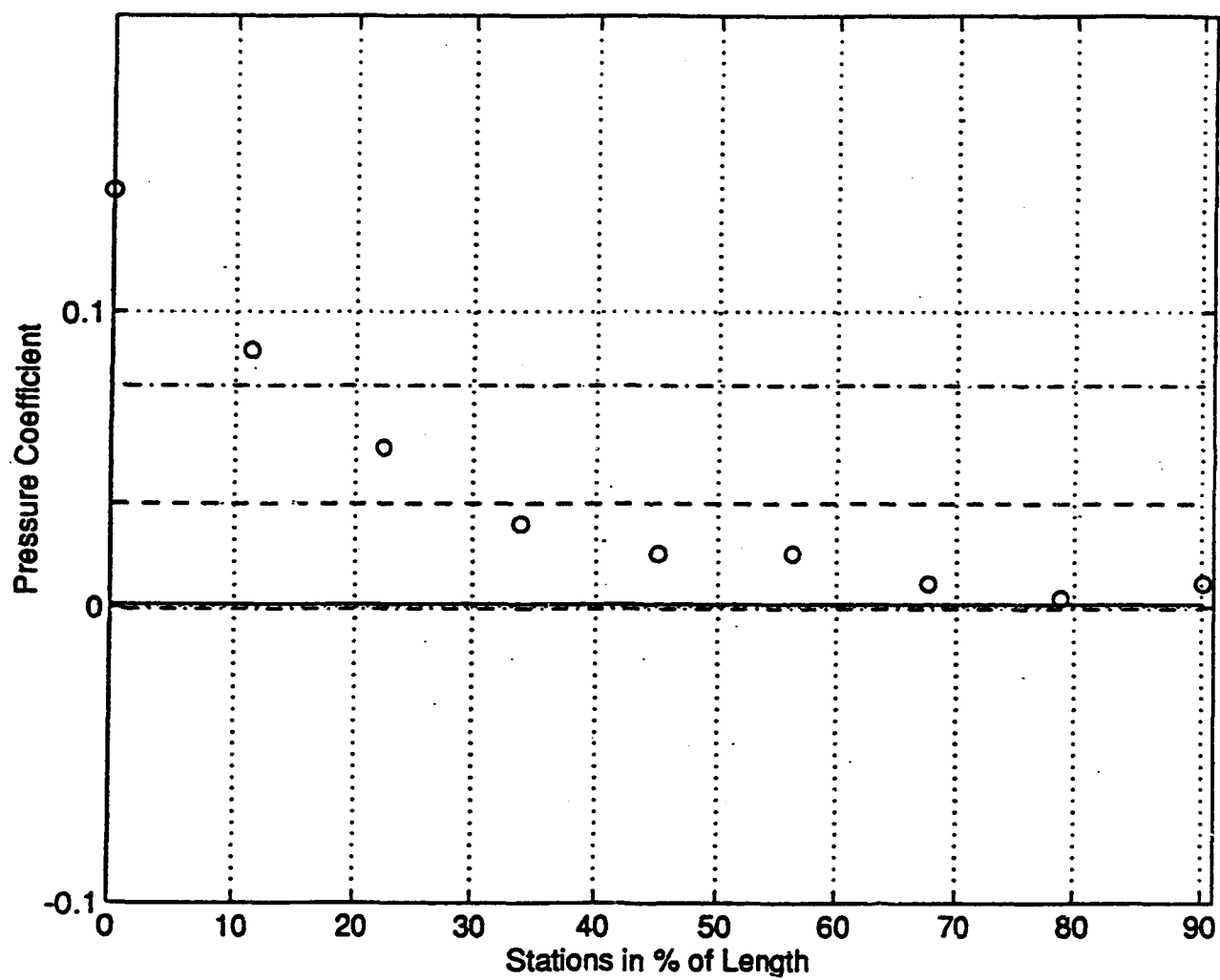


Fig. 5.16 Pressure Coefficient for Surface 5 of Case 2

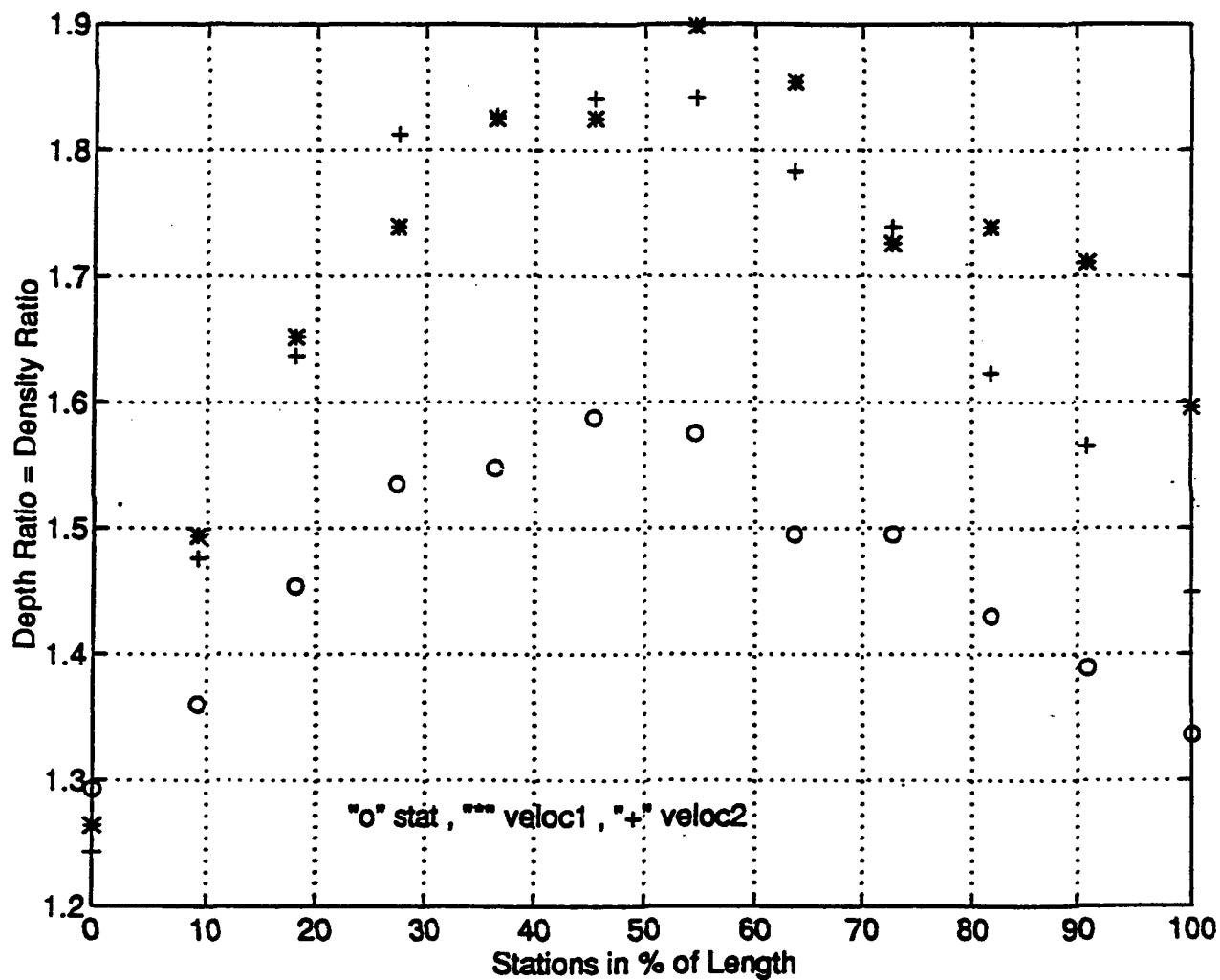


Fig. 5.17 A Comparison of Water Depth Ratio on Surface 2 for Different Motion Profiles. Position 1

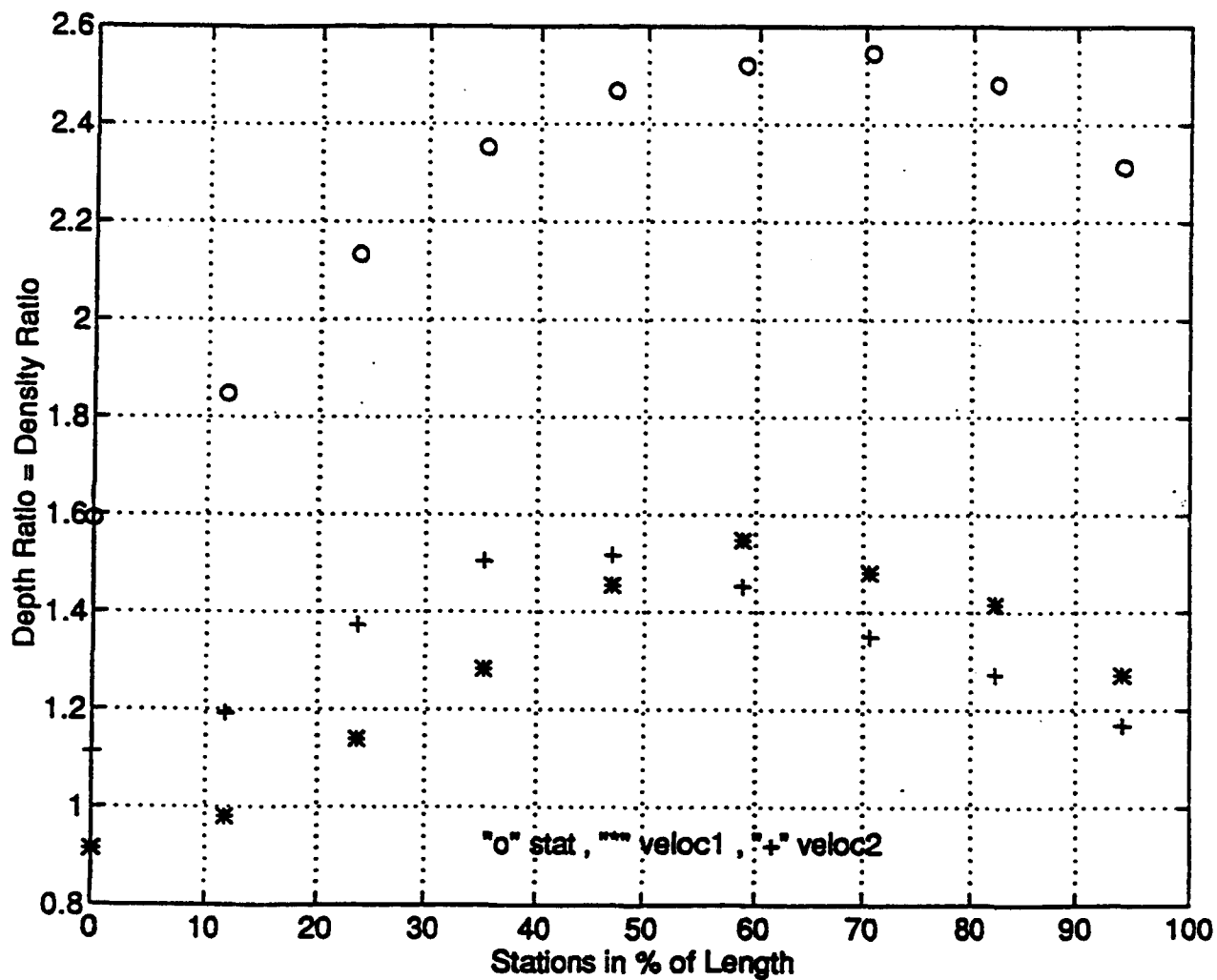


Fig. 5.18 A Comparison of Water Depth Ratio on Surface 4 for Different Motion Profiles. Position 1

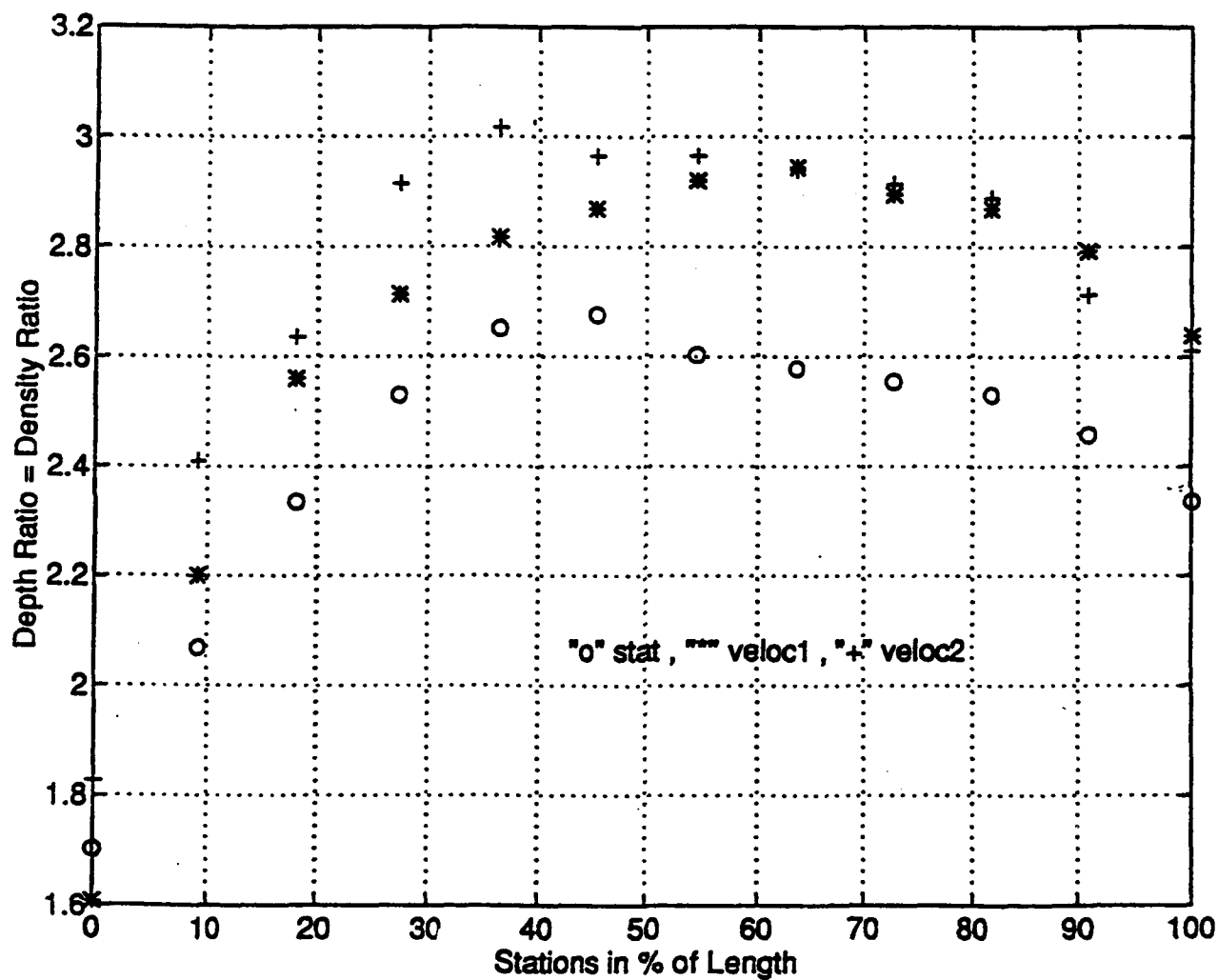


Fig. 5.19 A Comparison of Water Depth Ratio on Surface 2 for Different Motion Profiles. Position 2

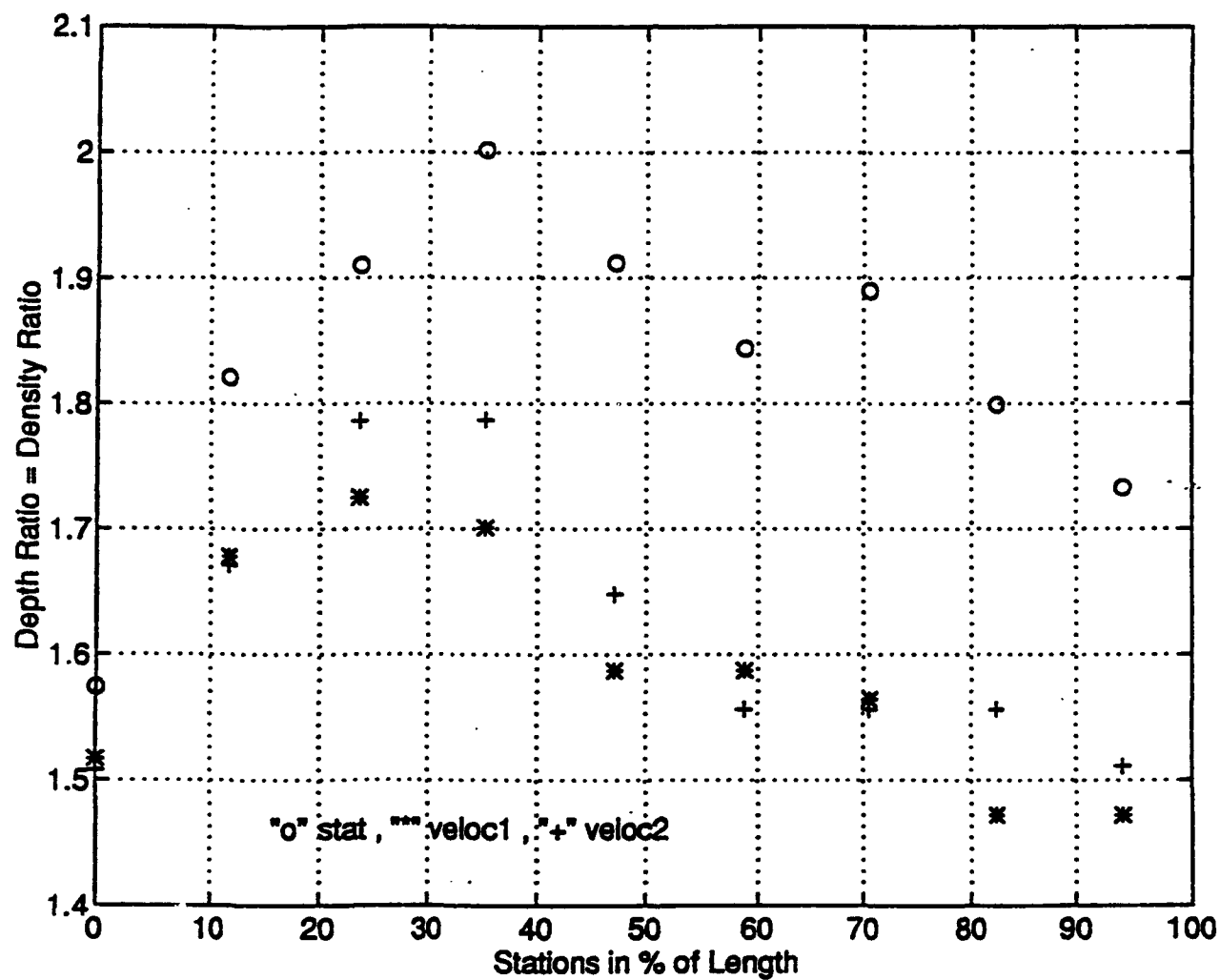


Fig. 5.20 A Comparison of Water Depth Ratio on Surface 4 for Different Motion Profiles. Position 2

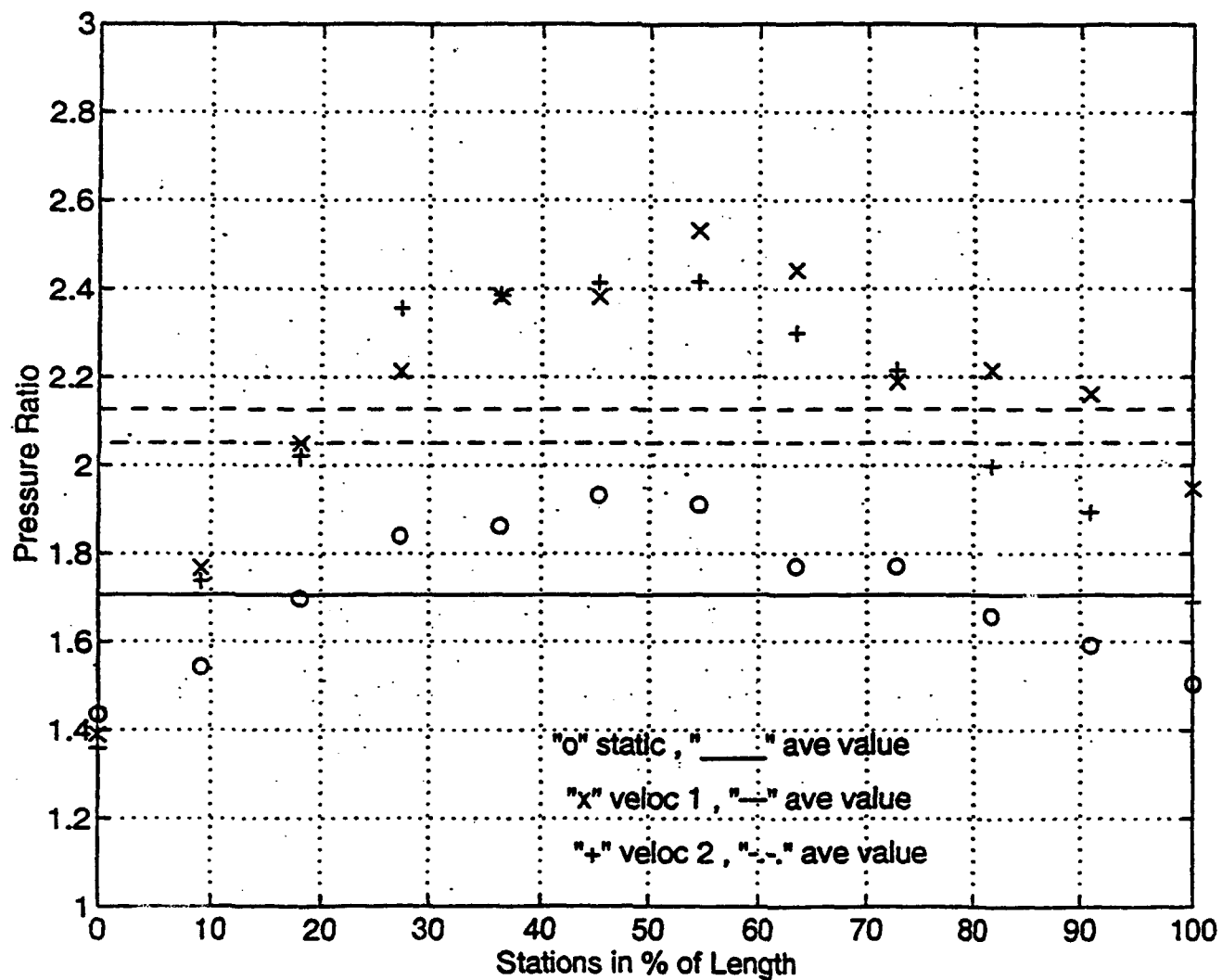


Fig. 5.21 A Comparison of Pressure Ratio on Surface 2 for Different Motion Profiles. Position 1

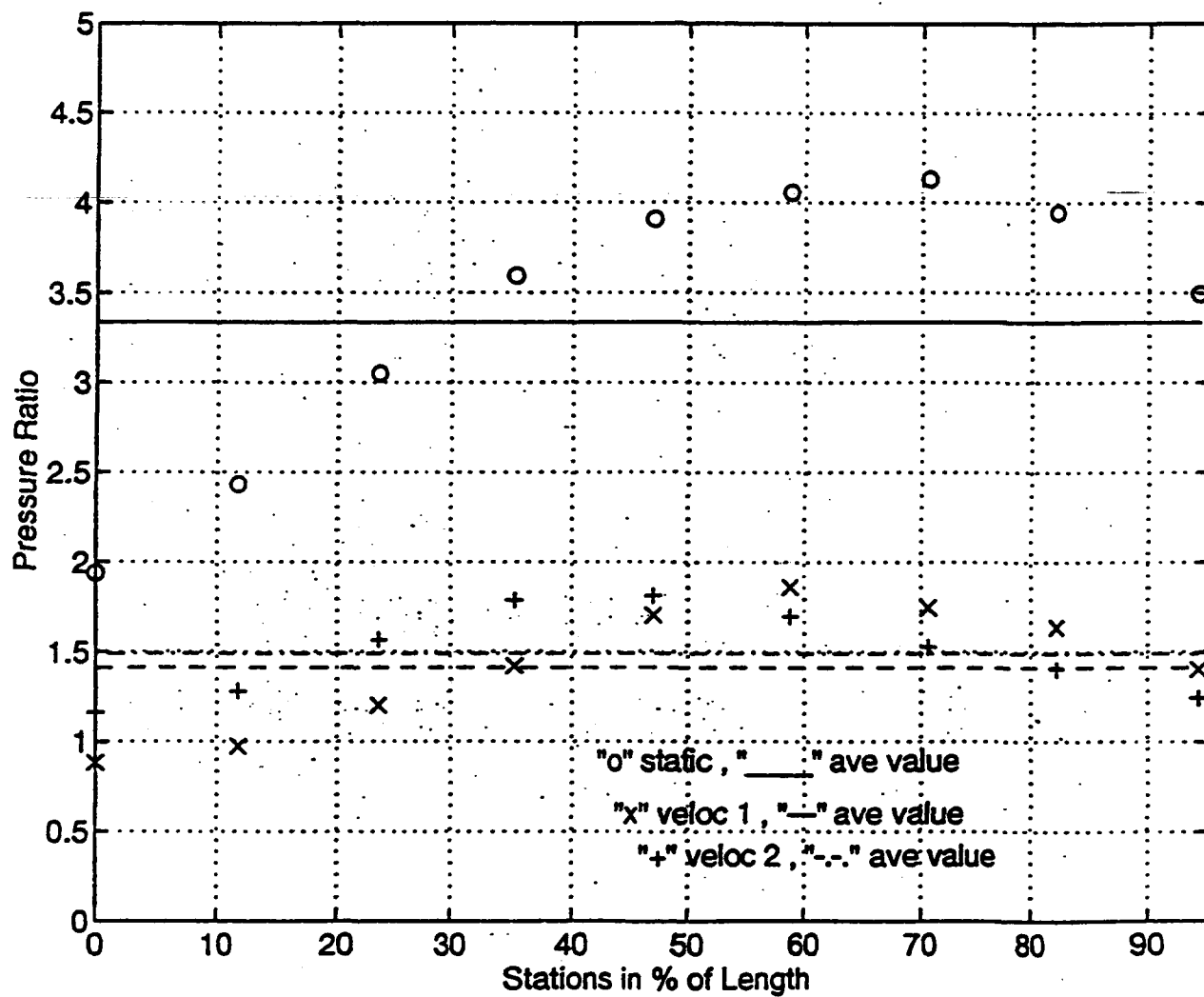


Fig. 5.22 A Comparison of Pressure Ratio on Surface 4 for Different Motion Profiles. Position 1

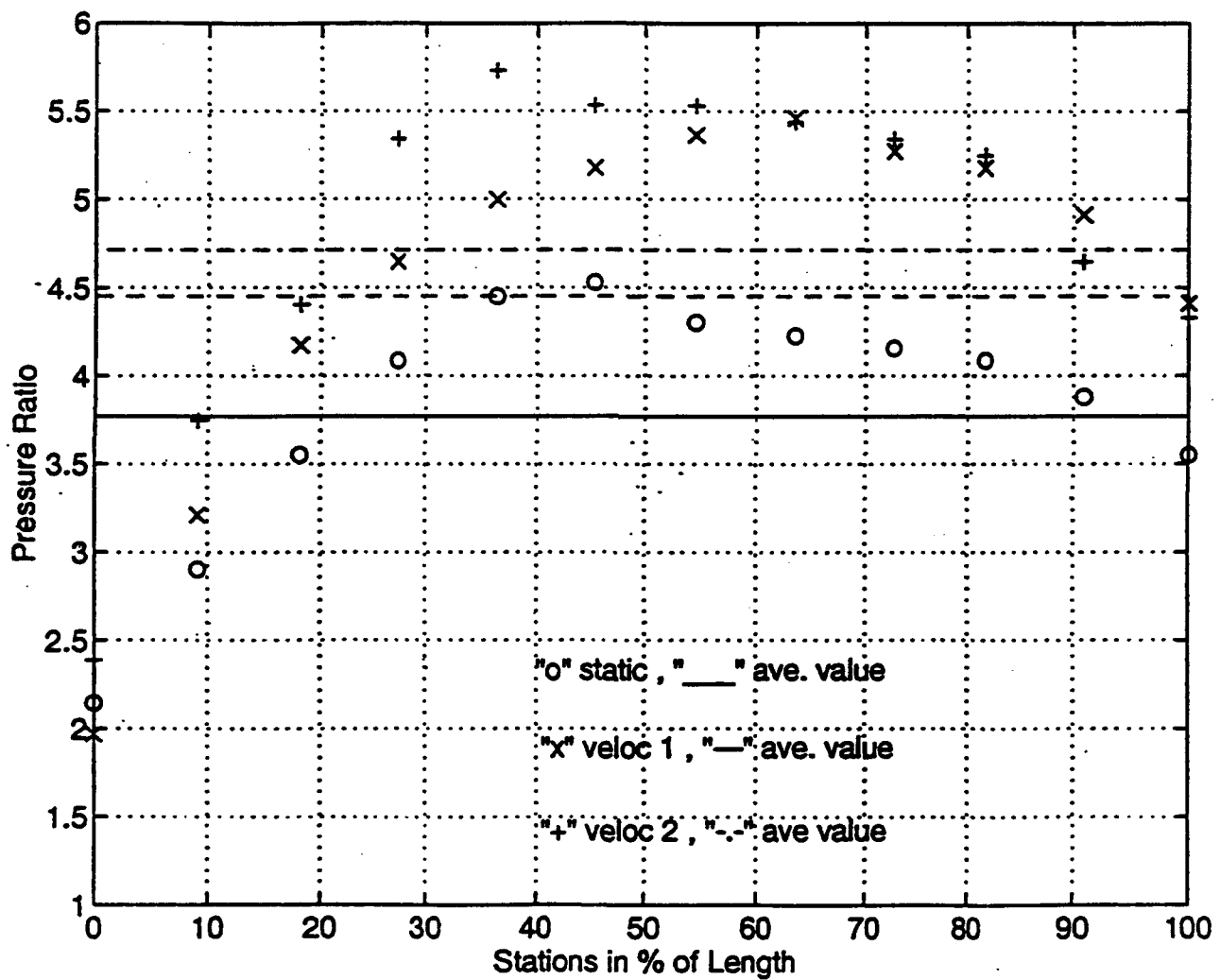


Fig. 5.23 A Comparison of Pressure Ratio on Surface 2 for Different Motion Profiles. Position 2

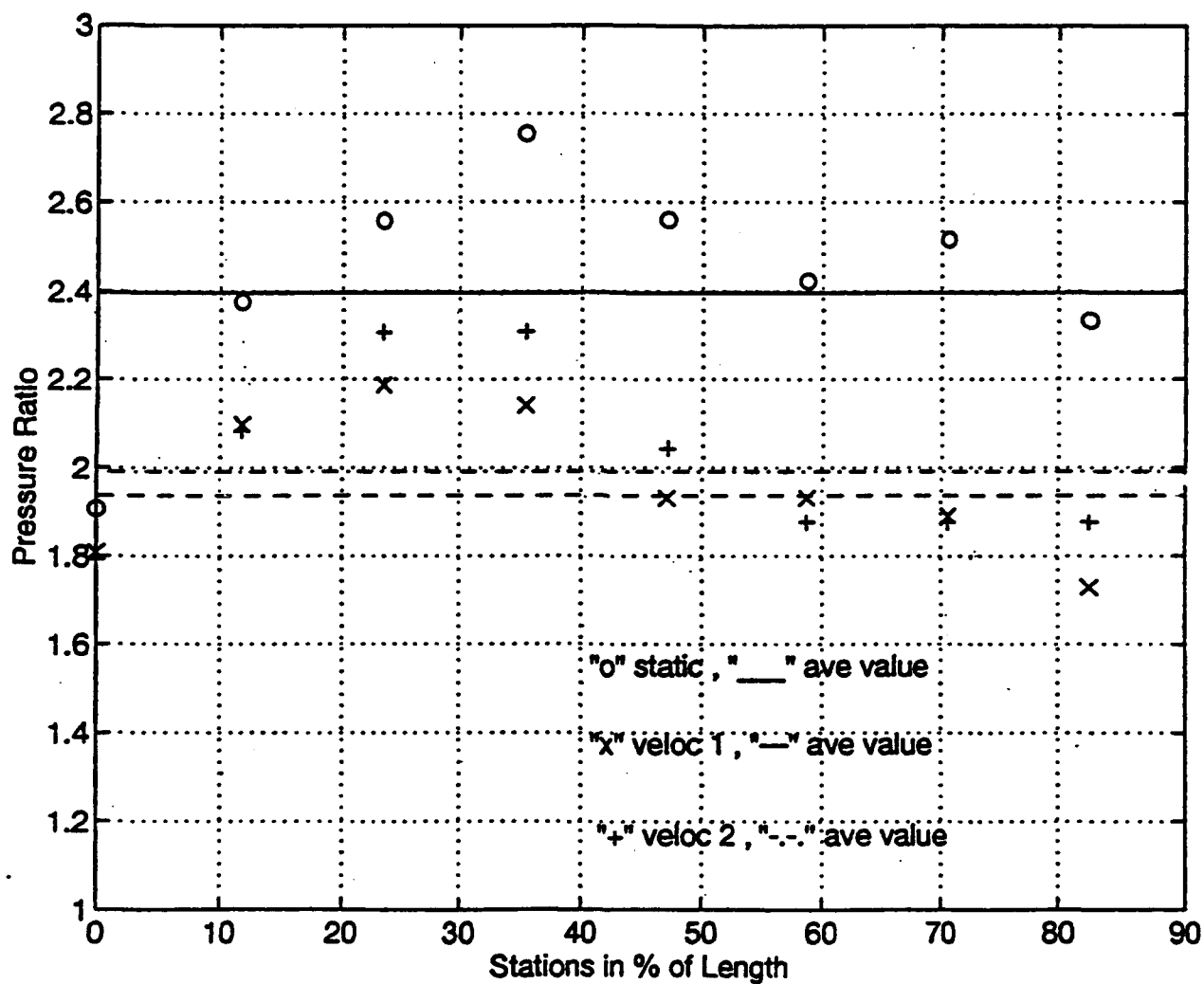


Fig. 5.24 A Comparison of Pressure Ratio on Surface 4 for Different Motion Profiles. Position 2

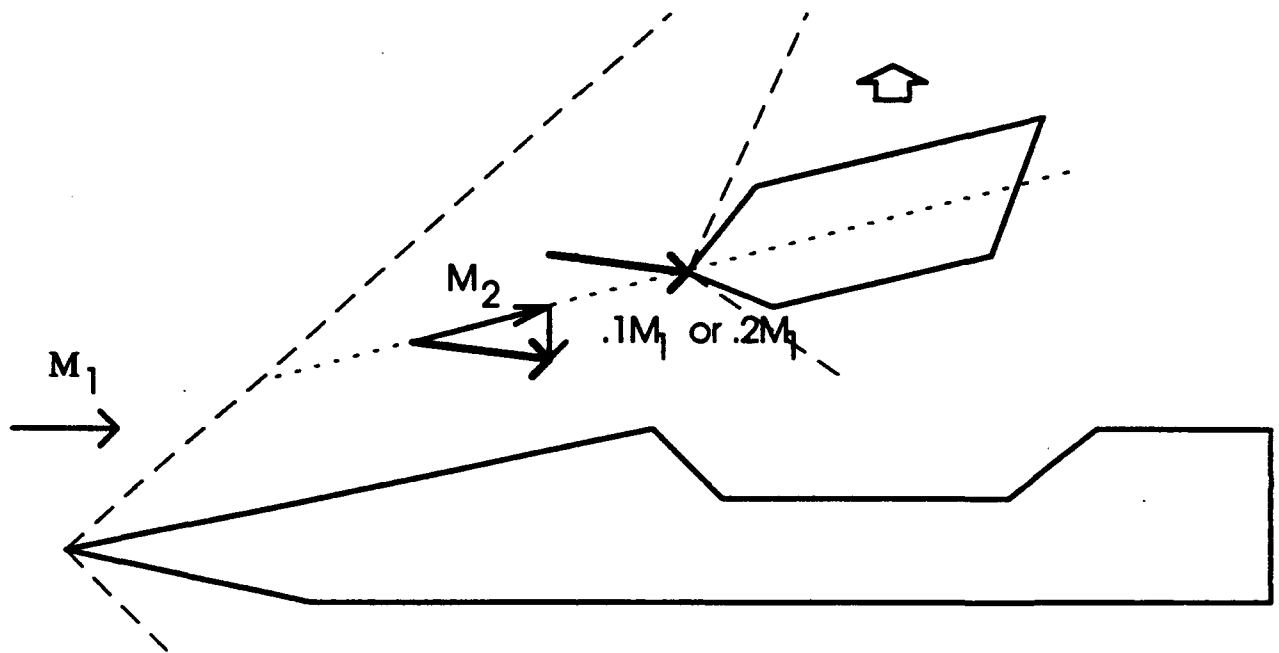
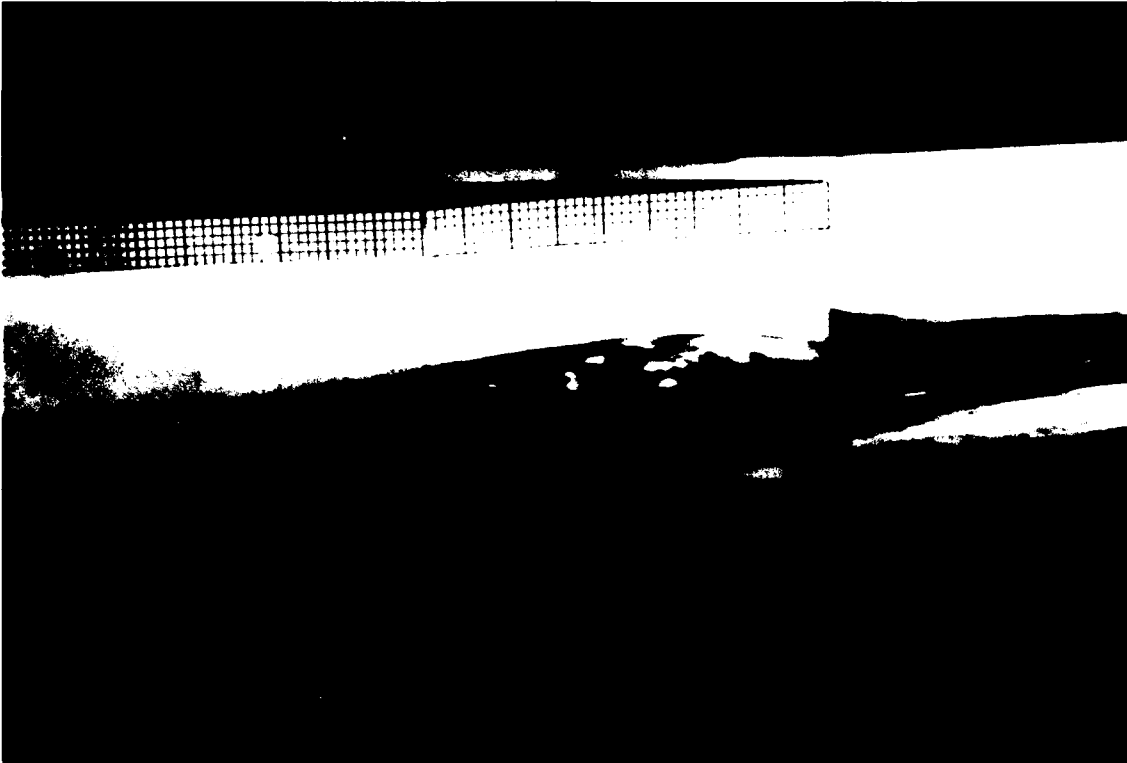
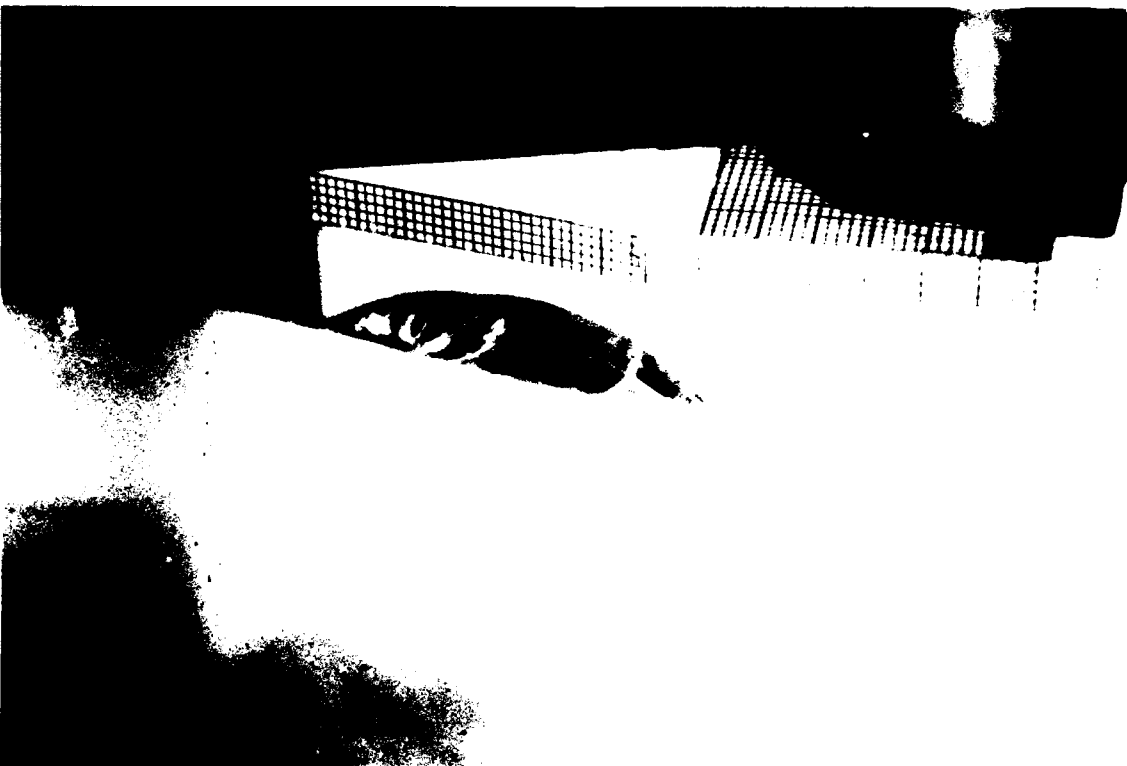


Fig.5.25 Analysis of Flow For Capsule\Fuselage System

SURFACE 2 (RIGHT SIDE)



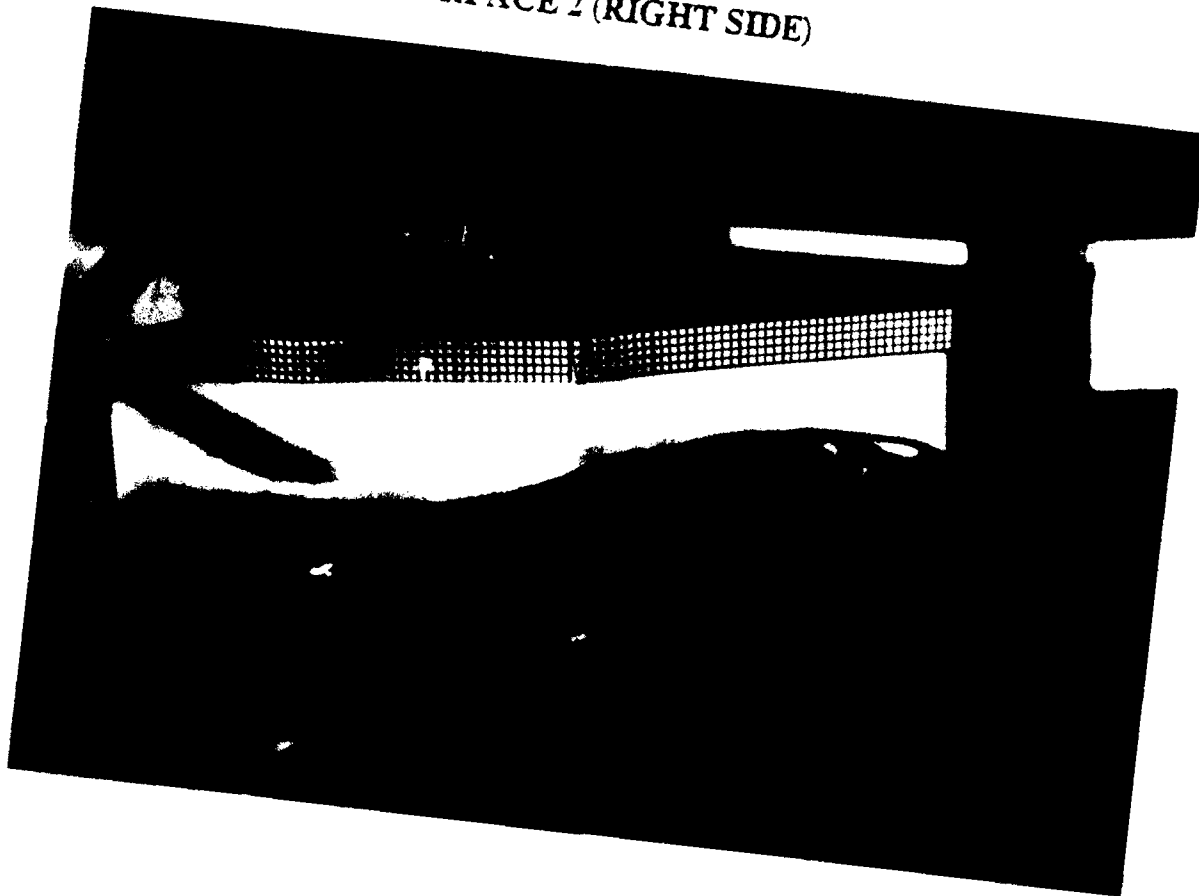
SURFACE 4 (LEFT SIDE)



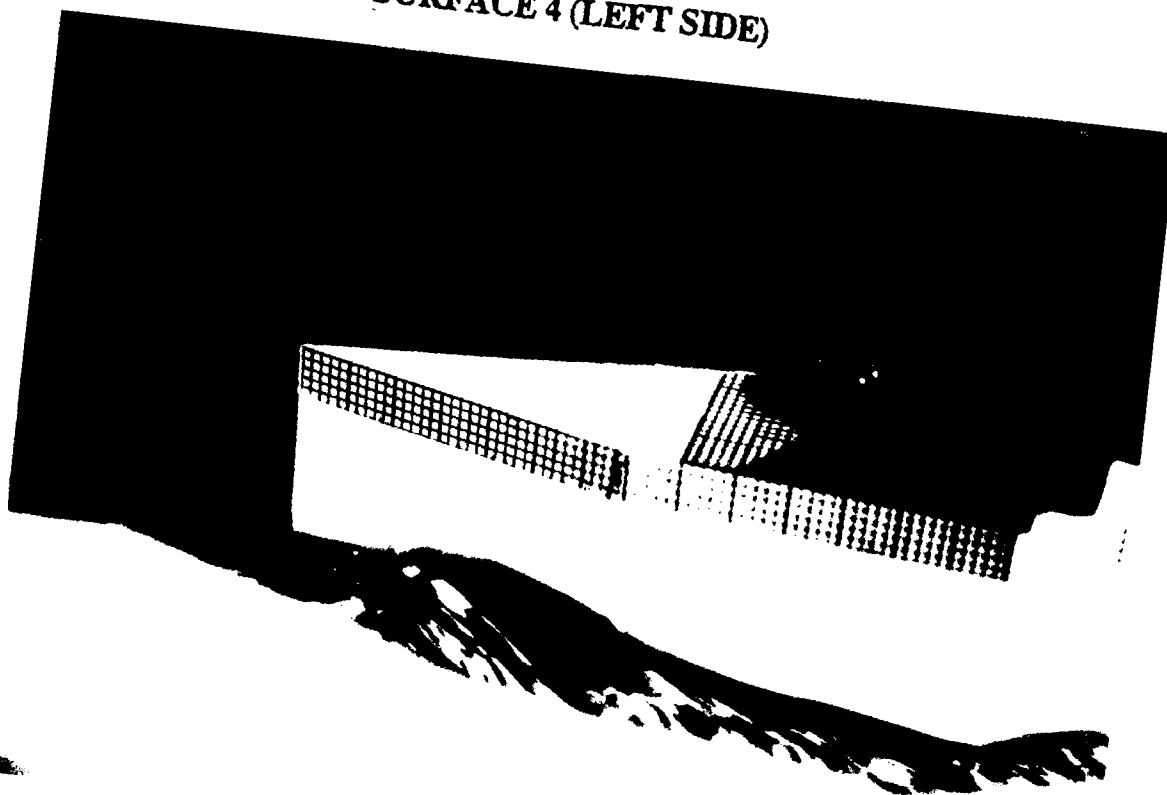
POSITION 1

VELOCITY 1

SURFACE 2 (RIGHT SIDE)



SURFACE 4 (LEFT SIDE)



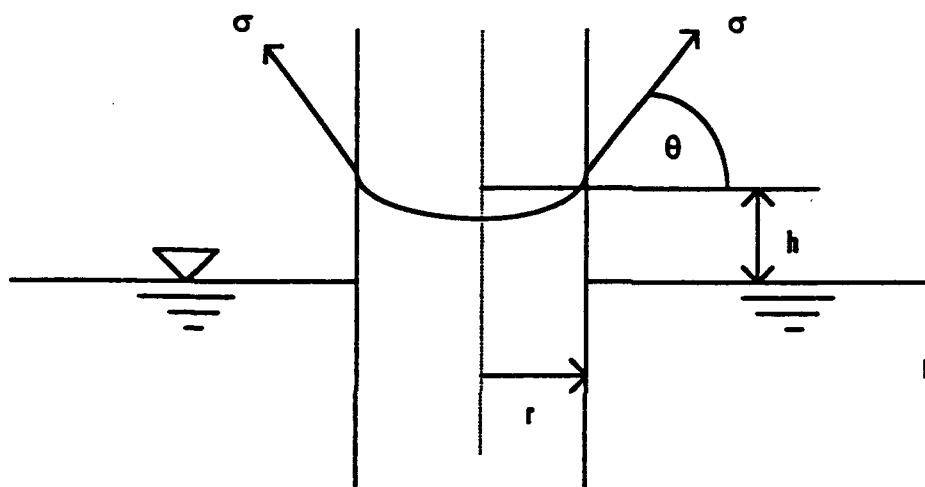


Fig. B.1 Capillary Rise in a Tube

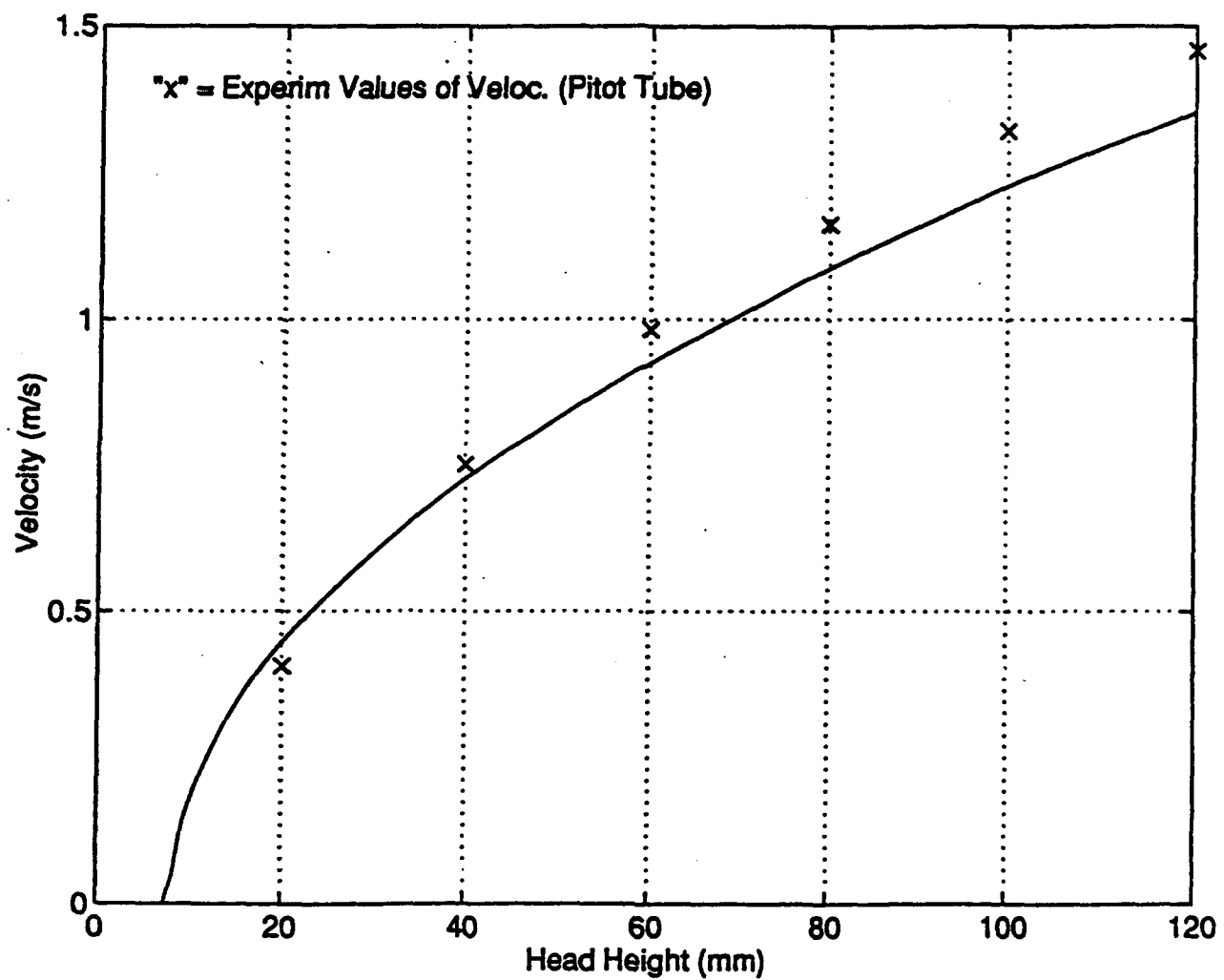


Fig. B.2 Velocity Measurements Using Pitot Tube as Compared to the Velocity from the Energy Equation

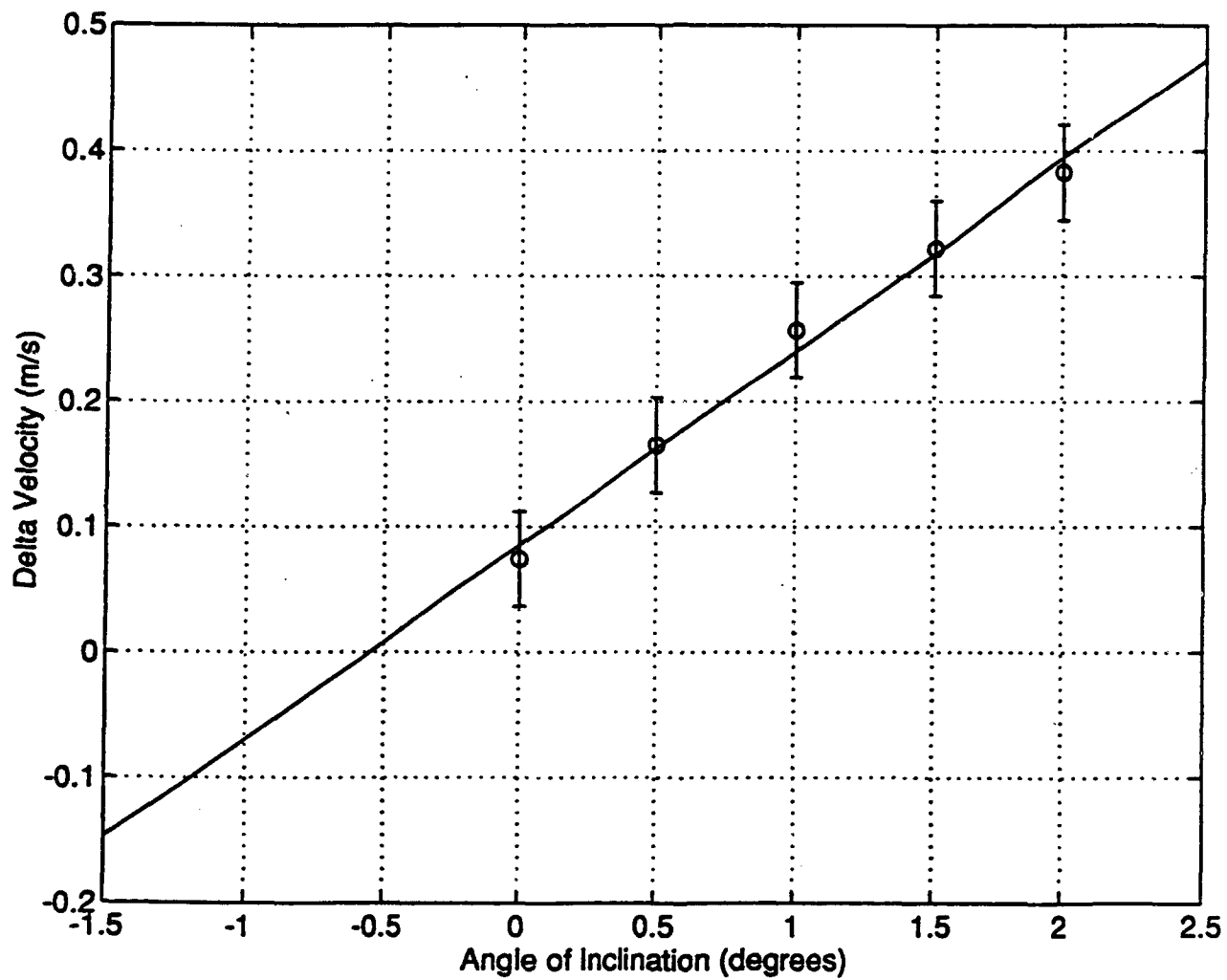


Fig. B.3 **Velocity Differential vs Angle of Inclination of Table.**
Head Height of 20 mm

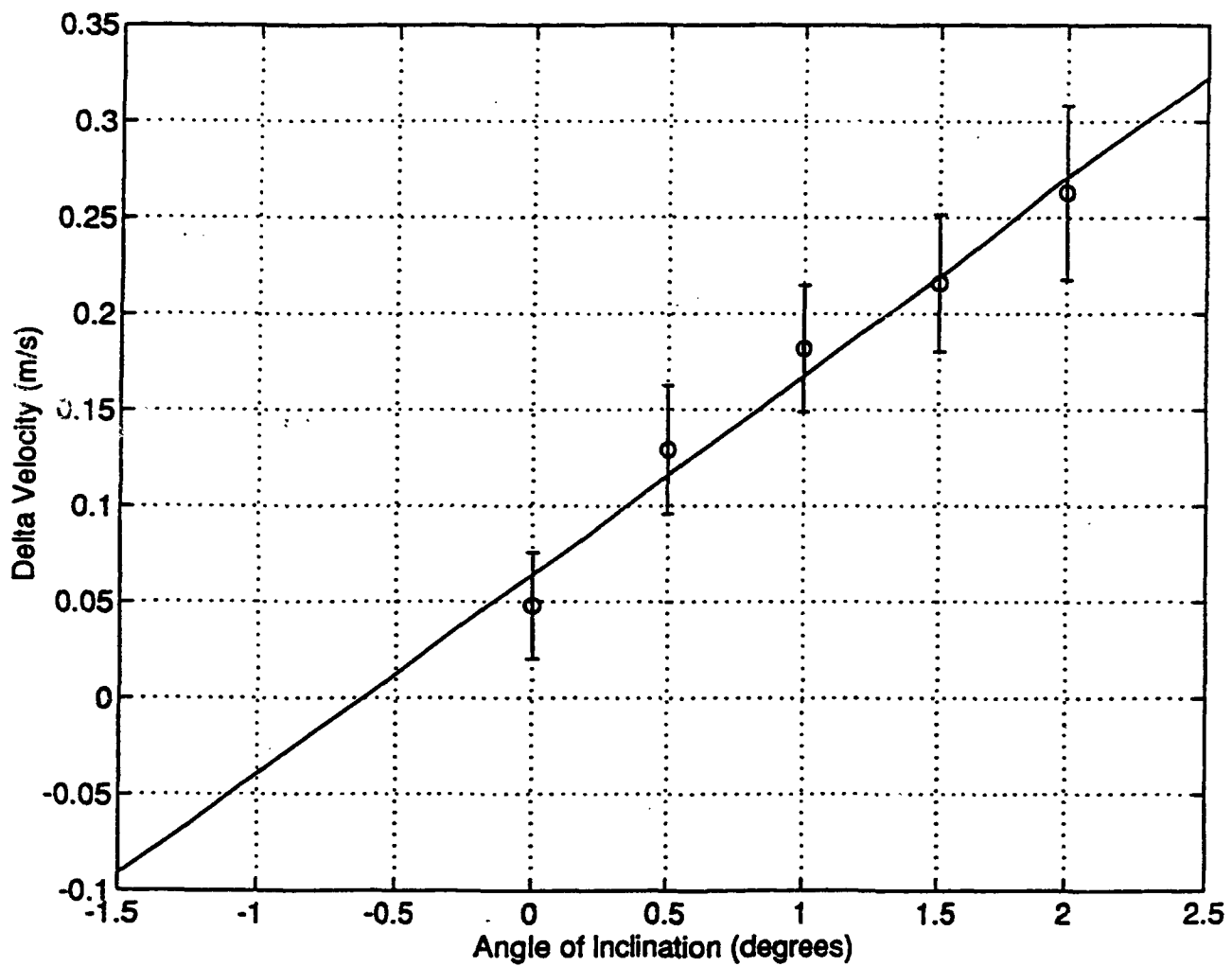


Fig. B.4 Velocity Differential vs Angle of Inclination of Table.
Head Height of 40 mm

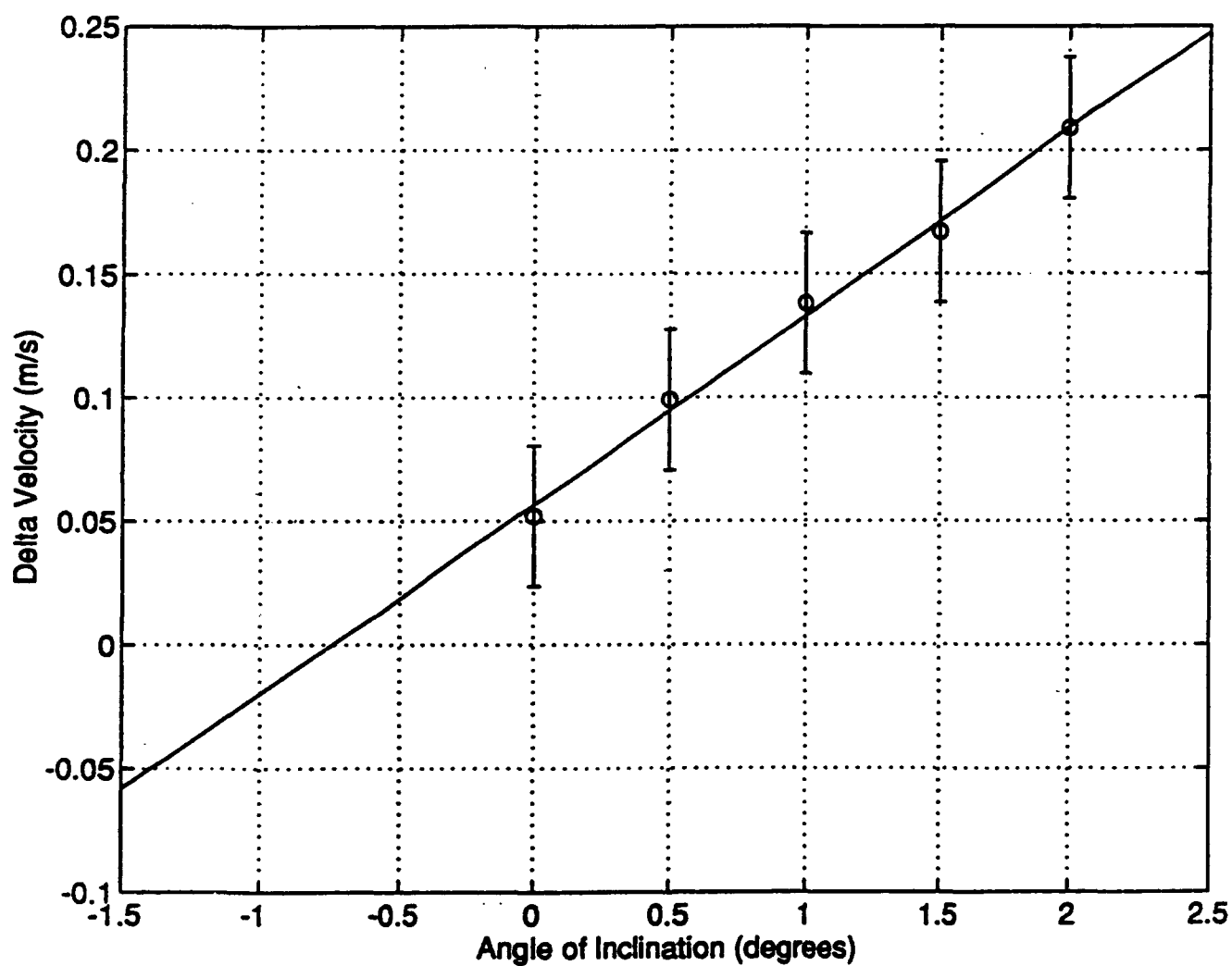


Fig. B.5 Velocity Differential vs Angle of Inclination of Table.
Head Height of 50 mm

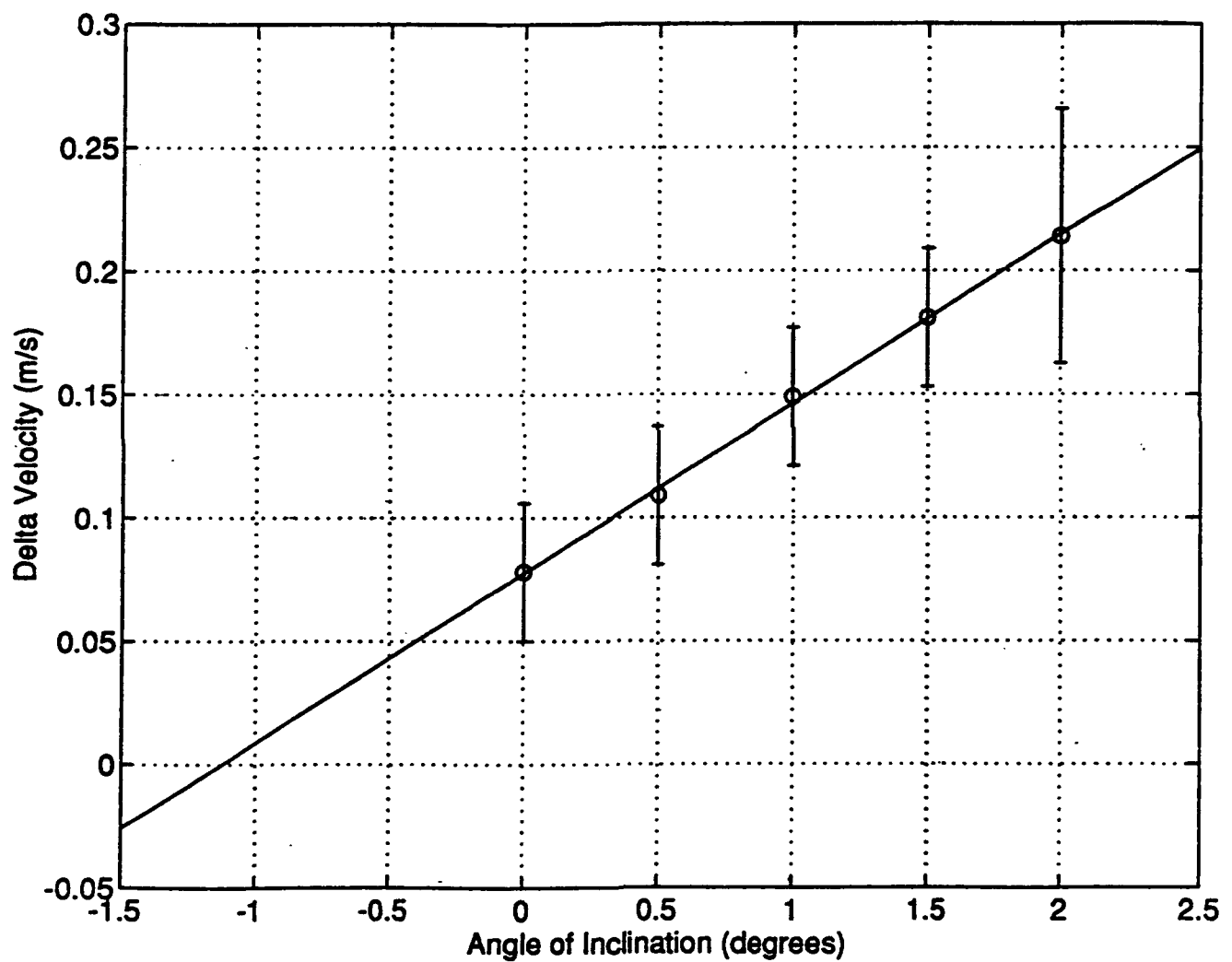


Fig. B.6 **Velocity Differential vs Angle of Inclination of Table.**
Head Height of 60 mm

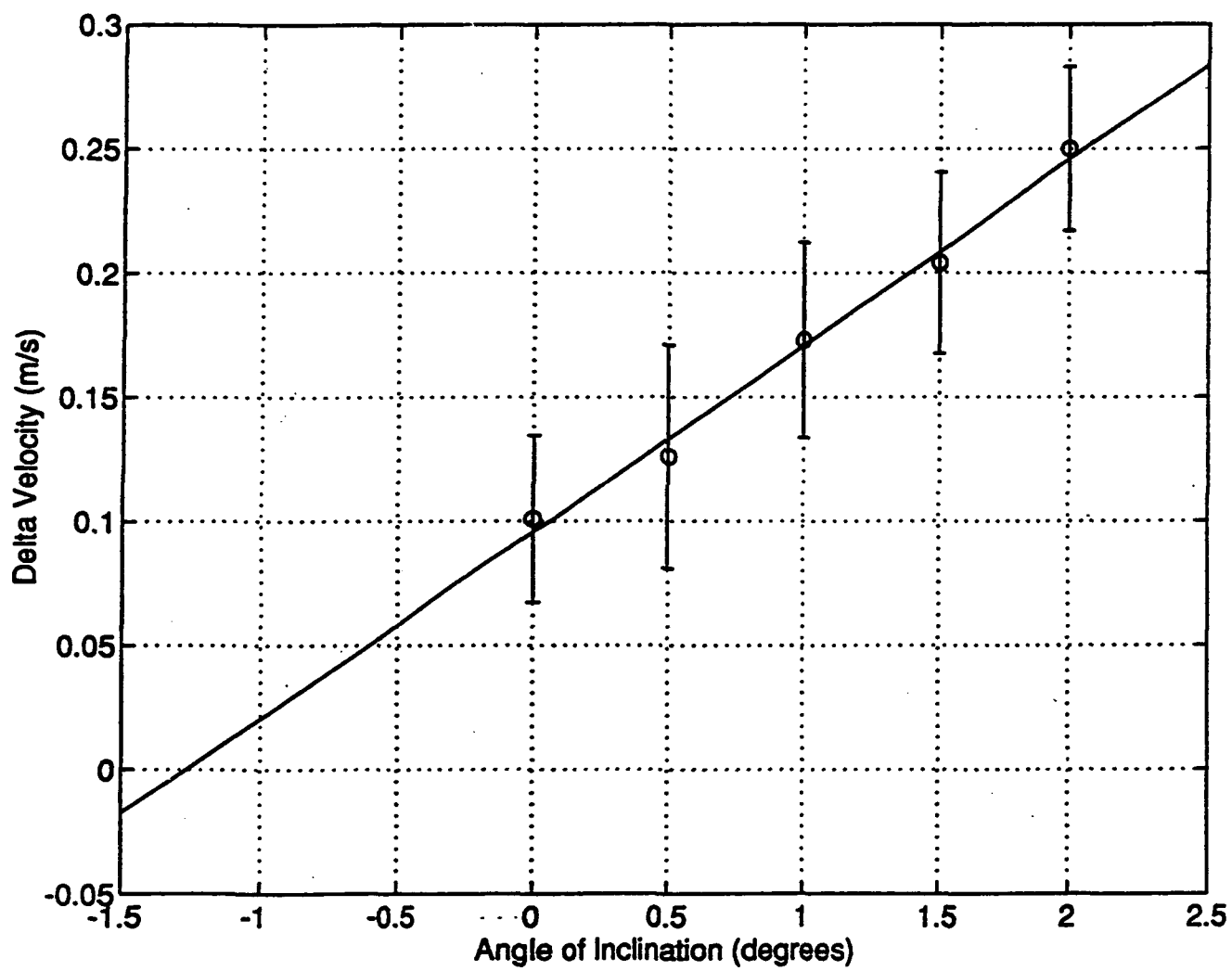
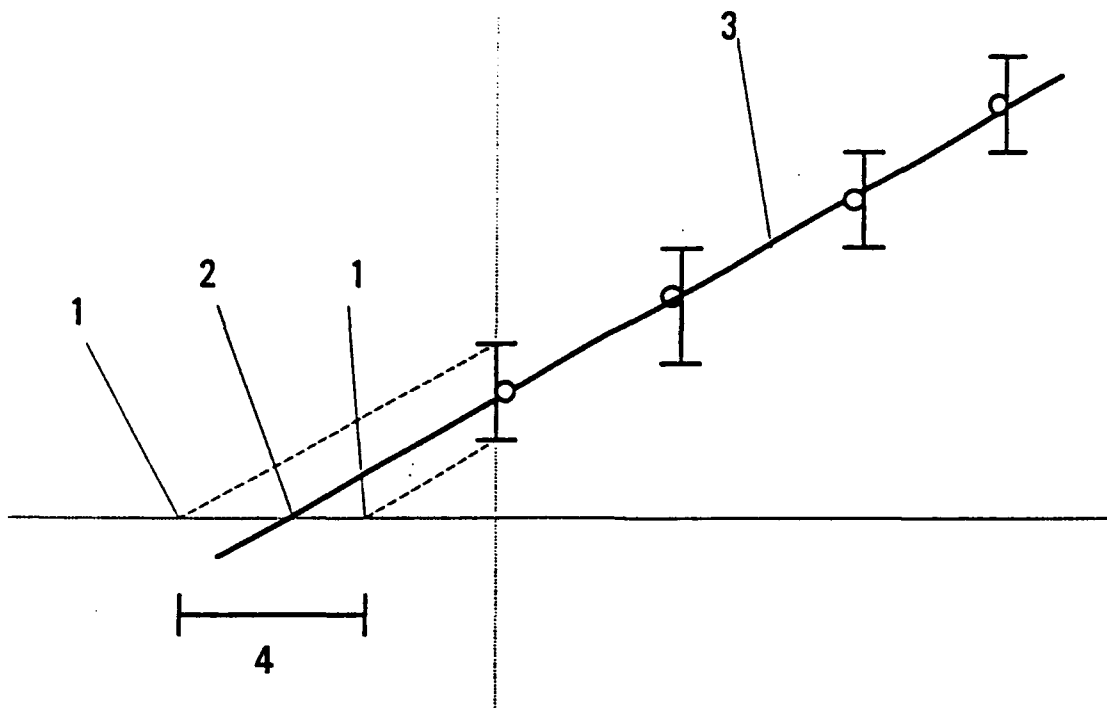


Fig. B.7 **Velocity Differential vs Angle of Inclination of Table.**
Head Height of 80 mm



ABSISSA: ANGLE OF INCLINATION OF TABLE

ORDINATE: DELTA VELOCITY BETWEEN .1 M AND .45 M

NOTE: NEGATIVE ANGLES INDICATE COUNTERCLOCKWISE ANGLES OF INCLINATION FOR THE TABLE

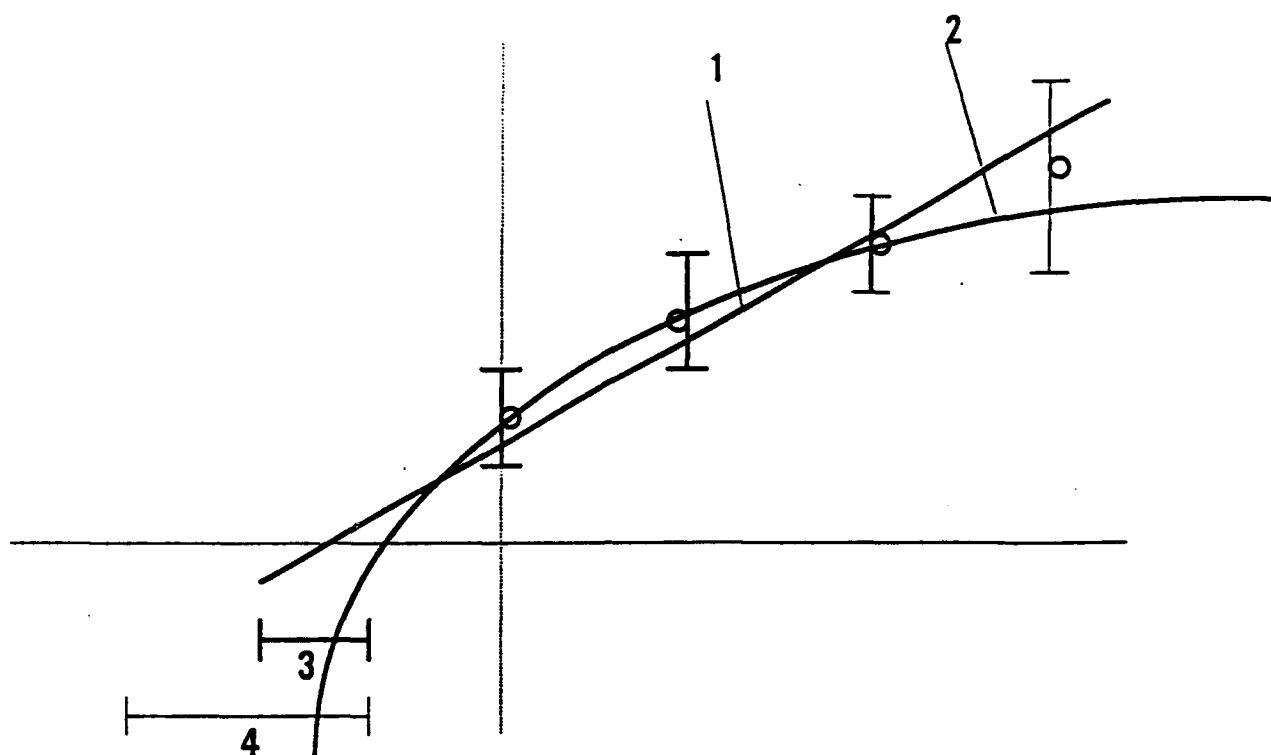
1 PROJECTION ON ABSISSA OF ERRORBARS AT ZERO DEGREE INCLINATION

2 INTERSECTION OF LINEAR FIT WITH ABSISSA TO GET POINT OF ZERO DELTA VELOCITY.

3 LINEAR FIT OF EXPERIMENTAL POINTS

4 ERRORBAND ON ABSISSA

B.8 (a) Method of Determination of the Uncertainty in the Velocity
Differential for the Reference Head Heights Between
50 and 80 mm



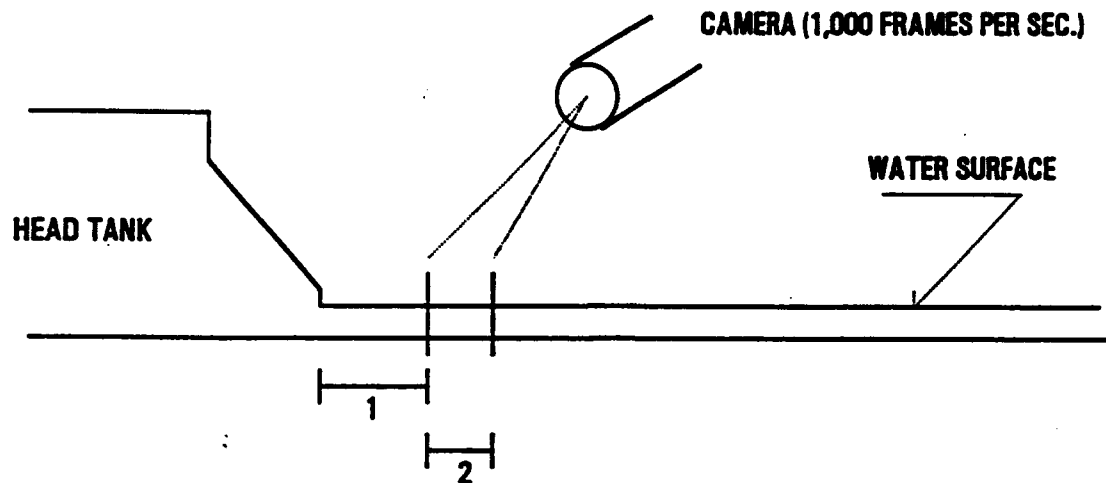
1 LINEAR FIT FOR THE DATA

2 QUADRATIC FIT FOR THE DATA

3 DIFFERENCE IN POINTS OF INTERSECTION BETWEEN LINEAR AND QUADRATIC FIT CURVES

4 ERROR BAND OF POINT OF ZERO DELTA VELOCITY IS TWICE THE DIFFERENCE GIVEN BY 3

**B.8 (b) Method of Determination of the Uncertainty in the Velocity
Differential for the Reference Head Heights Between
20 and 40 mm**



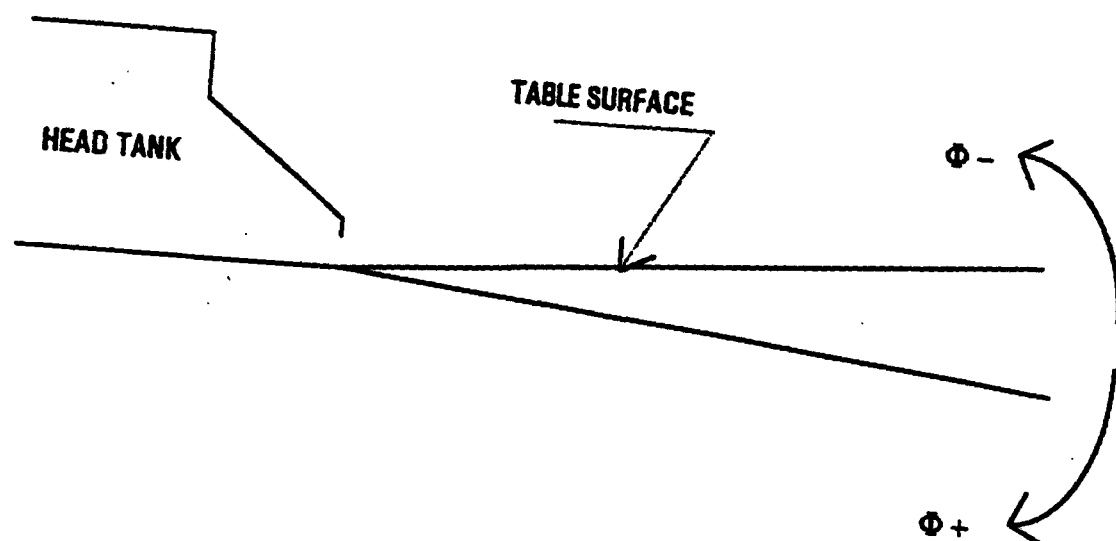
1 0.1 M DOWNSTREAM FROM NOZZLE

2 0.05 M BETWEEN POINTS IN WATER

VELOCITY = Δ DIST / TIME

TIME IS OBTAINED FROM CAMERA WITH 0.002 SEC ERROR

B.9 Determination of Velocity using High Speed Camera



B.10 Positive and Negative Angles of Inclination for Table

APPENDIX B

Table 5.3 Experimental Values of the Ratio of Different Flow Parameters

Across a "Compression Shock Wave"

(Hydraulic Jump)

Surface 2
Case 1

Station (in % of Length)	$\frac{h_j}{h_i} \equiv \frac{\rho_j}{\rho_i}$	$\frac{p_j}{p_i}$ (Eqn. 2.5.1)	Pressure Coefficient (Eqn. 2.5.7)
0	1.349	1.525	0.078
9.1	1.75	2.235	0.184
18.2	2.082	2.933	0.287
27.3	2.215	3.247	0.334
36.4	2.315	3.498	0.371
45.5	2.382	3.674	0.397
54.5	2.415	3.763	0.411
63.6	2.415	3.763	0.411
72.7	2.382	3.674	0.397
81.8	2.382	3.674	0.397
90.9	2.315	3.498	0.371
100.0	2.249	3.331	0.346
	$\bar{x} = 2.119$	3.018	0.300
	± 0.287	3.738	0.407
		2.397	0.208

			$Cp_{THEO} = 0.325$
--	--	--	---------------------

**Table 5.4 Experimental Values of the Ratio of Different Flow Parameters
Across a "Compression Shock Wave"
(Hydraulic Jump)**

Surface 4 Case 1

Station (in % of Length)	$\frac{h_j}{h_i} \equiv \frac{\rho_j}{\rho_i}$	$\frac{p_j}{p_i}$ (Eqn. 2.5.1)	Pressure Coefficient (Eqn. 2.5.7)
0	1.444	1.682	0.101
11.8	1.613	1.978	0.145
23.5	1.75	2.235	0.184
35.3	1.784	2.302	0.194
47.1	1.784	2.302	0.194
58.8	1.784	2.302	0.194
70.6	1.75	2.235	0.184
82.4	1.75	2.235	0.184
94.1	1.613	1.978	0.145
	$\bar{x} = 1.691$	2.123	0.167
	± 0.116	2.347	0.200
		1.910	0.135
			$Cp_{THEO} = 0.188$

**Table 5.5. Experimental Values of the Ratio of Different Flow Parameters
Across a "Compression Shock Wave"
(Hydraulic Jump)**

Surface 2
Case 2

Station (in % of Length)	$\frac{h_j}{h_i} \equiv \frac{\rho_j}{\rho_i}$	$\frac{p_j}{p_i}$ (Eqn. 2.5.1)	Pressure Coefficient (Eqn. 2.5.7)
0	1.812	2.357	0.137
9.1	2.147	3.084	0.210
18.2	2.421	3.779	0.28
27.3	2.543	4.124	0.315
36.4	2.635	4.401	0.342
45.5	2.757	4.792	0.382
54.5	2.848	5.104	0.413
63.6	2.818	5.0	0.403
72.7	2.818	5.0	0.403
81.8	2.818	5.0	0.403
90.0	2.848	5.104	0.413
100.0	2.695	4.59	0.361
	$\bar{x} = 2.615$	4.340	0.336
	± 0.291	5.312	0.434
		3.521	0.254
			$Cp_{THEO} = 0.290$

**Table 5.6 Experimental Values of the Ratio of Different Flow Parameters
Across a "Compression Shock Wave"**

Surface 4
Case 2

Station (in % of Length)	$\frac{h_j}{h_i} \equiv \frac{\rho_j}{\rho_i}$	$\frac{p_j}{p_i}$ (Eqn. 2.5.1)	Pressure Coefficient (Eqn. 2.5.7)
0	1.267	1.395	0.040
11.8	1.54	1.848	0.085
23.5	1.746	2.228	0.124
35.3	1.815	2.363	0.137
47.1	1.849	2.432	0.144
58.8	1.919	2.576	0.159
70.6	1.953	2.648	0.166
82.4	1.919	2.576	0.159
94.1	1.849	2.432	0.144
	$\bar{x} = 1.771$	2.276	0.128
	± 0.193	2.672	0.168
		1.915	0.092
			$Cp_{THEO} = 0.163$

**Table 5.7 Experimental Values of the Ratio of Different Flow Parameter
Across an Expansion Wave**

Surface 3			
Case 1			
Station (in % of Length)	$\frac{h_j}{h_i} \equiv \frac{\rho_j}{\rho_i}$	$\frac{p_j}{p_i}$ (Eqn. 2.5.1)	Pressure Coefficient (Eqn. 2.5.7)
0	0.950	0.931	0.269
7.5	0.816	0.752	0.189
15.1	0.681	0.584	0.113
22.6	0.547	0.430	0.044
30.2	0.547	0.430	0.044
37.7	0.521	0.410	0.031
45.3	0.521	0.410	0.031
52.8	0.494	0.372	0.019
60.4	0.467	0.344	0.006
67.9	0.453	0.330	-0.0006
75.5	0.453	0.330	-0.0006
83.0	0.414	0.291	-0.018
90.6	0.414	0.291	-0.018
98.1	0.440	0.317	-0.007
	$\bar{x} = 0.544$	0.426	0.043
	0.685	0.589	0.116
	0.401	0.278	-0.024
			$Cp_{theor} = -0.0022$

**Table 5.8 Experimental Values of the Ratio of Different Flow Parameters
Across a Expansion Wave**

Surface 5
Case 1

Station (in % of Length)	$\frac{h_j}{h_i} \equiv \frac{\rho_j}{\rho_i}$	$\frac{p_j}{p_i}$ (Eqn. 2.5.1)	Pressure Coefficient (Eqn. 2.5.7)
0	0.973	0.963	0.155
11.3	0.884	0.841	0.117
22.5	0.784	0.711	0.076
33.8	0.724	0.637	0.052
45.1	0.644	0.540	0.022
56.3	0.644	0.540	0.022
67.6	0.604	0.494	0.007
78.9	0.624	0.517	0.014
90.1	0.624	0.517	0.014
	$\bar{x} = 0.707$	0.616	0.046
	0.826	0.765	0.093
	0.588	0.475	0.0014
			$Cp_{theo} = -0.0027$

**Table 5.9 Experimental Values of the Ratio of Different Flow Parameters
Across a Expansion Wave**

Surface 3			
Case 2			
Station (in % of Length)	$\frac{h_j}{h_i} \equiv \frac{\rho_j}{\rho_i}$	$\frac{p_j}{p_i}$ (Eqn. 2.5.1)	Pressure Coefficient (Eqn. 2.5.7)
0	0.939	0.915	0.299
7.5	0.738	0.710	0.210
15.1	0.654	0.552	0.141
22.6	0.551	0.435	0.089
30.2	0.512	0.392	0.071
37.7	0.512	0.392	0.071
45.3	0.500	0.379	0.065
52.8	0.500	0.379	0.065
60.4	0.461	0.338	0.047
67.9	0.449	0.326	0.042
75.5	0.422	0.299	0.030
83.0	0.410	0.287	0.025
90.6	0.397	0.274	0.019
98.1	0.371	0.249	0.008
	$\bar{x} = 0.526$	0.407	0.077
	0.669	0.570	0.148
	0.382	0.260	0.013
			$C_{p_{THEO}} = -0.001$

**Table 5.10 Experimental Values of the Ratio of Different Flow Parameters
Across a Expansion Wave**

Surface 5
Case 2

Station (in % of Length)	$\frac{h_j}{h_i} \equiv \frac{\rho_j}{\rho_i}$	$\frac{p_j}{p_i}$ (Eqn. 2.5.1)	Pressure Coefficient (Eqn. 2.5.7)
0	1.040	1.057	0.141
11.3	0.870	0.822	0.087
22.5	0.756	0.676	0.054
33.8	0.662	0.561	0.028
45.1	0.624	0.517	0.018
56.3	0.624	0.517	0.018
67.8	0.586	0.474	0.008
78.9	0.568	0.453	0.003
90.1	0.586	0.474	0.008
	$\bar{x} = 0.689$	0.594	0.035
	0.826	0.765	0.075
	0.553	0.436	-0.0007
			$Cp_{THEO} = +0.001$

**Table 5.11 Experimental Values of the Ratio of Different Flow Parameters
Across a "Compression Shock Wave"
(Hydraulic Jump)**

Surface 2
Position 1 - Static Conditions

Station (in % of Length)	$\frac{h_j}{h_i} \equiv \frac{\rho_j}{\rho_i}$	$\frac{p_j}{p_i}$ (Eqn. 2.5.1)	Pressure Coefficient (Eqn. 2.5.7)
0	1.293	1.435	0.0657
9.1	1.36	1.543	0.0807
18.2	1.454	1.698	0.104
27.3	1.535	1.839	0.125
36.4	1.548	1.862	0.128
45.5	1.588	1.933	0.139
54.5	1.575	1.91	0.135
63.6	1.495	1.77	0.114
72.7	1.495	1.77	0.114
81.8	1.43	1.658	0.0978
90.0	1.389	1.591	0.0879
100.0	1.336	1.504	0.0749
\bar{x}	1.458	1.706	0.105
$\bar{x} + \sigma$	1.365	1.551	0.082
$\bar{x} - \sigma$	1.552	1.869	0.129

**Table 5.12 Experimental Values of the Ratio of Different Flow Parameters
Across a "Compression Shock Wave"
(Hydraulic Jump)**

Surface 2 Position 1 - Velocity 1
--

Station (in % of Length)	$\frac{h_j}{h_i} \equiv \frac{\rho_j}{\rho_i}$	$\frac{p_j}{p_i}$ (Eqn. 2.5.1)	Pressure Coefficient (Eqn. 2.5.7)
0	1.264	1.39	0.058
9.1	1.494	1.767	0.114
18.2	1.652	2.05	0.156
27.3	1.739	2.213	0.18
36.4	1.825	2.383	0.206
45.5	1.825	2.383	0.206
54.5	1.898	2.532	0.228
63.6	1.854	2.442	0.214
72.7	1.726	2.189	0.177
81.8	1.739	2.215	0.181
90.0	1.711	2.16	0.172
100.0	1.596	1.947	0.141
\bar{x}	1.694	2.217	0.168
$\bar{x} + \sigma$	1.525	1.821	0.122
$\bar{x} - \sigma$	1.863	2.459	0.217

Table 5.13 Experimental Values of the Ration of Different Flow Parameters

Across a "Compression Shock Wave"

(Hydraulic Jump)

Surface 2
Position 1 - Velocity 2

Station (in % of Length)	$\frac{h_j}{h_i} \equiv \frac{\rho_j}{\rho_i}$	$\frac{p_j}{p_i}$ (Eqn. 2.5.1)	Pressure Coefficient (Eqn. 2.5.7)
0	1.243	1.358	0.0532
9.1	1.476	1.737	0.11
18.2	1.637	2.022	0.152
27.3	1.812	2.356	0.202
36.4	1.827	2.386	0.206
45.5	1.841	2.415	0.210
54.5	1.841	2.416	0.211
63.6	1.783	2.3	0.193
72.7	1.739	2.215	0.181
81.8	1.623	1.997	0.148
90.0	1.565	1.892	0.133
100.0	1.449	1.69	0.103
\bar{x}	1.653	2.051	0.156
$\bar{x} + \sigma$	1.470	1.726	0.108
$\bar{x} - \sigma$	1.449	2.405	0.209

**Table 5.14 Experimental Values of the Ratio of Different Flow Parameters
Across a "Compression Shock Wave"
(Hydraulic Jump)**

Surface 4			
Position 1 - Static Conditions			
Station (in % of Length)	$\frac{h_j}{h_i} \equiv \frac{\rho_j}{\rho_i}$	$\frac{p_j}{p_i}$ (Eqn. 2.5.1)	Pressure Coefficient (Eqn. 2.5.7)
0	1.591	1.938	0.139
11.8	1.848	2.431	0.213
23.5	2.133	3.05	0.305
35.3	2.352	3.594	0.386
47.1	2.468	3.909	0.432
58.8	2.52	4.058	0.455
70.6	2.545	4.131	0.465
82.4	2.481	3.947	0.438
94.1	2.313	3.494	0.371
\bar{x}	2.25	3.334	0.347
$\bar{x} + \sigma$	1.937	2.614	0.240
$\bar{x} - \sigma$	2.564	4.186	0.474

**Table 5.15 Experimental Values of the Ratio of Different Flow Parameters
Across a "Compression Shock Wave"
(Hydraulic Jump)**

Surface 4
Position 1 - Velocity 1

Station (in % of Length)	$\frac{h_j}{h_i} \equiv \frac{\rho_j}{\rho_i}$	$\frac{p_j}{p_i}$ (Eqn. 2.5.1)	Pressure Coefficient (Eqn. 2.5.7)
0	0.914	0.882	0.0176
11.8	0.98	0.973	-0.00409
23.5	1.139	1.2	0.0298
35.3	1.283	1.42	0.0625
47.1	1.455	1.7	0.104
58.8	1.547	1.86	0.128
70.6	1.481	1.745	0.111
82.4	1.416	1.635	0.0944
94.1	1.271	1.402	0.0597
\bar{x}	1.276	1.409	0.061
$\bar{x} + \sigma$	1.064	1.090	0.013
$\bar{x} - \sigma$	1.488	1.758	0.113

**Table 5.16 Experimental Values of the Ratio of Different Flow Parameters
Across a "Compression Shock Wave"
(Hydraulic Jump)**

Surface 4
Position 1 - Velocity 2

Station (in % of Length)	$\frac{h_j}{h_i} \equiv \frac{\rho_j}{\rho_i}$	$\frac{p_j}{p_i}$ (Eqn. 2.5.1)	Pressure Coefficient (Eqn. 2.5.7)
0	1.113	1.163	0.0242
11.8	1.192	1.279	0.0415
23.5	1.373	1.565	0.0839
35.3	1.504	1.784	0.117
47.1	1.517	1.808	0.12
58.8	1.452	1.696	0.104
70.6	1.349	1.525	0.078
82.4	1.272	1.402	0.0598
94.1	1.168	1.244	0.0362
\bar{x}	1.326	1.489	0.0727
$\bar{x} + \sigma$	1.186	1.271	0.040
$\bar{x} - \sigma$	1.467	1.721	0.107

**Table 5.17 Experimental Values of the Ratio of Different Flow Parameters
Across a "Compression Shock Wave"
(Hydraulic Jump)**

Surface 2
Position 2 - Static Conditions

Station (in % of Length)	$\frac{h_j}{h_i} \equiv \frac{\rho_j}{\rho_i}$	$\frac{p_j}{p_i}$ (Eqn. 2.5.1)	Pressure Coefficient (Eqn. 2.5.7)
0	1.702	2.144	0.17
9.1	2.068	2.901	0.283
18.2	2.335	3.551	0.379
27.3	2.53	4.087	0.459
36.4	2.651	4.45	0.513
45.5	2.676	4.529	0.525
54.5	2.603	4.303	0.491
63.6	2.578	4.227	0.48
72.7	2.554	4.157	0.469
81.8	2.53	4.087	0.459
90.0	2.457	3.88	0.428
100.0	2.335	3.551	0.379
\bar{x}	2.418	3.771	0.412
$\bar{x} + \sigma$	2.148	3.086	0.31
$\bar{x} - \sigma$	2.688	4.569	0.531

**Table 5.18 Experimental Values of the Ratio of Different Flow Parameters
Across a "Compression Shock Wave"
(Hydraulic Jump)**

Surface 2
Position 2 - Velocity 1

Station (in % of Length)	$\frac{h_j}{h_i} \equiv \frac{\rho_j}{\rho_i}$	$\frac{p_j}{p_i}$ (Eqn. 2.5.1)	Pressure Coefficient (Eqn. 2.5.7)
0	1.607	1.967	0.144
9.1	2.2	3.21	0.328
18.2	2.56	4.174	0.472
27.3	2.713	4.648	0.542
36.4	2.817	4.997	0.594
45.5	2.869	5.178	0.621
54.5	2.92	5.365	0.649
63.6	2.945	5.458	0.663
72.7	2.895	5.273	0.635
81.8	2.869	5.178	0.621
90.0	2.792	4.911	0.581
100.0	2.638	4.41	0.507
\bar{x}	2.652	4.453	0.513
$\bar{x} + \sigma$	2.279	3.406	0.358
$\bar{x} - \sigma$	3.025	5.763	0.708

**Table 5.19 Experimental Values of the Ratio of Different Flow Parameters
Across a "Compression Shock Wave"
(Hydraulic Jump)**

Surface 2
Position 2 - Velocity 2

Station (in % of Length)	$\frac{h_j}{h_i} \equiv \frac{\rho_j}{\rho_i}$	$\frac{p_j}{p_i}$ (Eqn. 2.5.1)	Pressure Coefficient (Eqn. 2.5.7)
0	1.827	2.388	0.206
9.1	2.409	3.747	0.408
18.2	2.636	4.404	0.506
27.3	2.914	5.341	0.645
36.4	3.016	5.729	0.703
45.5	2.965	5.532	0.674
54.5	2.965	5.532	0.674
63.6	2.94	5.438	0.66
72.7	2.914	5.341	0.645
81.8	2.889	5.25	0.632
90.0	2.712	4.645	0.542
100.0	2.611	4.328	0.495
\bar{x}	2.733	4.713	0.552
$\bar{x} + \sigma$	2.408	3.744	0.408
$\bar{x} - \sigma$	3.058	5.897	0.728

**Table 5.20 Experimental Values of the Ratio of Different Flow Parameters
Across a "Compression Shock Wave"
(Hydraulic Jump)**

Surface 4
Position 2 - Static Conditions

Station (in % of Length)	$\frac{h_j}{h_i} \equiv \frac{\rho_j}{\rho_i}$	$\frac{p_j}{p_i}$ (Eqn. 2.5.1)	Pressure Coefficient (Eqn. 2.5.7)
0	1.574	1.907	0.135
11.8	1.821	2.375	0.204
23.5	1.91	2.558	0.232
35.3	2.002	2.755	0.261
47.1	1.912	2.561	0.232
58.8	1.844	2.422	0.211
70.6	1.89	2.516	0.225
82.4	1.799	2.332	0.198
94.1	1.733	2.203	0.179
\bar{x}	1.831	2.396	0.207
$\bar{x} + \sigma$	1.715	2.167	0.174
$\bar{x} - \sigma$	1.948	2.638	0.243

**Table 5.21 Experimental Values of the Ratio of Different Flow Parameters
Across a "Compression Shock Wave"
(Hydraulic Jump)**

Surface 4
Position 2 - Velocity 1

Station (in % of Length)	$\frac{h_j}{h_i} \equiv \frac{\rho_j}{\rho_i}$	$\frac{p_j}{p_i}$ (Eqn. 2.5.1)	Pressure Coefficient (Eqn. 2.5.7)
0	1.517	1.808	0.12
11.8	1.678	2.098	0.163
23.5	1.725	2.187	0.176
35.3	1.701	2.141	0.17
47.1	1.587	1.931	0.138
58.8	1.587	1.931	0.138
70.6	1.564	1.89	0.132
82.4	1.472	1.729	0.108
94.1	1.472	1.729	0.108
\bar{x}	1.59	1.936	0.139
$\bar{x} + \sigma$	1.5	1.778	0.116
$\bar{x} - \sigma$	1.679	2.1	0.164

**Table 5.22 Experimental Value of the Ratio of Different Flow Parameters
Across a "Compression Shock Wave"
(Hydraulic Jump)**

Surface 4
Position 2 - Velocity 2

Station (in % of Length)	$\frac{h_j}{h_i} \equiv \frac{\rho_j}{\rho_i}$	$\frac{p_j}{p_i}$ (Eqn. 2.5.1)	Pressure Coefficient (Eqn. 2.5.7)
0	1.508	1.792	0.118
11.8	1.671	2.084	0.161
23.5	1.786	2.306	0.194
35.3	1.797	2.308	0.194
47.1	1.648	2.043	0.155
58.8	1.556	1.876	0.13
70.6	1.556	1.876	0.13
82.4	1.556	1.876	0.13
94.1	1.511	1.797	0.118
\bar{x}	1.62	1.991	0.147
$\bar{x} + \sigma$	1.517	1.808	0.12
$\bar{x} - \sigma$	1.722	2.182	0.176

APPENDIX C

This appendix presents the details of the procedures and measurements carried out during the calibration of the hydraulic simulator.

The topics considered in this appendix are:

1. Determination of the water depth as a function of head height.
2. Calculation of velocity using Pitot tubes.
3. Calculation of velocity using High Speed Camera.
4. Determination of angles of table for uniform flow.

1. Determination of water depth as a function of head height

The depth of the water on the surface of the table was determined using a micrometric depth probe.

The readings were obtained directly from a digital display, and the procedure to set up the measuring probe was the following:

Before the simulator was turned on, the probe was lowered until its tip touched the surface of the glass. At this position, the reading was set to zero; and then the tip was lifted. At this point, it was ready to be used.

Several measurements were made at different longitudinal stations, exercising care to avoid hysteresis in the measuring probe. This was done by discarding measurements when the micrometer of the probe had to be reversed in direction during the determination of the water depth. The measurements for water depth are shown in Tables 1.B and 2.B.

Table 1.B

Measurements of Water Depth vs Head Height

Station: .1m Downstream from Nozzle

Head Height (mm)	Water Depth (mm)	Best Estimate of σ
20	7.713	0.0227
40	7.445	0.0340
50	7.425	0.0144
60	7.387	0.0170
80	7.281	0.0125

Table 2.B

Measurements of Water Depth vs Head Height

Station: .25 m Downstream from the Nozzle

Head Height (mm)	Water Depth (mm)	Best Estimate of σ
20	7.687	0.124
30	7.535	0.049
40	7.487	0.042
60	7.360	0.040
80	7.258	0.073
100	7.163	0.032

2. Calculation of velocity using Pitot tubes

For the calculation of velocity with a Pitot tube, the energy equation for incompressible flow, better known as Bernoulli's equation, can be used:

$$V = \sqrt{2g \left(\frac{p_s}{\gamma} - \frac{p_o}{\gamma} \right)}$$

where V = velocity of the flow

g = gravity constant

γ = specific weight of water

p_o = static pressure

p_s = stagnation pressure

Once the differential pressure is known, the velocity can be easily obtained.

In order to get this differential, it is necessary to measure the difference in height of the column of water inside the tube when the fluid is flowing and when it is at rest.

At this point, another problem had to be addressed, namely, that of capillarity. The reduced depth of the water dictated the use of small diameter tubes (1 mm). Since the capillarity effects only become negligible for diameters larger than 12 mm [Ref. 5], the capillary rise had to be taken into account.

The capillary rise, h , can be calculated using the following equation in conjunction with Figure 1.B.

$$h = \frac{2\sigma \sin \theta}{\gamma r}$$

where σ = surface tension (units of force per unit length)

θ = wetting angle (generally assumed to be 90°)

γ = specific weight of liquid

r = radius of tube

It is important to point out that since any impurity may alter the capillary rise considerably; the tubes were carefully cleaned before being used. In spite of this, it was not possible to consistently get good agreement between the theoretical and experimental values of capillary rise.

The values of calculated velocities using this method are shown in Table 3.B.

Table 3.B
Velocity calculations using Pitot tube of 1mm diameter

Head Height (mm)	Velocity (m/s)
20	0.406
40	0.751
60	0.982
80	1.162
100	1.321
120	1.458

Due to the difficulty in obtaining a better agreement between theoretical and experimental values of capillary rise, this method was considered unreliable; and, therefore, an alternate method was utilized.

3. Determination of velocity using High Speed Camera

The system used for the calculation of the speed of the flow is a Kodak SP 2000 "Motion Analysis System".

This system can record events using a range of 60 to 2000 frames per second provided there is enough light for recording. This last aspect was very important in order to get good images.

Several settings of camera resolution (frames per second) were utilized, but only those corresponding to the values used are included here.

Table 4.B shows the velocities at a station 0.1m downstream from the nozzle, Table 5.B shows the velocities at a station 0.45m for different angles of inclination, and Table 6.B shows the velocity differential between the two points. In each case the uncertainty was calculated using the following expression:

$$w_v = \left[\left(\frac{\partial V}{\partial t} \delta t \right)^2 + \left(\frac{\partial V}{\partial \Delta} \delta \Delta \right)^2 \right]^{\frac{1}{2}}$$

where $\frac{\partial V}{\partial t} = -\frac{\Delta}{t^2}$ and $\frac{\partial V}{\partial \Delta} = \frac{1}{t}$. Also δt was the best estimate for the standard deviation and $\delta \Delta = v \delta t$ the estimated uncertainty in displacement of the float due to error in observation.

The velocity differential for each head height was plotted against angle of inclination, and the data was best fitted to get the intersection of the curve with the abscissa. This intersection gave the angle of zero velocity differential and, therefore, of uniform velocity. The procedure to assign a value of uncertainty is explained in section 4.1.4.3. Each point of zero velocity differential was plotted and best fitted as shown in Fig. 4.4.

The plots for each one of the head heights are shown in Figures B.3 through B.7

Table 4.B
Velocity Using High Speed Camera
Resolution 1,000 frames per second

Head Height (mm)	Δt_{ave} (sec)	σ	Velocity (m/s)
20	0.0454	5.59×10^{-3}	1.101 ± 0.027
40	0.05425	5.00×10^{-3}	0.922 ± 0.028
50	0.060	2.00×10^{-3}	0.833 ± 0.0285
60	0.06875	1.50×10^{-3}	0.727 ± 0.0115
80	0.1208	5.48×10^{-4}	0.414 ± 0.0190

Table 5.B
Velocity Versus Angle of Inclination of Table
Resolution 1,000 frames per second

Head Height = 80 mm		
Angle of Inclination θ	Velocity V (m/s)	Uncertainty in Velocity
0	1.202	0.0337
0.5	1.227	0.0450
1.0	1.274	0.0394
1.5	1.305	0.0365
2.0	1.351	0.0330

Head Height = 60 mm		
Angle of Inclination θ	Velocity V (m/s)	Uncertainty in Velocity
0	1.005	0.0226
0.5	1.031	0.0238
1.0	1.071	0.0265
1.5	1.103	0.0281
2.0	1.136	0.0516

Head Height = 50 mm		
Angle of Inclination θ	Velocity V (m/s)	Uncertainty in Velocity
0	0.885	0.0181
0.5	0.932	0.0200
1.0	0.971	0.0218
1.5	1.000	0.0258
2.0	1.042	0.0217

Head Height = 40 mm		
Angle of Inclination θ	Velocity V (m/s)	Uncertainty in Velocity
0	0.775	0.0139
0.5	0.856	0.0167
1.0	0.909	0.0165
1.5	0.943	0.0178
2.0	0.990	0.0226

Head Height = 20 mm		
Angle of Inclination θ	Velocity V (m/s)	Uncertainty in Velocity
0	0.488	0.0055
0.5	0.600	0.0080
1.0	0.671	0.0104
1.5	0.746	0.0157
2.0	0.797	0.0252

Table 6.B
Velocity Differential

Head Height = 80 mm		
Angle of Inclination θ	Velocity Variation (m/s) $V_{.45m} - V_{.10m}$	Uncertainty in Velocity
0	0.101	± 0.0337
0.5	0.126	± 0.0450
1.0	0.173	± 0.0394
1.5	0.204	± 0.0365
2.0	0.250	± 0.0330

Head Height = 60 mm		
Angle of Inclination θ	Velocity Variation (m/s) $V_{.45m} - V_{.10m}$	Uncertainty in Velocity
0	0.078	± 0.0266
0.5	0.109	± 0.0238
1.0	0.149	± 0.265
1.5	0.182	± 0.0281
2.0	0.214	± 0.0516

Head Height = 50 mm		
Angle of Inclination θ	Velocity Variation (m/s) $V_{.45m} - V_{.10m}$	Uncertainty in Velocity
0	0.052	± 0.0181
0.5	0.099	± 0.020
1.0	0.138	± 0.0218
1.5	0.167	± 0.0258
2.0	0.209	± 0.0217

Head Height = 40 mm		
Angle of Inclination θ	Velocity Variation (m/s) $V_{.45m} - V_{.10m}$	Uncertainty in Velocity
0	0.048	± 0.0139
0.5	0.129	± 0.0167
1.0	0.182	± 0.0165
1.5	0.216	± 0.0178
2.0	0.263	± 0.0226

Head Height = 20 mm		
Angle of Inclination θ	Velocity Variation (m/s) $V_{.45m} - V_{.10m}$	Uncertainty in Velocity
0	0.074	± 0.0055
0.5	0.165	± 0.0080
1.0	0.257	± 0.0104
1.5	0.332	± 0.0157
2.0	0.383	± 0.0252

REPORT DOCUMENTATION PAGE			Form Approved OMB No 0704-0188	
<small>1. This report is the property of the U.S. Government. It is loaned to your agency for your use only. It and its contents are not to be distributed outside your agency. Send comments regarding this report's burden estimate or any other aspect of this report, including suggestions for reducing the burden, to Washington Headquarters Services, Directorate for Information Operations and Reports, 1215 Jefferson Davis Highway, Suite 1204, Arlington, VA 22202-4302, and the Office of Management and Budget, Paperwork Reduction Project (0704-0188), Washington, DC 20503.</small>				
1. AGENCY USE ONLY (Leave blank)		2. REPORT DATE 6 June 1994	3. REPORT TYPE AND DATES COVERED Final	
4. TITLE AND SUBTITLE Calibration and Initial Testing of a New Hydraulic Simulator			5. FUNDING NUMBERS	
6. AUTHOR(S) Cristian A. Puebla, B.S.				
7. PERFORMING ORGANIZATION NAME(S) AND ADDRESS(ES) AFIT/ENY Wright-Patterson AFB OH 45431			8. PERFORMING ORGANIZATION REPORT NUMBER AFIT/GA/ENY/94J-1	
9. SPONSORING/MONITORING AGENCY NAME(S) AND ADDRESS(ES) Flight Dynamics Directorate WL/FIVRA Wright-Patterson AFB OH 45431			10. SPONSORING/MONITORING AGENCY REPORT NUMBER	
11. SUPPLEMENTARY NOTES				
12a. DISTRIBUTION AVAILABILITY STATEMENT Approved for public release; distribution unlimited			12b. DISTRIBUTION CODE	
13. ABSTRACT (Maximum 200 words) <p>In the present research, the flow field associated with the ejection of a crew capsule from the fuselage of a high speed generic aircraft was experimentally investigated by means of the modified gas hydraulic analogy. For this, an existing hydraulic simulator was calibrated and modified to adapt it to the needs of the experiment. The analogy was evaluated for a five-sided capsule alone, and good quantitative agreement with the 2-D shock-expansion theory was obtained. It was found that the size of the model played a key role in the determination of good quantitative data. The analysis of the capsule interacting with a fuselage was made considering it at fixed vertical positions from the fuselage and moving with respect to the fuselage at different constant speeds. A clear difference in water depth ratio distribution on the surfaces of the capsule was found between the static and dynamic conditions and also differences occurred for the various velocities of separation. The agreement between theory and experiment was fair. It was concluded that larger models are needed to get good quantitative agreement between theory and experiment and that any separation study should be made applying a dynamical model.</p>				
14. SUBJECT TERMS Gas Hydraulic Analogy, Hydraulic Simulator, Modified Analogy, Aerodynamic Coefficients, Froude Number, Mach Number, Capsule - Fuselage Interaction, Hydraulic Jump, 2-D Shock-Expansion Theory			15. NUMBER OF PAGES 140	
			16. PRICE CODE	
17. SECURITY CLASSIFICATION OF REPORT UNCLASSIFIED	18. SECURITY CLASSIFICATION OF THIS PAGE UNCLASSIFIED	19. SECURITY CLASSIFICATION OF ABSTRACT UNCLASSIFIED	20. LIMITATION OF ABSTRACT UL	